B-Tagging Calibration at the ATLAS Experiment

Dissertation

**zur Erlangung des akademischen Grades
eines Doktors der Naturwissenschaften
(Dr. rer. nat.)
der Fakultät Physik
der Technischen Universität Dortmund**

vorgelegt von

Dipl.-Phys. Florian Hirsch

Lehrstuhl für Experimentelle Physik IV
Fakultät Physik
Technische Universität Dortmund

Juni 2011

Gutachter: Prof. Dr. C. Gößling
               Prof. Dr. Dr. Wolfgang Rhode

Disputation: 15.07.2011

Contents

1 Introduction

This Ph.D. thesis describes a measurement of the b-tagging efficiency for selected b-tagging algorithms at the ATLAS experiment. Apart from this main focus the influence of b-tagging on a measurement of the top-quark cross-section is discussed. In addition some measurements of characteristics of the sensors of the ATLAS Pixel Detector are shown.

The LHC delivers proton-proton collisions at 7 TeV center-of-mass energy since 2010 with steadily increasing instantaneous luminosity. These collisions are being recorded with the ATLAS Detector which is a state-of-the-art 4π multi-purpose particle detector. The collected data is used on the one hand for commissioning of the detector and of the different physics objects that are needed to link detector signals to predictions from simulations based on inputs from particle physics theory. On the other hand measurements of parameters like cross-sections of known processes are conducted for the first time at this center-of-mass energy. Those measurements help the commissioning of the detector as well since performance measurements and physics measurements are closely intertwined. In addition they provide useful input to theoretical physics since they can be directly compared to predictions assuming the standard model of particle physics or assuming extensions of this model. Especially measurements on heavy objects like the top-quark provide a window to new physics. No discovery was claimed by the ATLAS Detector so far which is not surprising since the total integrated luminosity in 2010 was 45 pb^{-1} and has just reached 1 fb^{-1} at this point in 2011, but it was already possible to set limits on models like quark-contact interactions which would allude to a substructure of quarks or to set limits on super-symmetric extensions on the standard model.

Chap. 2 gives a brief overview of the standard model which is the basic theory of particle physics and uses it to motivate the construction of particle colliders and particle detectors. Chap. 3 then describes the ATLAS Detector and its different subsystems. For the Pixel Detector some qualification measurements for the sensor are presented in Chap. 4. Chap. 5 introduces the concept of b-tagging and the main classes of b-tagging algorithms are presented with a focus on the SV0 tagger and the JetProb tagger which are the two taggers currently calibrated and used in physics analyses. Chap. 6 shows the application of the p_T^{rel} method to measure the b-tagging efficiency in detail. It also shows results of the first measurements of the top-quark pair-production cross-section at 7 TeV center-of-mass energy and focuses on the role b-tagging algorithms play in these measurements.

2 Particle Physics

The theory of particle physics aims to give a description of the fundamental building blocks that form all things that exist and of their interactions. The theory in its current form is called the standard model of particle physics [1]. It postulates the existence of quarks and leptons as fundamental particles. This means that every observed object is comprised of these particles but the particles themselves do not have a substructure. It also postulates the existence of three fundamental interactions, the strong force, the weak force and the electromagnetic force. The weak force and the electromagnetic force are unified in the electroweak theory. The fourth known force of nature, the gravitational force, is not part of the standard model. Furthermore the existence of the Higgs boson is postulated. At this point every particle predicted by the standard model except for the Higgs boson has been observed and experimental data is consistent with standard model predictions to a high degree, therefore this theory is relevant and future more general theories will likely contain the standard model as a special case.

The theory itself is not developed in this chapter, instead a brief summary of important predictions of this theory are given to set the stage for physics with the ATLAS experiment. Of the many different motivations for this experiment the potential for the discovery of the Higgs boson is developed. b-quark and top-quark physics are covered in some detail since they are important for this work and a brief summary of electroweak decays is given for that purpose. In addition the concept of a particle jet is introduced.

2.1 Particle accelerators and the LHC

Tab. 2.1 contains a list of the particles postulated by the standard model. There is an antiparticle for each quark and lepton but it is not important for this work to distinguish particles from antiparticles. If necessary the antiparticle is marked with an over-bar. The dynamics of these particles are described by a U(1) x SU(2) x SU(3) gauge group theory. It describes the interaction of quantum fields that represent the particles like the scattering of two electrons by exchange of a photon. It also states that particles can be annihilated and created during those exchange processes, for example muons can weakly decay to electrons and neutrinos.

It should be noted that of the particles in Tab. 2.1 only the u quark, the d quark and the electron comprise stable matter. All other particles are unstable and decay to those lighter particles. As a consequence, in order to check the predictions of the standard model, the heavier particles have to be created since they cannot be found localized in nature in reasonable quantities. This is typically done with particle accelerators that accelerate electrons or protons to high energies and lead them to a point where they are collided with a target or with another accelerated particle beam in opposite direction. Fig. 2.1 shows a calculation that predicts the cross-sections for the production of different types of particles in proton-proton collisions for different center-of-mass energies of those collisions. The cross-section σ of a

Quark	Mass [MeV]	Lepton	Mass [MeV]	Boson	Mass [MeV]
Up (u)	$2.49^{+0.81}_{-0.79}$	Electron (e)	0.511	Photon (γ)	0
Down (d)	$5.05^{+0.75}_{-0.95}$	Muon (μ)	105.7	W	$(80.339 \pm 0.023) \cdot 10^3$
Charm (c)	$1.27^{+0.07}_{-0.09} \cdot 10^3$	Tau (τ)	1776.82 ± 0.16	Z	$(91.1876 \pm 0.0021) \cdot 10^3$
Strange (s)	101^{+29}_{-21}	ν_e	$< 2 \cdot 10^{-3}$	Higgs (H)	?
Top (t)	$(172 \pm 1.6) \cdot 10^3$	ν_μ	< 0.19		
Bottom (b)	$4.19^{+0.18}_{-0.06} \cdot 10^3$	ν_τ	< 18.2		

Table 2.1: Summary of the standard model particles. Masses are taken from [2]. No errors on the electron and on the muon are quoted since the measurements are highly precise and a higher accuracy than the quoted one is not needed. (u,d), (c,s) and (t,b) form the three quark families.

production process is defined by

$$R = \sigma \cdot L$$

where R is the observed production rate and L is the number of delivered interactions per area and time from the accelerator assuming that all production events are observed.

It is evident that a high creation rate for particles with higher masses can be achieved by increasing the collision energy to increase the cross-section and by increasing the luminosity. Therefore particle accelerators are classified by the center-of-mass energy and the luminosity they deliver. The LHC is a proton-proton circular collider [4]. A circular collider accelerates particles with electrical fields and bends them into a circular path with magnets. Two particle beams are accelerated in opposing directions in this way and are collided at specific points to create the heavy particles. The LHC has a circumference of 27 km and is situated at CERN near Geneva. It currently delivers collisions with center-of-mass energies of 7 TeV and has done so through March-November 2010 with a peak luminosity of $2.1 \cdot 10^{32}$ cm^{-2} s $^{-1}$ [5] measured at the ATLAS experiment. It has been estimated that the LHC will produce enough Higgs bosons to discover the Higgs boson if its mass is in the region from 120 GeV to 500 GeV with the ATLAS detector when 10 fb^{-1} of data are collected [6]. This integrated luminosity will be collected through the next years. The mass range is interesting since the Higgs mass has been constrained by standard model calculations including parameters like the W boson mass and the top-quark mass as shown in Fig. 2.2.

2.2 Particle Detectors and ATLAS

In addition to creating particles of interest it is also necessary to build devices that can be used to identify and study them. These devices are called particle detectors and they are built close to the collision point of the colliders. The main goals to achieve when setting up the discovery of the Higgs boson is enabling the detector to identify Higgs boson decays and to discriminate the process under study against background from other processes since other processes occur at a much higher rate as can be seen in Fig. 2.1. The requirements are similar for other physics goals of the ATLAS experiment like the search for supersymmetry or generally the search for heavy particles.

The Higgs boson is predicted to decay on a timescale of $\sim 10^{-23}$ s [8] (assuming a
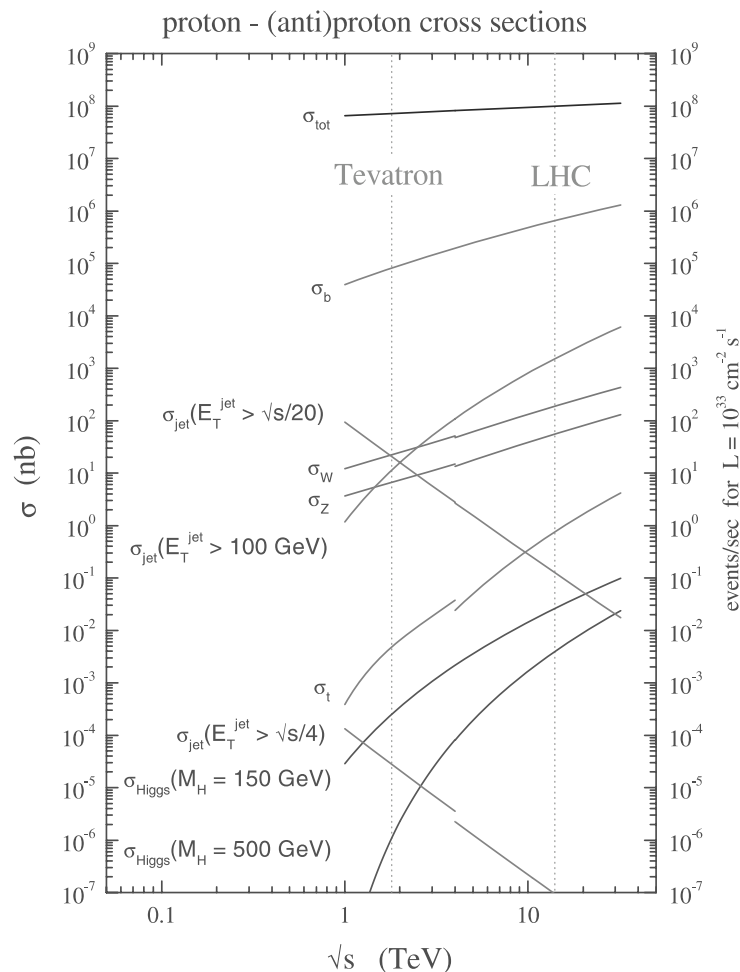
Figure 2.1: Cross-sections for selected production processes production at different center-of-mass energies. Two different assumptions for the Higgs mass are shown. The LHC is marked down at 14 TeV but it is currently operating at 7 TeV. [3]

light Higgs of mass < 140 GeV, the lifetime is shorter if the boson has a higher mass) so a direct measurement of the particle is impossible since it will not have traveled any measurable distance from the interaction point before it decays. It has to be identified using its longer lived decay products which necessitates the design of the detector to permit particle identification and measurements of particle characteristics like their trajectories, momenta and energies. This has to be done hermetically so particles cannot escape from the interaction point undetected, especially since neutrinos cannot be directly detected and have to be reconstructed by means of missing energy in the event. The ATLAS detector is a device that is built with these design goals and it is explained in detail in Chap. 3.

2.3 Jets

Some common decay products from heavy particles that exist long enough to reach the particle detector are leptons like electrons and muons or light hadrons which
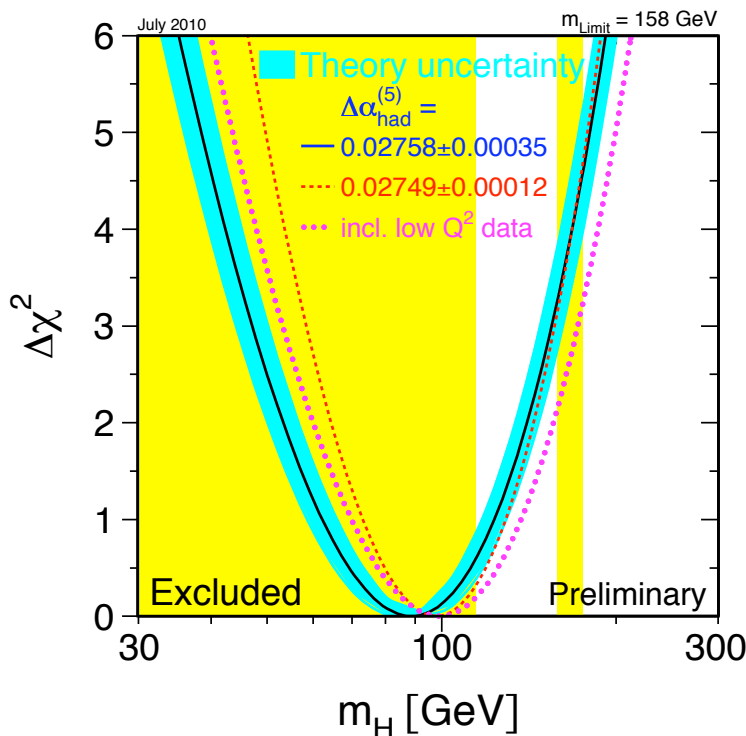
Figure 2.2: Higgs mass from electroweak fits. $\Delta\chi^2$ indicates the goodness of fit, the minimum value is preferred. The different curves are obtained by taking the input parameters from different measurements but all of them show that a low Higgs mass near the exclusion limit is preferred. The vertical bands show the 95% CL exclusion limits on m_H from the direct searches at LEP-II (up to 114 GeV) and the Tevatron (158 GeV to 175 GeV) [7].

are systems of quarks and gluons. Electrons and muons are direct decay products and are measured with the calorimetry and dedicated muon systems. The hadrons are created from quarks or gluons with varying multiplicities and kinematics so a concept is needed to give a representations of those particle showers.

Jets are objects defined to represent final states of quarks and gluons created during the proton-proton collisions that are stable in the sense that they do not decay before reaching the detector material (so particles created in the primary interaction as well as particles from subsequent decays of heavier particles). The quarks and gluons do not reach the detector material unchanged but they radiate additional gluons and fragment into hadrons which is dictated by quantum chromodynamics. One consequence of the theory is that observable states are colorless and of integer charge which the quarks and gluons are not. Jet algorithms cluster the shower of colorless particles that is created during the initial particles flight to the detector in simulations while at the same time being able to cluster detector signals like signals from calorimeters that stem from these particles to allow comparison of theory and experiment. In some sense the jets are therefore representations of the initial quark but they cannot be identified with them since the representation depends on the algorithm and showering model chosen to do the calculation.

Jet algorithms have to be collinear safe [9]. That means that if a quark with momen-

tum p_1 splits into two particles with lower momentum (p_{1a}, p_{1b}) during its fragmentation and there is another particle with momentum p_2 in the vicinity, the resulting distribution of jets must not differ from the case where the particle does not split. Some jet algorithms like cone based algorithms suffer from this when $p_1 > p_2 > p_{1a}, p_{1b}$. In addition the algorithms have to be infrared safe. That means that the emission of a soft gluon from a quark must not lead to a change in the jet distribution. This might happen if the jet clustering algorithm finds two close-by jets with high energy in the case where no gluon is emitted but finds only one merged jet in the case where one of the two high momentum quarks emits a soft gluon in-between the two quarks. The jet algorithm used for the measurements in this thesis has both these attributes and is described in Sec. 6.1.3.

2.4 Electroweak decays and the CKM matrix

In the standard model the flavor of a quark is preserved in all interactions except for weak interactions. The calculation of theoretical predictions for cross-sections or decay rates in this realm contains phase-space considerations and a calculation of the process dynamics. The process dynamics are often represented by Feynman diagrams. Feynman diagrams are a pictorial representation that give an intuitive idea of a process while at the same time providing a set of rules to calculate matrix elements which contain the dynamics. The matrix element is a measure of the amplitude of the process, so the higher the matrix element the higher the rate at which a certain process occurs. An example Feynman graph for a weak decay is given in Fig. 2.3.

The electroweak theory allows the change of a quark family by emission of a W boson. The decay rate for c-quarks and b-quarks shows the dependency

$$\Gamma_{ff'} \sim \frac{m_f^5}{m_W^4} |V_{ff'}|^2$$

where m_f is the mass of the decaying quark, m_W is the W-boson mass and $V_{ff'}$ is the CKM matrix element for the quark flavors f and f'. For top-quarks which decay predominantly to b-quarks the dependency is

$$\Gamma_{tb} \sim \frac{m_t^3}{m_W^2} |V_{tb}|^2$$

The CKM matrix is part of this theory and adds to the prescription of calculating matrix elements due to the mixing of quark flavors across families. $V_{ff'}$ is small if the quark flavors are not from the same family as can be seen in Eq. (2.1) where the CKM matrix is given. The CKM matrix elements are known to a higher precision than stated here but only the order of magnitude is important so the numbers are rounded.

$$\begin{pmatrix} |V_{ud}| & |V_{us}| & |V_{ub}| \\ |V_{cd}| & |V_{cs}| & |V_{cb}| \\ |V_{td}| & |V_{ts}| & |V_{tb}| \end{pmatrix} = \begin{pmatrix} 0.974 & 0.225 & 0.003 \\ 0.225 & 0.973 & 0.041 \\ 0.009 & 0.040 & 0.999 \end{pmatrix} \tag{2.1}$$

In the case of a b-quark decay the mass ratio is very low and in addition the CKM matrix element is small which suppresses the decay when compared to the top-quark decay where the mass ratio is large and the CKM matrix element is close to unity. This explains the high lifetime of the b-quark and therefore its tendency to travel measurable distances before decaying which is exploited for b-tagging.

2.5 b-hadrons

Since this work is mainly concerned with the identification of hadrons containing a b-quark some characteristics of b-hadron decays are developed in this section. The identification of b-quarks is interesting since the decay chains of particles that are studied with the ATLAS detector oftentimes contain b-quarks. Fig. 2.3 shows two example Feynman graphs that illustrate the decay of the top quark and of the predicted Higgs boson into a final state that contains b-quarks.
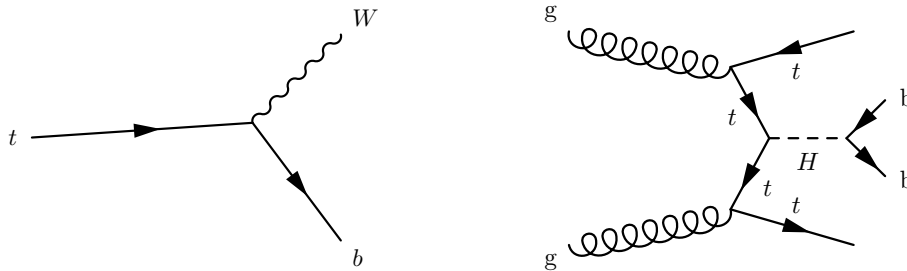
Figure 2.3: Feynman graphs for the weak decay $t \rightarrow Wb$ on the left and for the Higgs production associated with top-quarks with subsequent decay $H \rightarrow bb$ on the right. In both cases b-quarks are an important part of the signature.

The mean lifetime of the produced b-quarks is higher than the hadronization scale which is[1] $\sim 3 \cdot 10^{-24} s$, therefore b-quarks will hadronize and form b-hadrons before decaying. A spectrum of confined states containing two or three quarks[2] is allowed in the standard model and the full spectrum is produced in high energy collisions. Tab. 2.2 shows the fractions of the different hadrons produced in this hadronization. The dominantly produced hadrons are B-mesons. The decay of this meson can be

Hadron	Quark content	Produced fraction [%]
B^+, B^0	$(u\bar{b})$, $(d\bar{b})$	40.2 ± 1.3
B_S^0	$(s\bar{b})$	11.2 ± 1.3
b baryons	various	8.4 ± 2.2

Table 2.2: Fractions of b-hadrons after hadronization. Combined measurements of LEP and Tevatron. The fractions of B_c mesons is measured to be lower than the measurement errors on the other fractions and is therefore omitted. The fraction of produced B^+ is assumed to be the same as the fraction of produced B^0 [10].

described by the decay of the contained b-quark with the additional quark as a spectator and the b-quark will decay predominantly by $b \rightarrow cW$ [11]. A B-meson has a mean lifetime $\tau \sim 1.6$ ps [2] and will therefore travel an average distance $l \sim 5$ mm when produced with a momentum of ~ 50 GeV calculated by

$$l = \gamma v \tau, \ \gamma = \sqrt{1 - \frac{v^2}{c^2}}^{-1} \tag{2.2}$$

This can be exploited by building detectors that can resolve these distances to identify b-hadrons as will be explained in Chap. 5.

---

[1] Assuming $\Lambda = 200$ MeV

[2] A two-quark state is called a meson, a three quark state is called a baryon and both are called hadron.

Furthermore the virtual W-boson that is produced from the *b*-quark decays leptonically by $W \to \mu\nu_\mu$ with a fraction ~10.6%. An example distribution of the muon energy in the *b*-hadron rest-frame can be seen in Fig. 2.4. The spectrum was measured with the DELPHI experiment. Due to the mass of the *b*-hadron the produced muon can have a high momentum relative to the original flight direction of the *b*-hadron which will be exploited in Chap. 6.
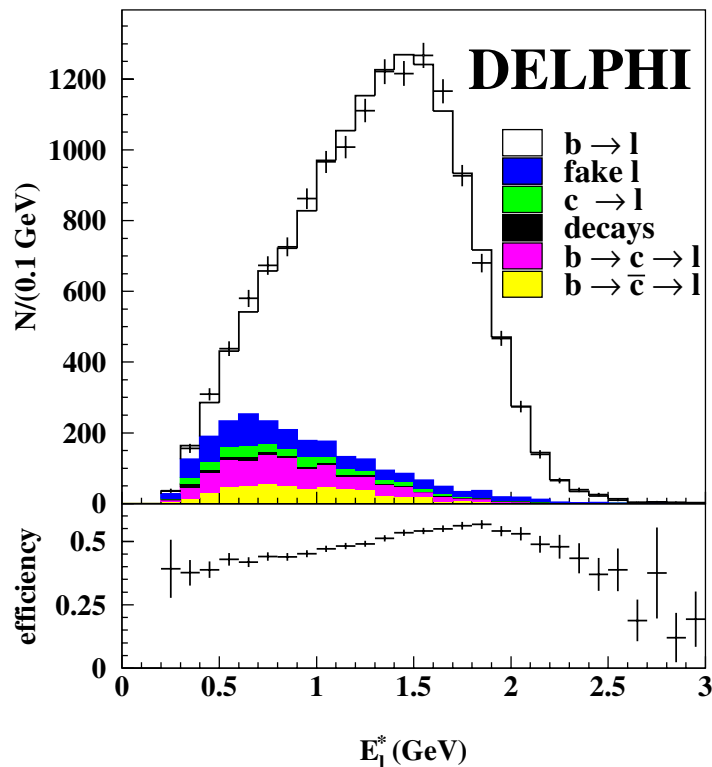

Figure 2.4: Spectrum of the lepton energy in the *b*-hadron rest-frame as measured with the DELPHI experiment [12].

It is also vital to have an understanding of the production of *b*-quarks at the LHC to follow the discussion of the p_T^{rel} method in Chap. 6. *b*-quarks are predominantly produced in pairs of two. The leading order contributions from direct quark production are shown as Feynman graphs in Fig. 2.5. Quarks created in the direct production have momenta in opposite directions in the rest-frame of the colliding incoming particles.

As examples of higher order corrections the contributions from gluon-splitting are shown in Fig. 2.6. Here the b$\bar{\text{b}}$ system is boosted in the direction of the gluon that splits so the opening angle between the two quarks is shallower. This makes it possible for two *b*-quarks to be so close to each other that they are resolved as a single jet by the detector. The ratio of *b*-quarks produced with a shallow opening angle to *b*-quarks produced with a wide opening angle between each other can be as high as 2 [13], so this has to be considered in the systematic uncertainty treatment in Sec. 6.6.

9
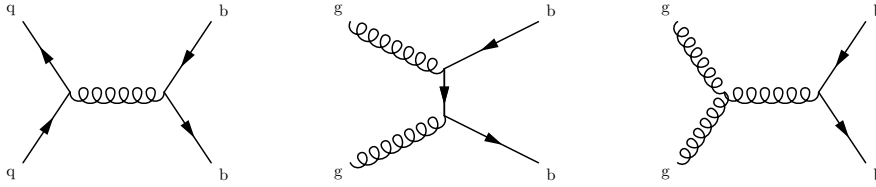
Figure 2.5: Feynman graphs for the direct b$\bar{\text{b}}$ production. q$\bar{\text{q}}$ annihilation on the left and gluon fusion in the middle and on the right.
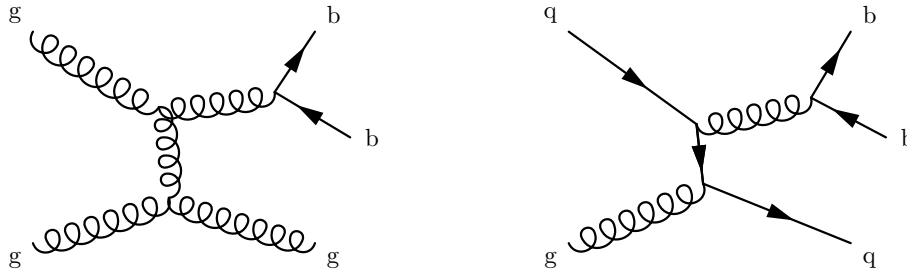
Figure 2.6: Non exhaustive list of Feynman graphs for the b$\bar{\text{b}}$ production by gluon splitting.
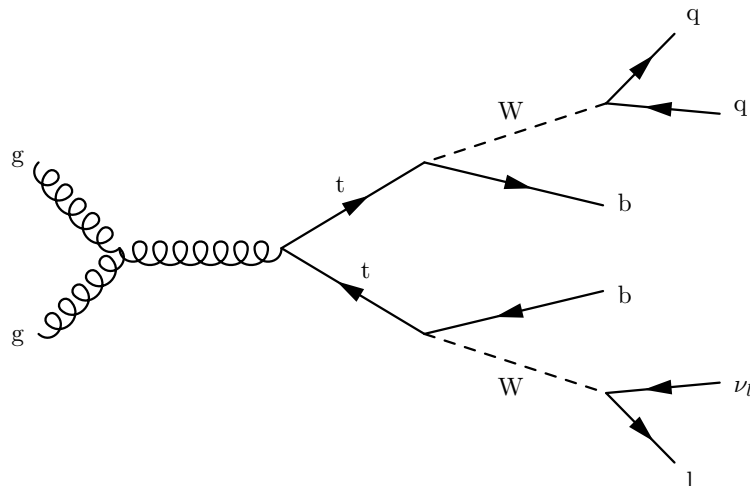
2.6 Top-quarks

In Sec. 6.8 measurements of the top-quark pair-production cross-section are outlined so a brief description of the production and decay of those quarks is given. Top-quarks are predominantly produced in pairs, similar to b-quarks. The decay of a top-quark occurs before hadronization due to its high mass which means that no consideration of the branching ratios to different hadron types is necessary. The predominant decay channel is $t \to Wb$ since the other possible quark flavors (s and d) are heavily suppressed by the CKM matrix.

The possible topologies of the consecutive decays of the W bosons leads to a multitude of signatures. Fig. 2.7 shows the decay $tt \to WWbb \to l\nu_l qqbb$ which is the semileptonic decay channel. q denotes a quark in the final state and l denotes a lepton of arbitrary flavor. The quark flavors can be (u,d) or (c,s). This channel is sometimes called the golden channel since it provides an easy to measure signature in particle detectors which consists of the high energy isolated[3] lepton, the high energy single neutrino that leaves a gap of missing energy in the detector, two b-quarks that can be tagged with the algorithms described in Chap. 5 and two more high energy jets which can be used to discriminate against background in an event selection. At the same time this channel still occurs with a decent rate.

In addition there are the decay channels $tt \to WWbb \to qqqqbb$ which is the full-hadronic channel and $tt \to WWbb \to ll'\nu_l\nu_{l'}bb$ which is the dileptonic decay channel. The quark flavors appear in pairs similar to the semileptonic channel and l and l' denote independent lepton flavors. The Feynman diagrams are similar to the one for the semileptonic decay with different combinations of the W-boson decay branches. The fullhadronic decay occurs with the highest rate and the dileptonic decay occurs

---

[3]Meaning that the lepton is not in the vicinity of a jet. Leptons from b-hadron decays are oftentimes not isolated for example.

Figure 2.7: Production of top-quark pair by gluon fusion and subsequent semileptonic decay chain.

with the lowest rate. The rates of the different decay processes are summarized in Tab. 2.3.

Decay channel	Percentage of total decays
dileptonic	10.5
semileptonic	43.8
semileptonic one lepton	14.6
fullhadronic	45.6

Table 2.3: Fractions of the three different decay channels of the top-quark assuming that all W decay channels have the same probability. Semileptonic one lepton is the amount of semileptonic decays when fixing the lepton flavor [2].

Measurements of top-quark parameters are important for a variety of reasons. The cross-section at 7 TeV has not been measured before and is a prediction of the standard model. A measurement can therefore confirm this prediction or it can show discrepancies which would hint to physics beyond the standard model. Furthermore the production of top-quarks creates high energy jets and leptons. Those are often part of signatures for physics searches so the top-quark events are a background to those searches. A thorough understanding of the background is always necessary for any measurement and the measurement of the cross-section provides an estimate of the magnitude of background to expect for those measurements.

The top-quark mass is also an important parameter since it provides constraints on the Higgs mass as can be seen in Fig. 2.8. Conversely a measurement of both the Higgs boson and the top-quark mass provides constraints on the validity of the standard model prediction.
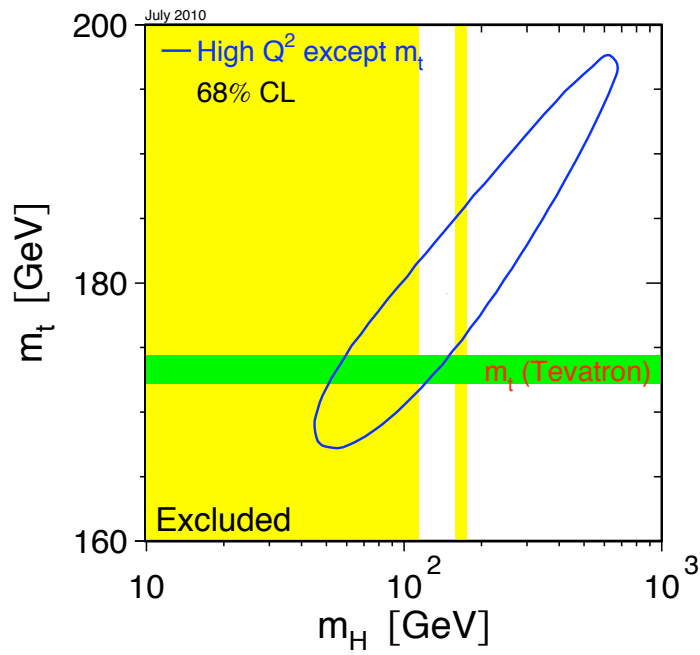
Figure 2.8: A fit of electroweak precision data to obtain predictions for the top-quark mass and the Higgs boson mass. Inputs are for example the W boson mass and the prediction is done with standard model calculations. The 68% confidence level contour in m_t and m_H for the fit to all high-Q^2 except the direct measurement of m_t which is indicated by the shaded horizontal band of $\pm$ 1 sigma width is indicated. The vertical bands show the 95% CL exclusion limits on m_H from the direct searches at LEP-II (up to 114 GeV) and the Tevatron (158 GeV to 175 GeV) [7].

3 The ATLAS Detector

The ATLAS Detector is one of the two particle detectors at the LHC that is designed as a device with a high discovery potential over a wide energy range (the other being the CMS detector) [14]. It is highly hermetic to offer good solid angle coverage employing an inner tracking device, electromagnetic and hadronic calorimetry and a muon system. The detector is forward-backward symmetric.

The design is typical for modern particle detectors since it allows to fulfill these general requirements:

- The energy and momentum of particles created in the collision or their decay products must be measured with high precision.

- The type of those particles must be identified. The identification principle is illustrated in Fig. 3.1.

- The detector must be able to trigger on events of interest since it is not possible and not desirable to record every collision event.
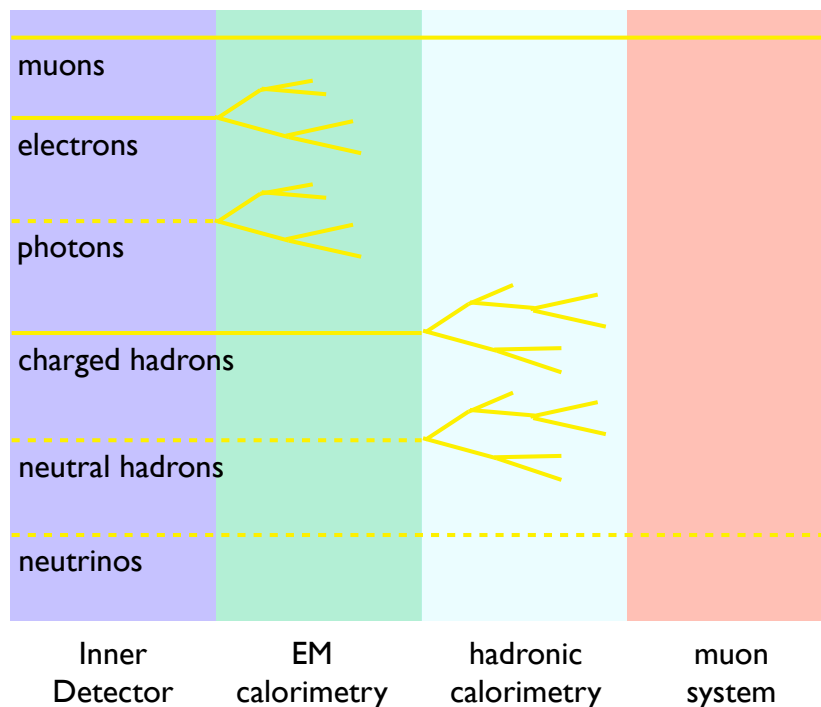
**Figure 3.1:** Schematic display of particle identification. Muons pass through the whole detector. Electrons and photons shower in the electromagnetic calorimeter and electrons also have a track in the Inner Detector. Hadrons shower mainly in the hadronic calorimeter (and are not stopped in the electromagnetic calorimeter) and neutrinos are not directly detected by any part of the experiment.

The distinctive feature of the ATLAS Detector is its air core toroid magnet system to deliver the magnetic field for the muon system. This allows for a thin solenoid magnet surrounding the Inner Detector cavity since the solenoid magnet is not required to provide the bending field for the muon system as well as for the Inner Detector. This puts less material in the way of muons and allows an accurate measurement of their momentum.

The layout of the ATLAS Detector can be seen schematically in Fig. 3.2. The subdetectors are described in the following chapters after introducing the coordinate system used. The Pixel Detector is described in more detail since it is most vital for b-tagging.

The ATLAS Detector weighs 7000 tonnes and is 44 m long and 25 m high.
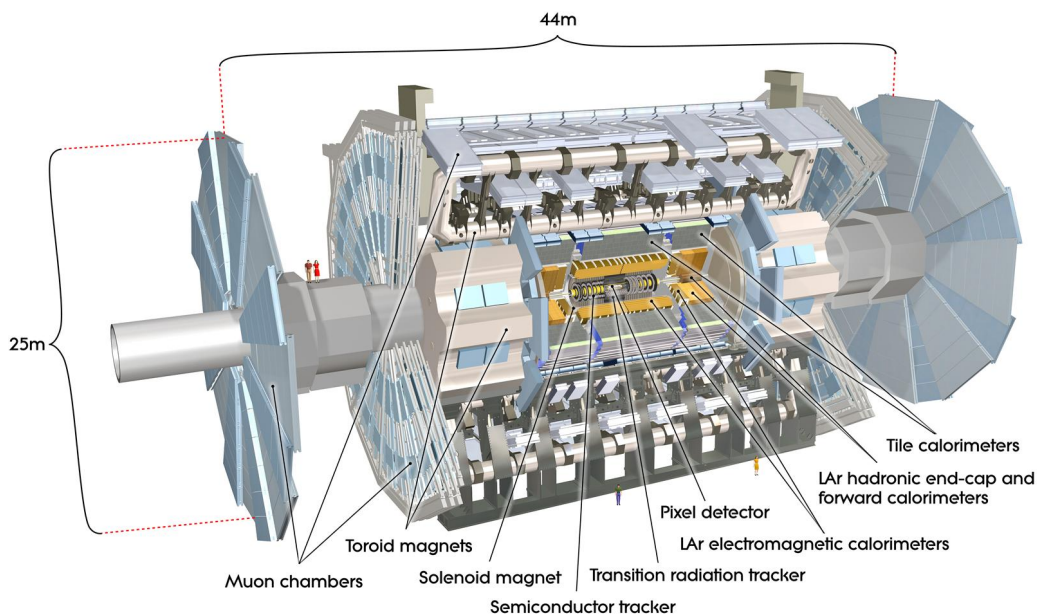
Figure 3.2: Schematic view of the ATLAS Detector with labels for the different subsystems [15].

3.1 Coordinate system

ATLAS employs different types of coordinate systems for different applications. The most intuitive one is a three dimensional right-handed cartesian coordinate system which has its origin in the interaction point. The positive x-direction points from the origin to the center of the LHC, the positive y-direction points upward and the positive z-direction points along the LHC tunnel. The y-axis is slightly tilted from perfectly vertical due to the tilt of the LHC tunnel.

Since the expected physical processes of interest are radially symmetric it is useful to introduce polar coordinates (r, φ) to describe the x,y-plane (also called the transverse plane). The z-coordinate is replaced by the Lorentz invariant pseudorapidity

$$\eta = -\ln \tan \frac{\theta}{2}$$

where θ is the azimuthal angle. The rapidity is defined as

$$y = \frac{1}{2} \ln \frac{E + p_L}{E - p_L}$$

with E being the particle energy and p_L being its momentum along the beam axis. The rapidity is equal to the pseudorapidity for mass-less particles (or approximately equal if the particle mass is much smaller than the momentum). In addition quantities like momenta and energy are often expressed in the transverse plane and are indexed with T (e.g. p_T denotes the transverse momentum which is the projection of the momentum in the transverse plane).

Coordinates of reconstructed track vectors are often characterized by the quantities d_0, the radial distance of the track vertex at the point of closest approach to the primary vertex also called transverse impact parameter and z_0 or $z_0 \sin \theta$, the longitudinal distance at the point of closest approach to the primary vertex also called longitudinal impact parameter. The signed significance of those quantities S_{d_0} and $S_{z_0 \sin \theta}$ is often used where the significance is the quantity divided by its measurement error and the sign is only assigned in combination with a jet and a primary vertex. It is positive if the angle between the jet and the line joining the primary vertex and the point of closest approach of the track and the primary vertex is less than 90° and negative otherwise.
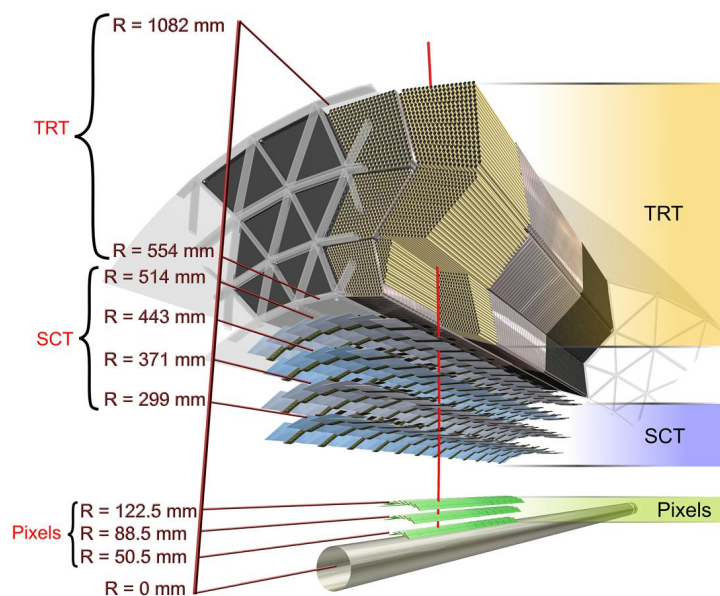
3.2 Inner Detector

The Inner Detector is a tracking device designed for high efficiency reconstruction of charged particle tracks traversing the detector. It consists of 3 subsystems, the Pixel Detector, the SCT Detector and the TRT Detector and a superconducting solenoid magnet delivering a field of 2 T. It is designed to detect tracks with a transverse momentum down to 0.1 GeV and to provide a resolution on d_0 that is ~ 12 μm [16] for high-p_T tracks under optimal conditions. It provides coverage up to $|\eta| < 2.5$ and is designed for a momentum resolution of $\sigma_{p_T}/p_T = 0.05\% p_T \oplus 1\%$. A schematic view of the Inner Detector can be seen in Fig. 3.3.

3.2.1 Pixel Detector

The Pixel Detector is a semiconductor based tracking device. It relies on silicon wafers with pixel implantations to gain two-dimensional information of hits induced by charged particles passing through the active material of the detector. A bias voltage of 150 V is applied to the sensor to deplete the silicon. Traversing charged particles create mobile charges in the depleted silicon material that are extracted and form the detection signal. The Pixel Detector has been designed for reliable pattern recognition and vertex reconstruction by providing high spatial resolution in a high track rate environment with low noise. Its performance is characterized in numerous studies (for example [18] for the tuning of the readout thresholds or [19] for the efficiency with cosmic ray data). A discussion of measurements of sensor performance parameters is given in Chap. 4.

The Pixel Detector consists of 1744 building blocks called modules. The modules are arranged to form a three-layered barrel part and three disks on each side of the detector respectively to form endcaps. The innermost layer is positioned at a radial

Figure 3.3: Schematic view of a slice of the Inner Detector barrel region. The distance of the different detector layers to the interaction point is indicated [17].

distance of 5.05 cm from the interaction point and is the most vital detector part for impact parameter or vertex based b-tagging (see Chap. 5).

Each module consists of a sensor tile that is connected to readout chips via bump-bonds. The readout chips are wire-bonded to a flexible polyimide printed-circuit board that holds the module control chip and the connector plug for the module. The module design can schematically be seen in Fig. 3.4.

The pixel sensor consists of a 18 mm x 62 mm tile of diffusion oxygenated float-zone silicon [21]. Implanted on the high-resistivity n-type bulk material is an array of 47232 diodes, realized as n^+ implantations on the readout side, with the complete back-plane of the sensor tile being highly p^+ doped to form the pn junction necessary for depletion of the sensor. One normal pixel implantation covers an area of 50 μm $\times$ 400 μm.

The pixel implantations are connected to 16 readout chips via bump-bond connections forming 46080 readout channels. This number is not identical to the number of sensor pixels. To provide full sensor coverage pixels in the middle of the module with regard to the short pixel edge are ganged since the readout chips do not cover this region actively. Readout channels are identified with pixels in the following. Pixels at the borders of readout chips with respect to the long pixel edge are also longer than the normal pixels with a length of 600 μm. The bump-bond connections were formed by two different vendors. 46.4% of the modules were bump bonded at IZM Berlin using an electroplated eutectic PbSn alloy [22]. The remaining 53.6% were bump-bonded at AMS Rome where indium bumps deposited on readout chip and sensor were connected using thermocompression [23].

16
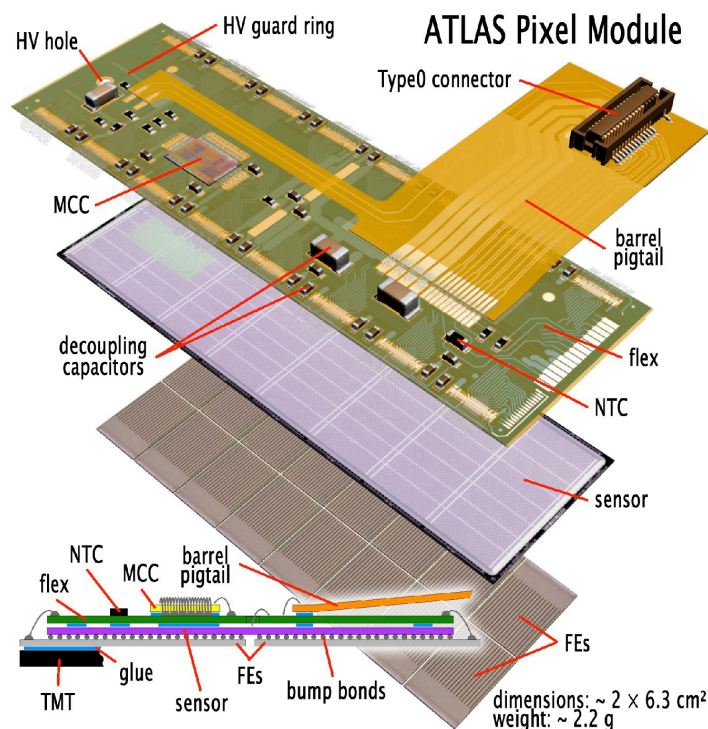
Figure 3.4: Exploded view of a Pixel Detector Module. The position of the bump-bonds is indicated in the profile view in the lower left of the figure [20].

3.2.2 SCT Detector

The SCT Detector is also a semiconductor based tracking device using single sided p-in-n technology with AC-coupled readout strips. The strips have a pitch of 80 μm and two 6 cm-long sensors are daisy chained in the barrel part of the detector whereas the endcap part uses radial sensors with constant azimuthal angle.

The SCT barrel is tiled by 2112 modules and organized in 4 layers. Each module has 4 sensor strips where the two sensors at the top of the module are slightly ($\pm$ 20 mrad from the geometrical center of all strips of the module) rotated relative to the two sensors at the bottom of the module to provide two-dimensional space-point information [24].

There are three different designs for the endcap modules of the SCT Detector. The designs are not detailed here, but they also use the rotated sensor strips to gain two-dimensional space-point information.

3.2.3 TRT Detector

The TRT Detector is based on polyimide straw tubes of 4 mm diameter filled with 70% Xe, 27% CO_2 and 3% O_2. They contain 31 μm thick anode wires made of tungsten coated with 0.5 μm - 0.7 μm gold centered with a precision of 300 μm in the straw tube.

The TRT straws are placed in barrel and endcap parts in a way that guarantees that a charged particle with $p_T > 0.5$ GeV and $|\eta| < 2.0$ traverses at least 36 straws

except in the barrel-endcap transition region. It also contains foils in-between the straws that provide transition radiation for electron identification.

3.3 Calorimetry

The calorimeters are devices that measure particle shower energies and stop particles that are not muons from reaching the muon system. The ATLAS calorimeters cover an azimuthal angle up to $|\eta| < 4.9$ and are partitioned into electromagnetic and hadronic calorimetry to provide identification of photons and electrons versus hadrons. The calorimeter systems are segmented into cells to provide directional information. A schematic view of the calorimeter view is given in Fig. 3.5 showing the distribution of the different calorimeter technologies.
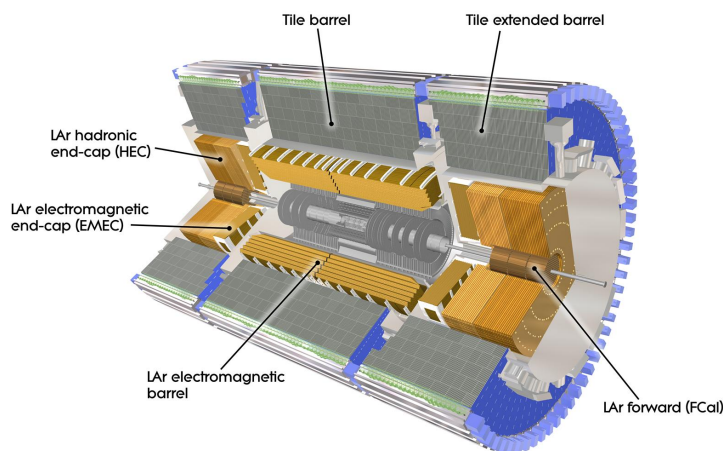
Figure 3.5: Schematic view of the calorimeter [25].

3.3.1 Electromagnetic calorimetry

The electromagnetic calorimeter is a lead-liquid argon detector with accordion-shaped kapton electrodes and lead absorber plates over its full coverage. The accordion shape guarantees full φ coverage without cracks and liquid argon was chosen due to its intrinsic linear behavior, its stability of response over time and its radiation-hardness. The electromagnetic calorimeter has a thickness of $\sim$30 radiation lengths. It is furthermore segmented into three layers in $0 < |\eta| < 2.5$ and two layers in $2.5 < |\eta| < 3.2$. The electromagnetic calorimeter is designed to provide an energy resolution of $\sigma_E/E = 10\%/\sqrt{E} \oplus 0.7\%$.

3.3.2 Hadronic calorimetry

There are three different hadronic calorimeters. The sampling tile calorimeter covers a range up to $|\eta| < 1.7$ using steel as the absorber and scintillating tiles as the active materials. The hadronic end-cap calorimeter extends out to $|\eta| = 3.2$ and uses copper-liquid argon. The forward calorimeter provides the rest of the coverage

and is based on copper-tungsten-liquid argon technology. The hadronic calorimeter is designed to provide an energy resolution of $\sigma_E/E = 50\%/\sqrt{E} \oplus 3\%$ in the central region and an energy resolution of $\sigma_E/E = 100\%/\sqrt{E} \oplus 10\%$ in the forward region.

3.4 Muon system

The muon system is designed to use the deflection of charged particles in the magnetic field created by the toroid magnets to provide muon tracking and triggering. The muon system uses four different detector technologies. The Monitored Drift Tubes (MDTs) and the Cathode Strip Chambers (CSCs) measure the muon tracks. The Resistive Plate Chambers (RPCs) and the Thin Gap Chambers (TGCs) provide trigger information. The distribution of these systems can be seen in Fig. 3.6.

The track parameters of muons are usually determined by the track parameters of a track reconstructed in the Inner Detector and matched to the muon track since the Inner Detector resolution is better for low p_T tracks. For high p_T tracks the muon system allows a better measurement. It is designed for momentum resolutions better than $\sigma_{p_T}/p_T = 10\%$ up to momenta of $p_T = 1$ TeV and the accessible momentum range goes up to ~ 3 TeV.
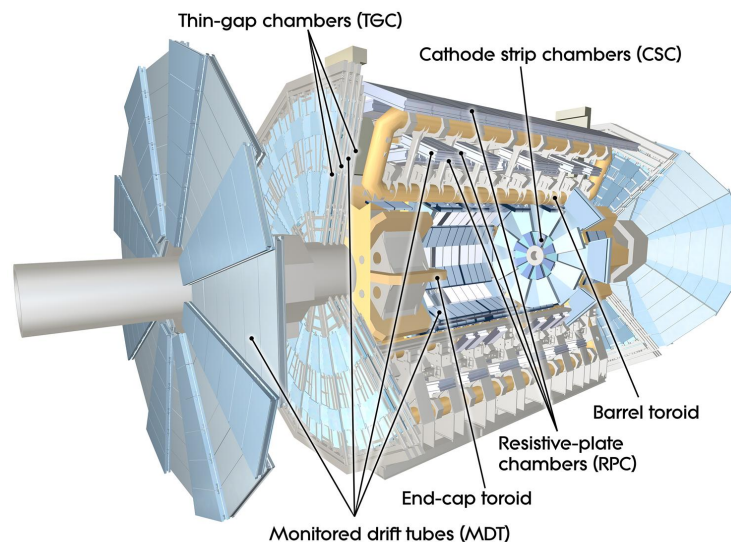
Figure 3.6: Schematic view of the muon system [26].

3.4.1 Tracking chambers

The MDTs cover a range of $|\eta| < 2.7$ in all but the innermost layer of the muon system. They consist of drift tubes filled with 93% Ar and 7% CO_2 gas and contain a tungsten-rhenium wire of 50 μm diameter. They deliver track coordinate measurements in the bending plane (η) with a resolution of 8 μm per tube layer which are combined with the measurement of the coordinate in the non-bending plane (φ) from the trigger chambers.

In high η regions the particle multiplicities are higher than ~ 150 Hz/cm^2 which is the limit for safe MDT operation, therefore CSCs are used in the first endcap layer

in the $|\eta| > 2$ region. They allow higher rates, the $|\eta|$ resolution is 60 μm and the φ resolution is 5 mm per plane. They are filled with 80% Ar and 20% CO_2.

3.4.2 Trigger chambers

The trigger chambers are optimized for fast tracking information with a focus on high rates over precision measurements of the track parameters. The barrel region ($|\eta| < 1.05$) is equipped with RPCs which detect ionizations of traversing charged particles in a mixture of 94.7% $C_2H_2F_4$, 5% Iso-C_4H_{10} and 0.3% SF_6 with parallel phenolic-melaminic plastic laminate plates at a distance of 2 mm.
The $1.05 < |\eta| < 2.4$ endcap region is equipped with TGCs. They are multi-wire proportional chambers with a 55% CO_2 and 45% n-C_5H_{12} gas mixture and a wire diameter of 50 μm.

3.5 Operation

The ATLAS Detector has taken data from March 2010 - November 2010 adding up to a total integrated luminosity of 45 pb^{-1}. The delivered luminosity and the total recorded luminosity are shown in Fig. 3.7.
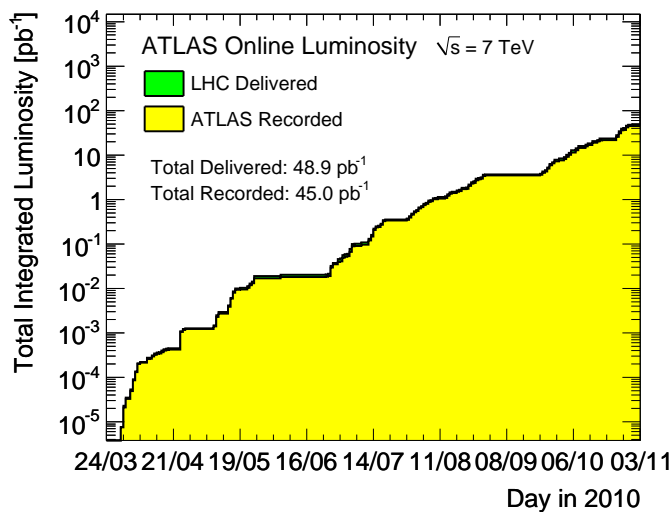
Figure 3.7: Development of the integrated luminosity over time in 2010. The instantaneous luminosity rises over time which is a sign of the successful commissioning of the LHC. Taken from the luminosity public results webpage[1].

Inner Detector			Calorimeters				Muon Detectors			
Pixel	SCT	TRT	LAr EM	LAr HAD	LAr FWD	Tile	MDT	RPC	CSC	TGC
99.1	99.9	100	90.7	96.6	97.8	100	99.9	99.8	96.2	99.8

Table 3.1: Luminosity corrected data taking efficiencies of the subdetectors.

---

[1]https://twiki.cern.ch/twiki/bin/view/AtlasPublic/LuminosityPublicResults

The recorded luminosity is slightly lower than the delivered luminosity due to ramp up procedures for different subdetectors like the Pixel Detector that are only done once the particle beam is declared to be stable. This means that the detectors are not in danger of significant damage that could occur if the beam would create unforeseen large particle densities for example by scraping the beam-pipe that surrounds it. This also means that the collisions that happen during this time cannot be recorded. In addition the subdetectors are not fully efficient due to non-functional regions or incidents like high voltage trips that have to be recovered during runtime. A summary of the luminosity weighted efficiencies for the data-taking period in 2010 is given in Tab. 3.1.

4 Pixel Detector sensor studies

In this chapter studies for the characterization of the performance of the sensors used in the Pixel Detector are described. The measurements were done with data taken in 2008 and they are currently being updated since they are expected to change with accumulated irradiation dose. The operating bias voltage for the Pixel Detector was 150 V when doing the measurements. A more detailed discussion of the measurements presented here can be found in [27].

4.1 Scans

Since the modules of the Pixel Detector are assembled and integrated into the ATLAS Detector it is not possible to measure sensor performance parameters under laboratory conditions[1]. For this reason the front-end electronics of the modules contain charge injection circuitry that allows known charges to be injected into the system of the semiconductor material and the readout electronics. Each readout cell has a low and a high injection capacity, the capacities are 7 fF and 40 fF respectively [28]. The injected charge is set by an 8-bit DAC controlling the applied voltage to charge the capacitor allowing an injection charge range up to ∼200k electrons.

The response of the detector to these injected charges can be measured. The injection/measurement cycle is typically repeated on the order of 100 times to gain measurement statistics and the whole process is called a scan. A characteristic scan conducted on the Pixel Detector is the threshold scan where the injection charge is increased from a low value to a high value and the response of each pixel is measured. This results in an S-shaped curve of hits collected versus injected charge. The threshold scan is used to characterize the readout threshold of the pixels as well as the noise where the center of the S-shaped curve is a measure of the threshold and the width is a measure of the noise [18].

Scans typically need times on the order of some minutes up to several hours depending for example on the amount of different injection charges used in the scan. Another aspect that influences the measurement time is the mask staging. The front-end electronics of the Pixel Detector cannot read out every pixel at the same time due to limited buffer sizes. Therefore a masking pattern is used that typically enables every 32th pixel and disables the readout channels of the rest. In a mask step the pattern is then shifted so that after 32 mask steps each pixel of a module has been scanned. More details on the scan implementation can be found in [29].

4.2 Disconnected bumps

It is crucial that the bump connections are intact. Every disconnected bump-bond connection causes a dead detector region that decreases the performance of the detector. The amount of disconnected bumps is monitored over time to ensure sensor

---

[1]for example by powering a single module in a controlled environment and measuring its response to a radioactive source as was done during module production

quality and to gain valuable experience for future upgrades of the Pixel Detector. The amount of disconnected bumps might increase for example due to thermal cycles of the detector where the temperature in the module changes.

Cross-talk scans are used to find the disconnected bump connections. A high charge of multiple times the threshold of the readout electronics is injected into the two pixels neighboring a read out pixel along the long edge. The threshold is set to approximately 4 ke and the injected charge is 200 ke. The neighboring pixels are capacitively coupled over the sensor and therefore a cross-talk charge is induced in the read out pixel [30]. The cross-talk is ∼3.5% which results in an induced charge of 7 ke per injected pixel for normal pixels. For long pixels it is higher since they have a higher capacitance. The preamplifiers of the pixels not read out are disabled which increases the cross-talk. The charge chosen is high enough so a single injected pixel is sufficient to cause an over threshold charge in the read out pixel which prevents being biased by sensor edges (where only one neighboring pixel exists). By injecting both neighboring pixels a systematic error from the cases where one of the neighboring pixels is disconnected is also avoided. The injections are repeated 100 times. If charge is collected the bump bond connections have to be intact since the cross-talk in the readout electronics is low due to shielding. A scan for a badly damaged module is shown in Fig. 4.1. For an intact bump connection 100 collected hits are expected in a read out pixel where for a disconnected pixel 0 hits are expected. Pixels with 0 hits in the cross-talk scan are therefore disconnected bump candidates.
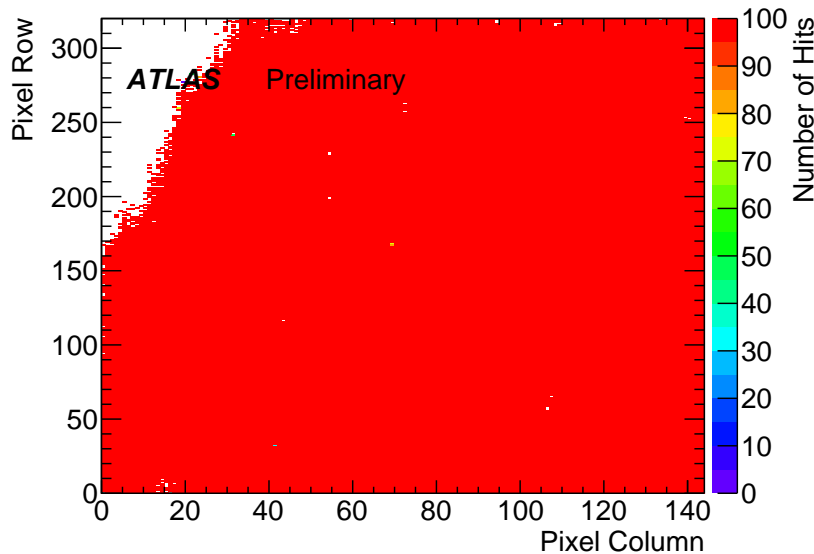
Figure 4.1: Module with disconnected bump-bond connections. An especially bad module with many disconnected bump-bond connections has been chosen since it demonstrates that the regions of failure are often localized at corners of modules which is compatible to handling mistakes. Row and column are the local coordinates of a module identifying pixel positions. The white color marks pixels with 0 hits.

To refine the measurement an analog scan is also conducted. This scan injects charge into a pixel and reads out the same pixel. If the readout electronics are damaged or there is other general damage to this readout channel no hits are registered in the

analog scan. These analog dead pixels will also register no hits in the cross-talk scan but this does not indicate a disconnected bump so analog dead pixels are removed from the disconnected bump candidates.

Furthermore a threshold scan is conducted. The threshold scan measures, among other things, the noise of the pixels. The noise of a pixel is influenced by its capacitance so that a connected pixel has a higher noise than a disconnected one. Fig. 4.2 shows the noise distribution for the disconnected bump candidates and for all pixels under study. The noise of normal pixels peaks at ∼160 electrons. The additional structure in the plot is due to the special pixel types like the long and the ganged pixels that have a higher noise due to their higher capacity. The disconnected bump candidates noise peaks at ∼120 electrons. A cut on the noise to identify disconnected bumps is not done since the peaks are close, but the tail in the disconnected bump distribution is rejected by requiring that the noise of a disconnected pixel must be less than 300 electrons.
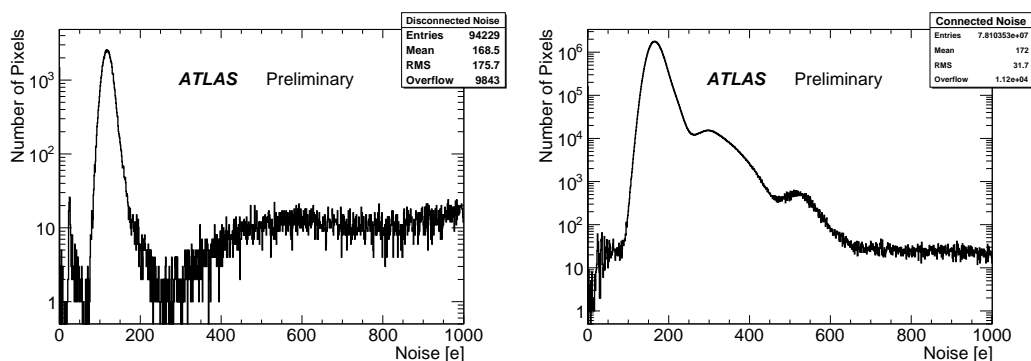

Figure 4.2: Distribution of noise from a threshold scan for disconnected bump candidates on the left and for all scanned pixels on the right.

This analysis results in a total of 76980 disconnected pixels in 1697 modules. Not all modules could be scanned since some of them were having temporary or permanent problems mainly related to issues with electrical, optical or cooling services. The ratio of disconnected pixels to total number of pixels is 0.1%. 94.8% of the total number of disconnected bumps are AMS type bumps, the rest are IZM type bumps. The integrated distribution of disconnected bump bond connections is shown in Fig. 4.3 where an accumulation of disconnected bumps on chip edges is visible. The larger connected areas are from few badly damaged modules.

4.3 Depletion voltage

Another study to show the sensor quality is a measurement of the depletion voltage (the voltage necessary to fully deplete the silicon along its 250 μm thickness). The charge collection efficiency is reduced if the sensor is not fully depleted so the bias voltage applied to the sensor should be at least equal to the depletion voltage. This quantity will also be monitored over time since it is expected to change with accumulated radiation dose.

Two different measurements of the depletion voltage were conducted. One measurement relies on cross-talk scans similar to the disconnected bumps measurement. The
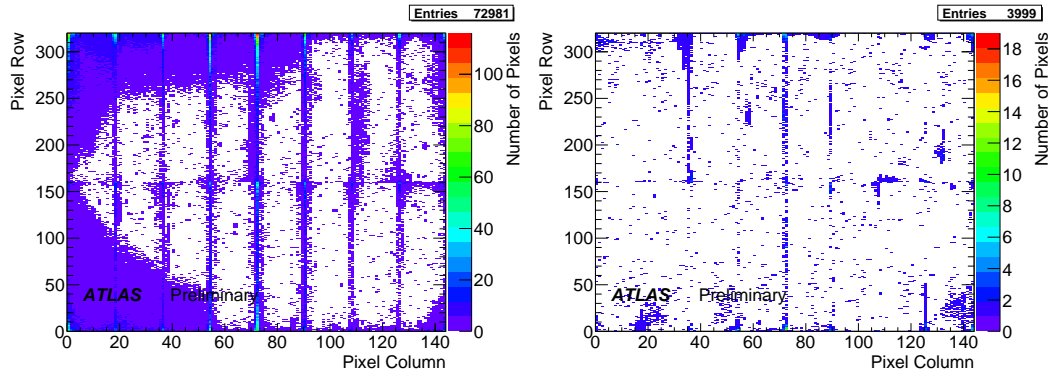
Figure 4.3: Distribution of disconnected bump bond connections for AMS bump bonded modules on the left and for IZM bump bonded modules on the right. An accumulation of disconnected bump bond connections on the edges of the readout chips is visible.

other measurement uses the noise occupancy of the detector to find the depletion voltage.

The magnitude of the cross-talk depends on the capacitance of the pixel implantations to ground (or to the edge of the depletion zone facing the pixel implantation) and to its neighboring implantations. Therefore the cross-talk in a depleted sensor is lower than the cross-talk in an undepleted sensor. Examples of the growth and shape of the depletion zone in the transition region between no depletion and full depletion when changing the applied bias voltage can be found in [31]. A cross-talk scan with an injection charge of 60 ke is used to find the depletion voltage. The preamplifiers of the pixels that are not being read out are turned on to decrease the cross-talk to ∼2% which means that the induced charge is 1.2 ke which is less than the readout threshold in a depleted sensor. In an undepleted sensor the charge is high enough to induce cross-talk hits.

The voltage is changed in steps of 2 V and at each voltage step a cross-talk scan is performed. An example cross-talk scan at 46 V bias voltage is shown in Fig. 4.4. A ring structure is visible which means that the module is partly depleted. It is possible that doping inhomogeneities form during the growth process of the silicon wafers which cause these structures. A grid structure of hits is also visible which is caused by injection crossings that happen due to the mask steps mentioned before. Since the depletion voltage is a module quantity it is not important to consider every pixel so the pixels which are expected to show the grid structure are masked from the analysis. This leaves a total of 35840 analyzed pixels for each module.

When approaching the depletion voltage with the bias voltage a drop in the total number of registered hits during the cross-talk scan is expected which translates to a rise in number of pixels with missing hits (the total number of injections subtracting the number of registered hits). The number of missing hits is displayed for an example module in Fig. 4.4. To find the depletion voltage a linear fit is performed to the rising part of the curve for each module. The intercept of the linear fit with the high plateau is the depletion voltage. The depletion voltages measured with this method for 1685 modules are shown in Fig. 4.6. The negative bin contains 24 modules for which the scan failed or the fit did not yield meaningful results.
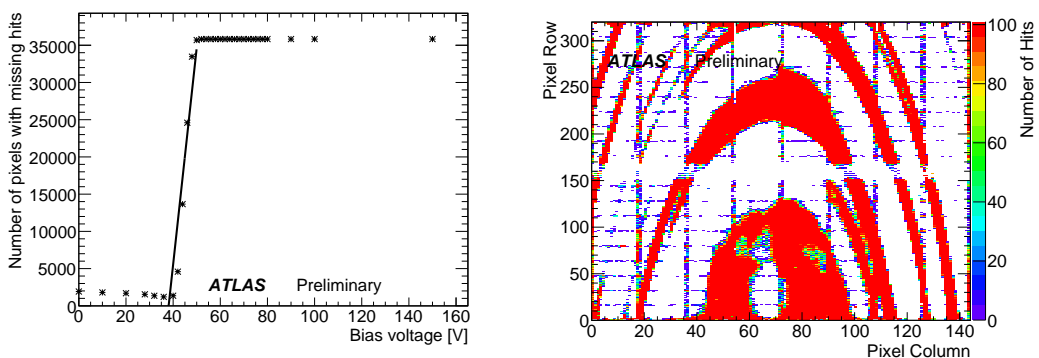
Figure 4.4: On the left the result of the cross-talk missing hits for different bias voltages is shown. The linear fit to the steep part of the distribution is also indicated. On the right the distribution of hits for the same module is shown at an applied bias voltage of 46 V. The white color marks pixels with 0 hits.

By means of the noise occupancy it is also possible to measure the depletion voltage. The noise depends on the detector capacitance as well: a depleted sensor is less noisy than an undepleted sensor. To measure the noise occupancy the scan machinery is not needed but data is taken with a random trigger applying different bias voltages. Similar to the cross-talk scan based method the noise occupancy drops significantly when the sensor is getting depleted.

In principle the single pixel occupancy could directly be used as a measure for the depletion voltage. For practical reasons only a limited amount of triggers could be taken during the time available for the measurement. 200k events were recorded for each step in bias voltage which leaves most pixels without hits even when approaching an undepleted sensor. Furthermore the noise occupancy gets too high and blocks the readout drivers from taking data which means that the voltage cannot be lowered indefinitely while still taking data in a sensible way.
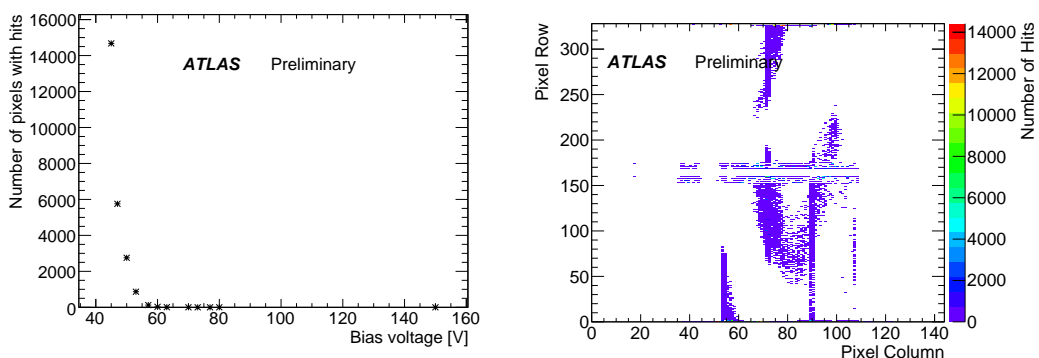

Figure 4.5: Number of pixels with hits on the left. On the right an example hitmap for a bias voltage of 50 V. Some pixels have a high noise in the hitmap which explains the scale of the plot but most pixels with hits have few hits. The white color marks pixels with 0 hits.

For those reasons the number of pixels with hits is chosen as the discriminant. When

approaching the undepleted case the amount of pixels showing hits in 200k events rises as shown in Fig. 4.5. Fig. 4.5 also shows a hitmap example which shows a structure similar to the one in Fig. 4.4. The resulting distributions of number of pixels with hits differ in total number of pixels and in slope so a global cut on any of those variables would not lead to a satisfactory measurement of the depletion voltage. Instead the second derivative is calculated and a global cut on the derivative is applied. The bias voltage at which the second derivative passes a global threshold is the depletion voltage. The threshold should be chosen as low as possible but a threshold of 0 is prone to statistical fluctuations. The threshold is set to 3 V^{-2}. The smallest bias voltage step size is 3 V so a second derivative above 3 V^{-2} corresponds to at least 27 more pixels with hits than before the voltage step.

The measurement results for 1625 modules are shown in Fig. 4.6. The negative bin contains modules where the measurement failed. A comparison of the two measurement is shown in Fig. 4.7. The measured spread of 4 V is comparable with the voltage step size which is 3-4 V in the noise occupancy based measurement.
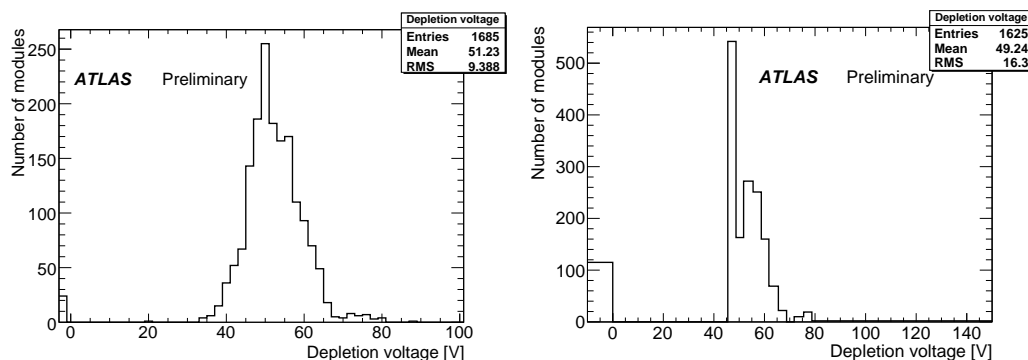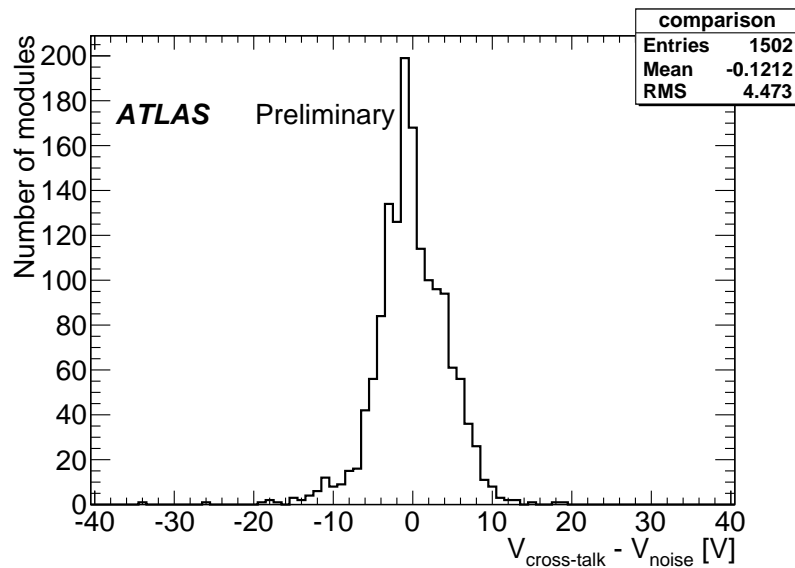

Figure 4.6: Resulting depletion voltage from the cross-talk scan on the left. Resulting depletion voltage from the noise occupancy based method on the right.

It should be noted that the measurement is cumbersome since the data-taking system is often blocked by high occupancies and modules that cause these problems have to be disabled by hand so the time needed for the measurement is high. The cut on the second derivative is also chosen in an arbitrary way which is unsatisfactory so the cross-talk method is the preferred method of measuring the depletion voltage.

4.4 Breakdown voltage

The breakdown voltage is the bias voltage at which the depletion zone of the sensor breaks down and the sensor becomes conductive [32]. To measure the breakdown voltage IV-curves are taken for groups of 6 or 7 modules. The IV-curve is the current measured at the power supply for different applied bias voltages. Each group is supplied by a single power supply.

The bias voltage is changed in steps of 10 V starting at 0 and increasing up to 600 V. The current output is limited to 2 mA to protect the modules which is sufficient to measure the breakdown voltage. A typical IV-curve is shown in Fig. 4.8 showing the breakdown of the module at high voltages. The breakdown voltage is found

**Figure 4.7:** Comparison of the depletion voltages from the two methods.

by performing a linear fit to the last points of the IV curve and extrapolating the intercept point with the voltage axis.

Results for the breakdown voltages measured with this method are shown in Fig. 4.9. There are a total of 272 power supply groups but one of them could not be measured due to a problem in the readout chain. It should be noted that the measured breakdown voltage is always the breakdown voltage of the module with the lowest breakdown voltage in a power supply group, so the breakdown voltage for most modules is higher than the measured values. However the mean measured breakdown voltage is 480 V which is safely above the applied 150 V in current operation. The breakdown voltage will change with accumulated irradiation dose and will be monitored to guarantee safe detector operation.

4.5 Leakage current

In addition [27] shows a study quantifying the residual leakage current through the sensor which influences the detector noise. It is below the measurement accuracy of 0.125 nA for 98.5% of the pixels. This quantity will also change with accumulated radiation dose and the described method can be used to assess the detector status over time.

A group of 2880 pixels is read out by a single front-end which contains the readout electronics and the injection circuits. It also contains a MonLeak ADC circuit which can be digitized over a range of 0.125 nA to 128 nA in steps of 0.125 nA. This allows a pixel-by pixel measurement of the leakage current. A comparator is used to measure the current and since only one pixel per front-end can be measured at a time with this circuit a binary search algorithm with a starting value close to the expected leakage current is used to speed up the measurement. The results of the MonLeak measurement with modules with known problems excluded and split by
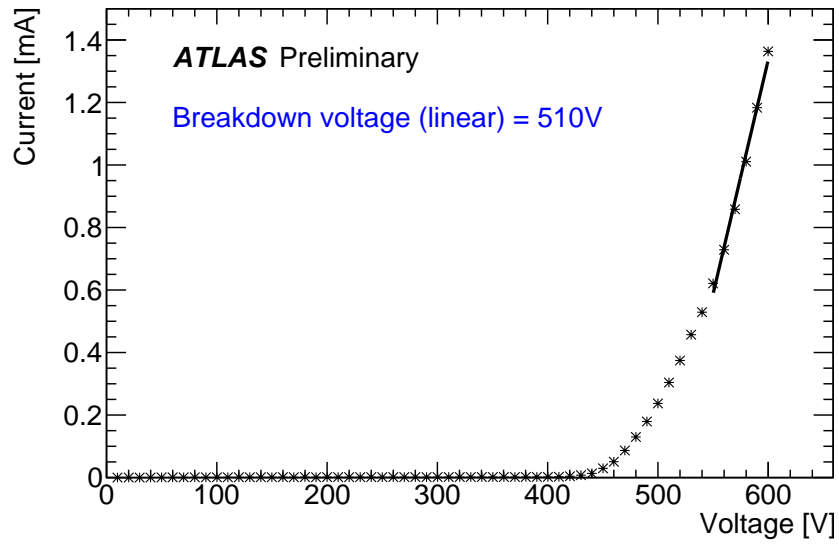
Figure 4.8: IV curve for a module with linear fit to the last five points of the curve and extrapolated breakdown voltage indicated.

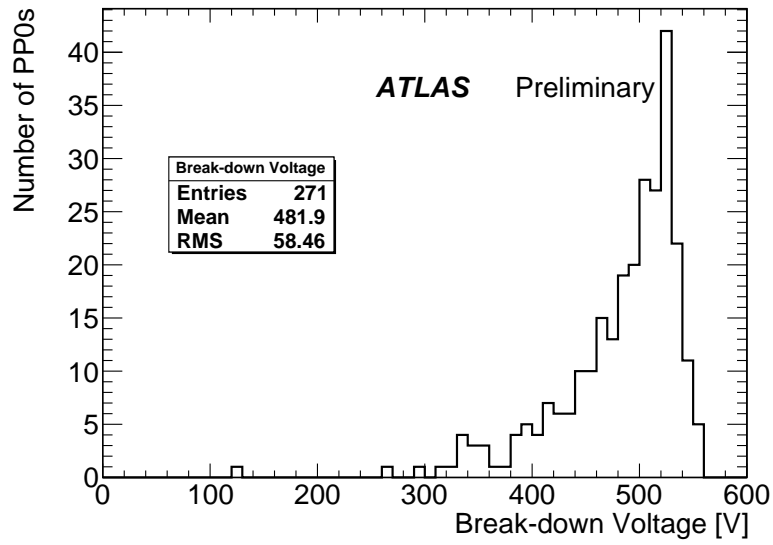bump connection type is shown in Fig. 4.10.

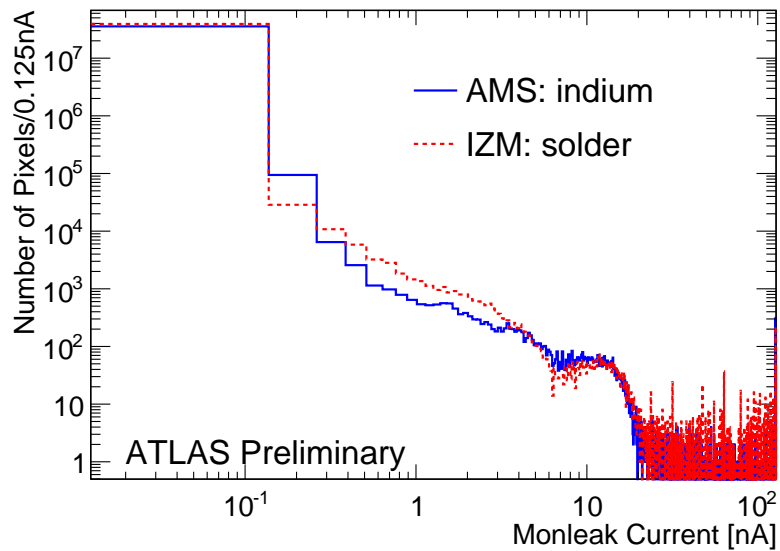**Figure 4.9:** Measured breakdown voltages.

Figure 4.10: Measured leakage currents with the MonLeak scan.

5 B-Tagging with the ATLAS Detector

This chapter describes a set of b-tagging algorithms that are used in the ATLAS experiment. The SV0 tagger and the JetProb tagger are described in detail since these are the two taggers that have been calibrated at this point. The working principle of the advanced taggers is also outlined.

5.1 Physics motivation

A b-tagging algorithm uses characteristics of b-quark decays to identify (tag) reconstructed jets that contain such decays. This aids in the selection of many interesting signatures. Top-quarks for example decay via the channel $t \to Wb$ in >99% of the cases [33], so b-tagging can be exploited to enhance events containing top-quarks against the background. Some details on the application of b-tagging for this purpose are shown in Chap. 6.8. Other prominent signatures that make use of b-tagging algorithms are for example the Higgs boson decay channel $H \to bb$ where the Higgs boson is produced in association with top-quarks as shown in Sec. 2.5.

5.2 Description of b-tagging algorithms

Two properties of the decays of b-quarks are used for b-tagging and they define two classes of algorithms that are uncorrelated [34]. These are the displacement of the b-quark decay from the primary interaction and the semileptonic decay of the b-quark and the kinematics of the resulting muon. Both classes depend on tracks in jets, so a track-to-jet association is needed. Details about this association as well as a more detailed description of the physics objects can be found in Sec. 6.1.

The independence of the two classes allows cross-checks and calibrations as will be detailed in Sec. 5.4, the algorithms are explained in the following.

5.2.1 Impact parameter based taggers

Most of the b-tagging algorithms exploit the fact that most created b-quarks travel a distance which is measurable with the Inner Detector before they decay. The mean life-time of a $B^{\pm}$ meson is (1.638 ± 0.011) ps [2] which allows it to travel a mean length of 5 mm if produced with 50 GeV transverse momentum as explained in Sec. 2.5. This can be resolved with the Inner Detector.

Impact parameter based taggers exploit this behavior by requiring the jet candidate for tagging to contain tracks that are significantly displaced from the primary vertex. The primary vertex is a measurement of the collision point of the two protons. The displacement reflects that these tracks are likely not prompt tracks from the primary vertex but originate from a secondary particle decay. The displacement is quantified by the tracks signed transverse impact parameter significance $S_{d_0} = d_0/\sigma_{d_0}$ where d_0 is the distance of the track to the primary vertex at the point of closest approach in the transverse plane and σ_{d_0} is the associated error on the measurement.

Example distributions for tracks in jets of different flavor are shown in Fig. 5.1. A likelihood ratio formalism to transform this quantity into a jet tagging weight is detailed in [34]. Three b-tagging algorithms exist that use this information: The IP1D tagger uses the longitudinal impact parameter. The IP2D tagger uses the transverse impact parameter. The IP3D uses both the longitudinal and the transverse impact parameter.
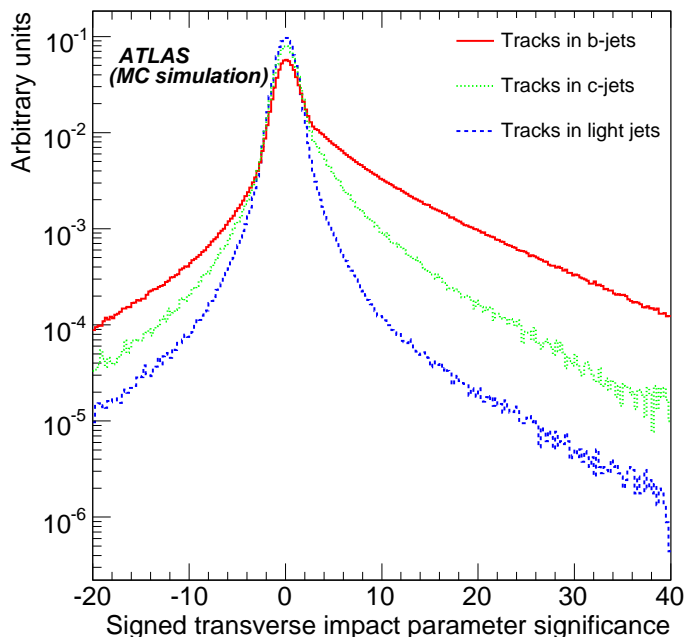
Figure 5.1: S_{d_0} distribution for different jet flavors. The distributions are from an older study derived from simulation at 14 TeV center-of-mass energy. The discriminating power of the variable is clearly demonstrated [34].

The JetProb tagger is also based on the signed impact parameter significance but follows a different approach: The S_{d_0} distribution for tracks in light jets is approximately symmetric along the axis defined by S_{d_0} and the negative side of the distribution is dominated by light jets. The negative side of the distribution is therefore reflected to the positive side and fit with a resolution function $R(x)$ which is given by

$$R(x) = p_0 e^{-x^2/2p_1^2} + p_2 e^{-x^2/2p_3^2} + e^{-p_4 - p_5 x} + e^{-p_6 - p_7 x} \tag{5.1}$$

with free parameters p_0-p_7. The S_{d_0} of a given track is then compared to this resolution function to assign a probability for this track originating from the primary interaction. The probability is given by

$$P_{trk_i} = \int_{-\infty}^{-|S_{d_0}^i|} R(x) dx$$

for the ith track in a jet. An example resolution function from a fit to a subset of the 2010 data is given in Fig. 5.2. A jet tag weight P_{jet} is then formed from the

individual track probabilities by doing the combination

$$P_{jet} = \prod_{i=1}^{N} P_{trk_i} \sum_{j=1}^{N-1} \frac{\left(-ln\prod_{i=1}^{N} P_{trk_i}\right)^j}{j!}$$

where N is the total number of tracks in the jet considered by the JetProb tagger. The cuts for tracks that are considered by the JetProb tagger are detailed in [35]. P_{jet} implies a probability for the jet not being a light jet and therefore a *b*-jet or a *c*-jet and usually $-\log_{10} P_{jet}$ is used as the tagging weight. Fig. 5.2 shows the fit of the resolution function to data and a comparison of the tagger weight on a subset of the available data to simulation.
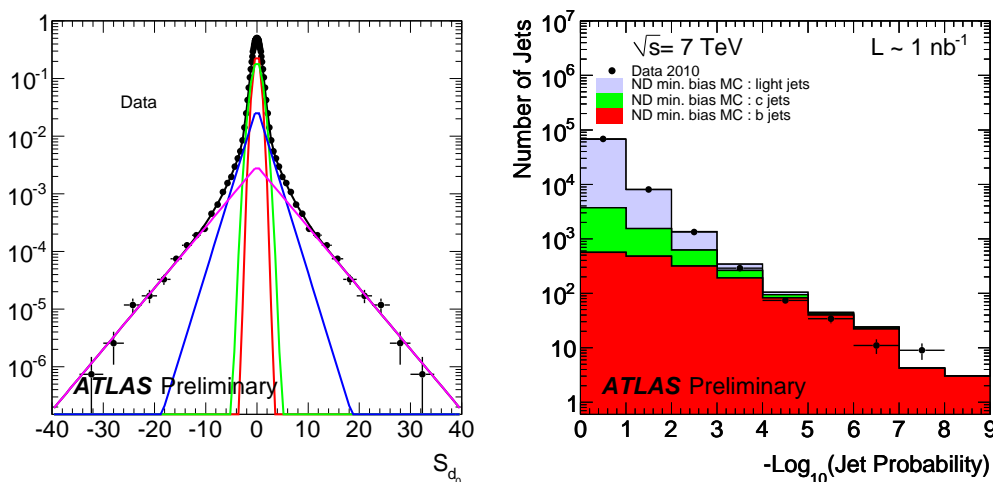

Figure 5.2: Left: JetProb resolution function fit result on data with colors indicating the different summands in Eq. (5.1). Right: JetProb tagger weight comparison of data to simulation. The different jet flavors are indicated by the colors [35].

5.2.2 Secondary vertex based taggers

Secondary vertex based *b*-tagging algorithms directly reconstruct the decay vertex of the *b*-quark decay and use properties of the reconstructed decay vertex to tag *b*-jets. The SV0 algorithm starts with a track selection that ensures basic track quality as detailed in [36] and fits two-track vertices that are displaced from the primary vertex. It then rejects two-track vertices that have a mass consistent with a K_S^0 meson, a Λ^0 baryon or a photon conversion. Additionally vertices that are displaced by the radius of one of the Pixel Detector layers are rejected to suppress material interactions. An inclusive secondary vertex is then fit from the remaining two-track vertices and then the attempt to reincorporate the tracks failing the selections into the inclusive secondary vertex is made.

The discriminating quantity used for tagging is the 3-dimensional signed decay length significance $L/\sigma(L)$, where L is the distance between primary and reconstructed secondary vertex and $\sigma(L)$ is the associated error. The sign is derived similar to the

sign of the impact parameter significance. Fig. 5.3 shows the $L/\sigma(L)$ distribution for different jet flavors and demonstrates the discrimination power of this tagging algorithm on simulation. It also shows a comparison to a subset of the data collected in 2010.
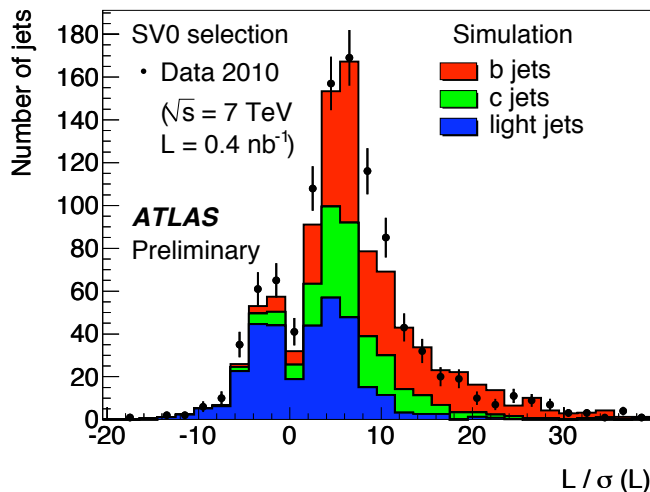
Figure 5.3: SV0 tagger weight comparison of data to simulation. The different jet flavors are indicated by the colors.

The SV1 tagger also reconstructs secondary vertices. It uses the invariant mass of the fitted vertex, the ratio of energy in the vertex compared to the total energy in the associated jet and the number of two-track vertices used for the inclusive vertex. The first two quantities are used as a 2-dimensional input and the third quantity is treated as a separate 1-dimensional input. The SV2 tagger uses all three quantities as a 3-dimensional input.

5.2.3 Advanced taggers

Advanced taggers show a better performance in general. The drawback is that they are less robust than the taggers shown so far so they are still in the commissioning phase and no calibration was derived for them as of this point.

The SV1 likelihood is combined with the IP3D likelihood to form the IP3D+SV1 tagger. The likelihoods are added to form the combined tagger and it is called the baseline tagger. The name baseline tagger should not be deceiving since the tagger is not calibrated yet and can therefore not be used in physics analyses that rely on the knowledge of the tagger performance (which most analyses do).

Another algorithm that can be used standalone or in combination with the IP3D tagger is the JetFitter algorithm. b-hadrons decay predominantly into c-hadrons which then decay themselves. The JetFitter algorithm exploits this fragmentation of the b-hadrons and does not require a single secondary vertex fit. Instead it assumes that the b-hadron and the c-hadron decay vertex are on the direction of flight of the original b-hadron and then reconstructs the cascade decay.

5.2.4 Soft lepton taggers

Soft lepton taggers exploit the decay kinematics of leptons from semileptonic b-hadron decays. The tagging efficiency of these taggers is limited to $\sim 21\%$ due to the branching fractions of the b-hadrons (including the cascade decay $b \rightarrow c \rightarrow l\nu_l X$). The soft muon tagger and the soft electron tagger use the p_T^{rel} quantity similar to the way it is used in the p_T^{rel} method detailed in Sec. 5.4.1. They use a likelihood ratio to discriminate between b-jets and background which is derived from the p_T^{rel} shapes from simulation. Consequently the p_T^{rel} method cannot be used to calibrate them and they are not discussed in detail. More details can be found in [34] and some data to simulation comparisons are collected on the ATLAS public results web page[1].

5.2.5 Event display

Fig. 5.4 shows an event display that visualizes the b-tagging concept. Event displays are a representation of the activity in the different parts of the detector with superimposed reconstructed objects. On the top left the primary interaction point is shown with orange lines representing the reconstructed tracks. The red track is a muon track. The cone represents the reconstructed jet built from the calorimeter signals that can be seen as yellow boxes in the lower left part of the figure. The tracks associated to the jet on the top right are consistent with originating from a secondary vertex. The presence of a muon also hints to the jet stemming from a b-hadron.
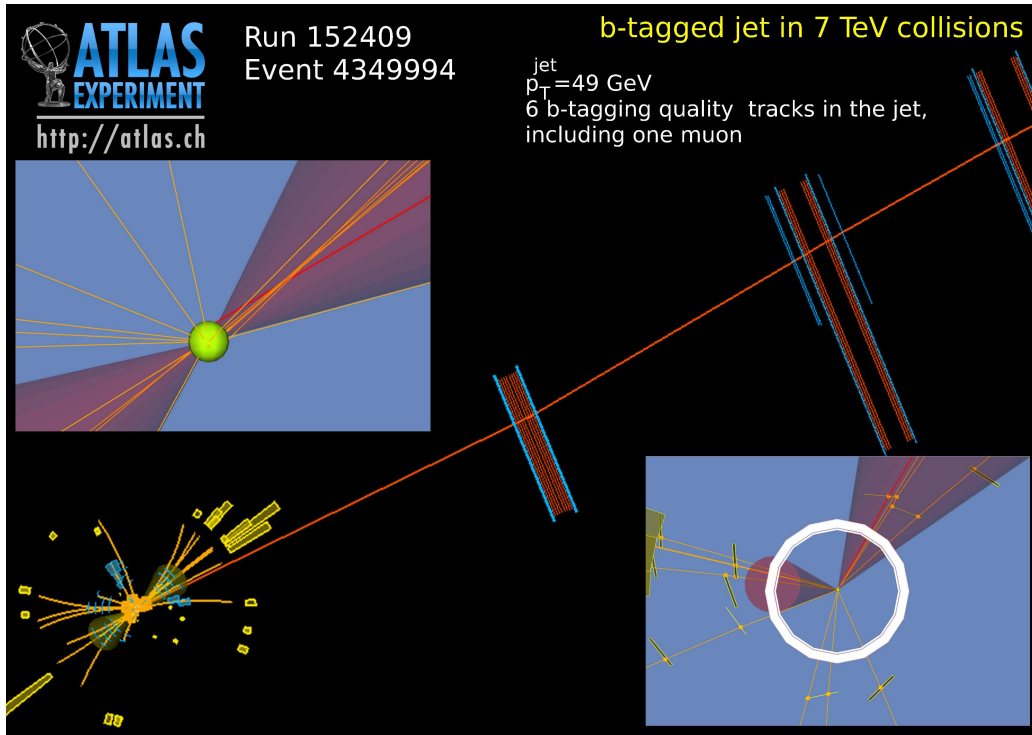
The different tagging principles can be seen in this figure: A secondary vertex can be reconstructed and some of the associated tracks are also displaced from the primary vertex which means their impact parameter is high. The flight direction of the muon from the decay is displaced from the central jet direction which would allow soft lepton tagging with the p_T^{rel} quantity.

5.3 Performance of b-tagging algorithms

Track reconstruction is not 100% efficient and track parameters can only be resolved with a certain accuracy as stated in Sec. 3.2. Therefore not all jets containing a b-quark decay can be tagged. On the other hand, processes like c-quark decays or track parameter mismeasurements can cause the reconstruction of displaced tracks and vertices that do not stem from a b-quark decay. This results in a b-tagging efficiency $\epsilon_b = N_{b,tag}/N_b$ that is less than 1 and fake rates $\epsilon_c = N_{c,tag}/N_c$ and $\epsilon_l = N_{l,tag}/N_l$ that are greater than 0. Here N is the total number of tagable jets that contain a b-hadron, a c-hadron or a light hadron (not a b- or c-hadron) and N_{tag} is the respective number of tagged jets of that flavor which is a subset of N. The requirement that the jet be tagable is defined by a certain kinematic range, for example the jet has to be inside the coverage of the Inner Detector. Oftentimes the rejection is quoted which is the inverse of the fake rate.

These efficiencies depend on jet parameters like p_T, η or number of tracks in the jet and on the tagger operating point that is chosen for b-tagging. Fig. 5.5 demonstrates the general trends of these dependencies

---

[1] *https://twiki.cern.ch/twiki/bin/view/AtlasPublic/FlavourTaggingPublicResultsCollisionData*

Figure 5.4: Event display showing the working principles of *b*-tagging algorithms. Explanations are given in the text.

The tagging efficiency drops when approaching low p_T and it also drops when approaching high p_T. The low p_T drop is due to two effects. On the one hand the mean *b*-hadron lifetime depends on its momentum as given by Eq. 2.2. Therefore a *b*-hadron with low p_T is likely to decay close to the interaction point which makes resolving the displaced tracks and vertices increasingly difficult. On the other hand low p_T jets contain low p_T tracks and the impact parameter resolution decreases for these tracks due to multiple scattering of the tracks.

Decay products from high p_T *b*-hadrons are collimated and have a high track density which complicates the pattern recognition. Due to their boost the hadrons could also decay close to or even after the innermost layer of the Pixel Detector which further decreases the tagging performance.

At high $|\eta|$ the performance also drops due to the diminished impact parameter resolution. This is partly due to an increased amount of material the particles have to traverse which increases the chance of interactions. The performance is also affected by the increased distance of the interaction region to the first layer of the Pixel Detector. In addition the endcap parts of the Pixel Detector are not of the same quality as the barrel parts, for example the module shown in Fig. 4.1 is in the endcap part. Fig. 5.6 illustrates the distances in the Inner Detector and its coverage for particles with different η.

Precise knowledge of those performance parameters is vital when using *b*-tagging algorithms for example in a cross-section measurement: If the *b*-tagging efficiency is used in the event selection it directly influences the measured event yield and must be used as a correction factor to obtain the cross-section.
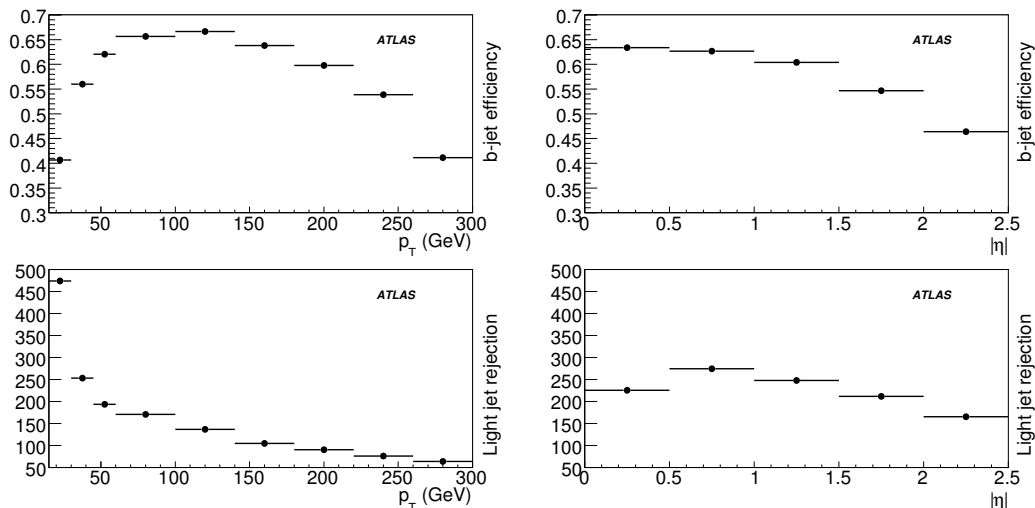
Figure 5.5: B-tagging efficiency and purified light jet rejection obtained with the IP3D+SV1 tagging algorithm at a tagger weight cut of 4 for $t\bar{t}$ events plotted against p_T and η [34]. The simulation is from an older study with 14 TeV center-of-mass energy so the single values are outdated, but the trend is clearly visible. The trend is similar for the other tagging algorithms.

It cannot be assumed a priori that the simulation models the b-tagging performance perfectly. Figs. 5.2 and 5.3 indicate that the agreement of the tagger weights in data and simulation is not perfect. On a more basic level it is also known that input quantities to the b-tagging do not agree perfectly between data and simulation. An example are the track signed impact parameter distributions as shown in Fig. 5.7. More studies of b-tagging input quantities are summarized in [37]. The b-tagging performance has to be measured on data due to these known mismatches. The following section explains the different methods that are used to do this performance calibration.

5.4 Calibration of b-tagging algorithms

This section shows different methods to measure the b-tagging performance. In particular the b-tagging efficiency measurement with the p_T^{rel} method is detailed. The methods shown can be used to calibrate the impact parameter based and secondary vertex based taggers with the exception of the $t\bar{t}$ based calibration methods which can be used to calibrate all taggers.

5.4.1 Efficiency measurements

There are four different methods currently used to measure the b-tagging efficiency ϵ_b for the different b-tagging algorithms, they are detailed in the following.

p_T^{rel} method

The p_T^{rel} method uses the leptonic decay of b-quarks $b \rightarrow \mu\nu_\mu X$ to measure the b-tagging efficiency. The p_T^{rel} of a muon in a jet is defined as the component of the
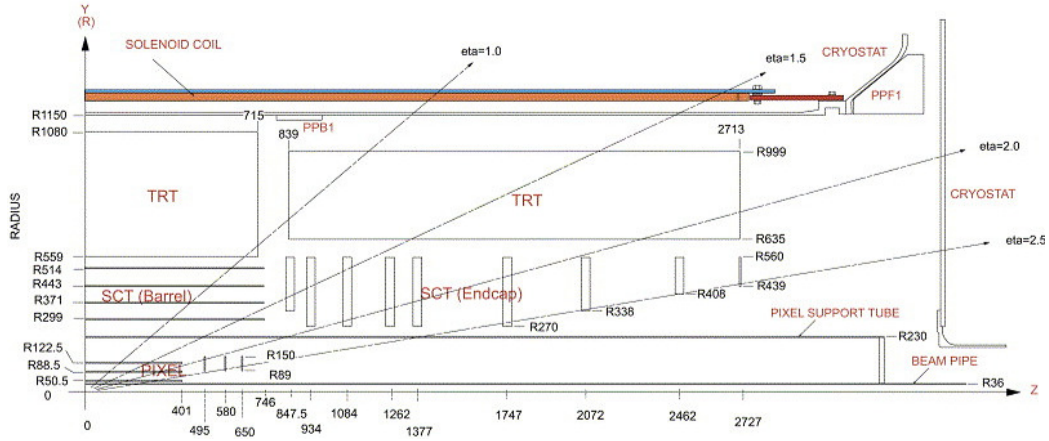
Figure 5.6: Coverage of the Inner Detector with indicated η levels. Lengths are given in mm.

momentum of the muon perpendicular to the axis given by the vectorial addition of the jet momentum axis $(\vec{p_j})$ and the muon momentum axis $(\vec{p_\mu})$. It is therefore defined by

$$\left(p_T^{rel}\right)^2 = \vec{p_\mu}^2 - \frac{(\vec{p_j} \cdot \vec{p_\mu})^2}{\vec{p_j}^2}$$

The p_T^{rel} quantity is visualized in Fig. 5.8. The p_T^{rel} distribution of muons from b-decays is harder on average than the p_T^{rel} distribution of muons from c-decays or light decays as has been mentioned in Sec. 2.5. Fig. 5.9 shows the shape differences, details on the Monte Carlo simulation can be found in Chap. 6. By fitting the p_T^{rel} distribution with template shapes for the different jet types the number of b-jets in the sample before and after tagging can be extracted. With these numbers the efficiency can be calculated as

$$\epsilon_b = \frac{N_{b,tag}}{N_b} \qquad (5.2)$$

From Fig. 5.9 it also becomes clear that the method cannot distinguish the shapes for c-jets and light jets. It is possible to fix the ratio of c-jets and light jets to reduce the fit to two dimensions but this was not desired because of the way the light jet template is derived as detailed in Chap. 6.

The method has intrinsic limitations. It cannot measure the efficiency for jets with a high transverse momentum since the axis of the muon and of the jet become more collinear the higher the jet p_T and therefore the p_T^{rel} distributions for the different types of jets become more similar. The limit for an efficiency measurement with this method is around 140 GeV which is therefore chosen as the upper limit.
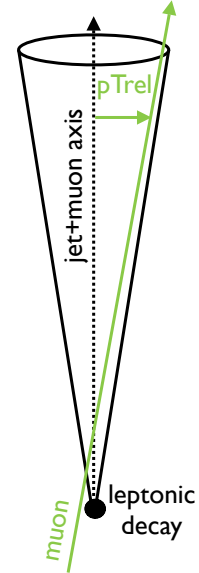
Figure 5.8: Illustration of the p_T^{rel} quantity.
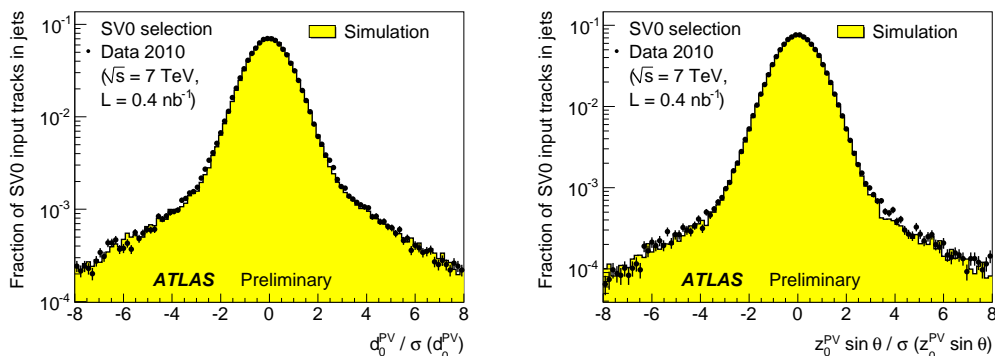
Figure 5.7: Comparison of signed impact parameter distributions on a subset of the 2010 data. S_{d_0} is shown on the left and $S_{z_0 \sin \theta}$ is shown on the right. The agreement is not perfect and the data distribution is slightly wider. The agreement is being improved by iterating the detector description and improving the detector alignment but since perfect agreement cannot be assumed this motivates a calibration of the *b*-tagging algorithms.

The application of the p_T^{rel} method on $\sim$35 pb^{-1} of recorded collision data is discussed in Chap. 6. Prior to that the p_T^{rel} method was used to measure the performance of the SV0 tagger on 3 pb^{-1} of data. The older study is detailed in [38].

System8 method

The System8 method calibrates a *b*-tagging algorithm using samples with different *b*-jet content (the n-sample and the p-sample) and another, complementary *b*-tagging algorithm. One sample is the inclusive jet sample, the other one is a sample that is enhanced in *b*-jet content by requiring an away tagged jet. This enhances the *b*-content since *b*-quarks are predominantly produced in pairs. Usually a lifetime based tagger is calibrated using the soft lepton taggers. It is possible to write down a set of 8 non-linear equations correlating the *b*-jet and *c*+light-jet content of the samples with the tagging efficiencies for those jet flavors and the total event jet counts in the samples before and after tagging as given in (5.3). It is possible to numerically solve those equations and extract the *b*-tagging efficiency as detailed in [39].

$$
\begin{aligned}
n &= n_b &+& n_{cl} \\
p &= p_b &+& p_{cl} \\
n^{LT} &= \epsilon_b^{LT} n_b &+& \epsilon_{cl}^{LT} n_{cl} \\
p^{LT} &= \alpha_6 \epsilon_b^{LT} p_b &+& \alpha_4 \epsilon_{cl}^{LT} p_{cl} \\
n^{MT} &= \epsilon_b^{MT} n_b &+& \epsilon_{cl}^{MT} n_{cl} \\
p^{MT} &= \alpha_5 \epsilon_b^{MT} p_b &+& \alpha_3 \epsilon_{cl}^{MT} p_{cl} \\
n^{LT,MT} &= \alpha_1 \epsilon_b^{LT} \epsilon_b^{MT} n_b &+& \alpha_2 \epsilon_{cl}^{LT} \epsilon_{cl}^{MT} n_{cl} \\
p^{LT,MT} &= \alpha_7 \alpha_6 \alpha_5 \epsilon_b^{LT} \epsilon_b^{MT} p_b &+& \alpha_8 \alpha_4 \alpha_3 \epsilon_{cl}^{LT} \epsilon_{cl}^{MT} p_{cl}
\end{aligned}
\tag{5.3}
$$
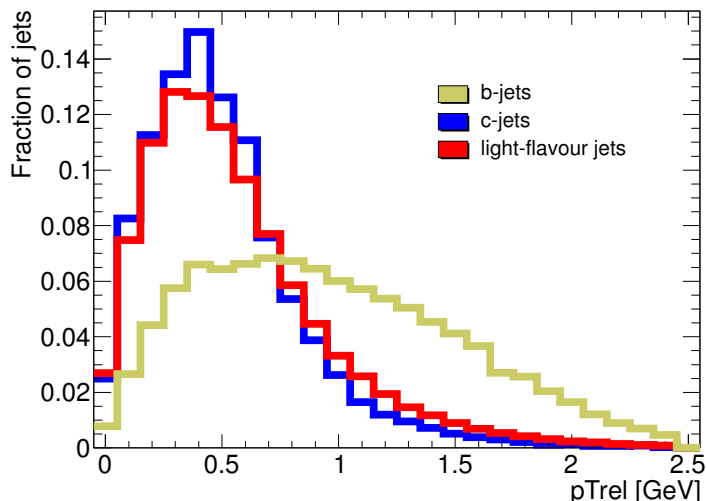
Figure 5.9: Templates used for the p_T^{rel} method for the three different jet flavors. A good discrimination of b-jets against other jets is visible. The light jet shape and the c-jet shape are similar therefore the fit cannot distinguish those jets.

$$
\begin{aligned}
\alpha_1 &= \epsilon_b^{LT,MT,n} / (\epsilon_b^{LT,n} \epsilon_b^{MT,n}) & \alpha_2 &= \epsilon_{cl}^{LT,MT,n} / (\epsilon_{cl}^{LT,n} \epsilon_{cl}^{MT,n}) \\
\alpha_3 &= \epsilon_{cl}^{MT,p} / \epsilon_{cl}^{MT,n} & \alpha_4 &= \epsilon_{cl}^{LT,p} / \epsilon_{cl}^{LT,n} \\
\alpha_5 &= \epsilon_b^{MT,p} / \epsilon_b^{MT,n} & \alpha_6 &= \epsilon_b^{LT,p} / \epsilon_b^{LT,n} \\
\alpha_7 &= \epsilon_b^{LT,MT,p} / (\epsilon_b^{LT,p} \epsilon_b^{MT,p}) & \alpha_8 &= \epsilon_{cl}^{LT,MT,p} / (\epsilon_{cl}^{LT,p} \epsilon_{cl}^{MT,p})
\end{aligned}
$$

Here n and p are the number of jets in the n-sample and in the p-sample respectively, n_b is the number of b-jets in the n-sample, n_{cl} is the number of c-jets and light jets combined in the n-sample, p_b and p_{cl} are the respective numbers in the p-sample. The high indices denote the respective numbers in the tagged samples, tagged by the lifetime tagger (LT) and the uncorrelated muon tagger (MT). The ϵs are the efficiencies of the taggers for the different jet flavors. One of the assumptions that has to be made here is that the combined tagging efficiency ϵ_{cl} is well modeled by simulation. Since ϵ_{cl} depends on the ratio of c-jets to light jets (since ϵ_c and ϵ_l are not the same) this is a potential source of bias.

This method is similar to the p_T^{rel} method since it implicitly uses the p_T^{rel} distribution to measure the efficiency (by using the soft muon tagger for the calibration). Preliminary measurements with this method show good agreement with the p_T^{rel} method.

$D^*\mu$ decays

This method utilizes the partial reconstruction of b-decay chains to identify b-jets. In particular the decay chain $b \to X\mu D^* \to X\mu D^0(\to K\pi)\pi$ is investigated. In jets with muons, D^0 candidates are built from oppositely charged tracks with kaon and pion mass hypotheses and requiring a good match with the expected D^0 mass. The resulting D^0 candidate is then combined with a track of the same charge as the used pion to form the D^* candidate using a pion mass hypothesis. A reconstructed muon is also required and the muon charge must be opposite to the D^* candidate

charge. Fig. 5.10 shows the reconstructed mass difference of the $K\pi\pi$-system to the $K\pi$-system for same sign and for opposite sign muons in the jet.
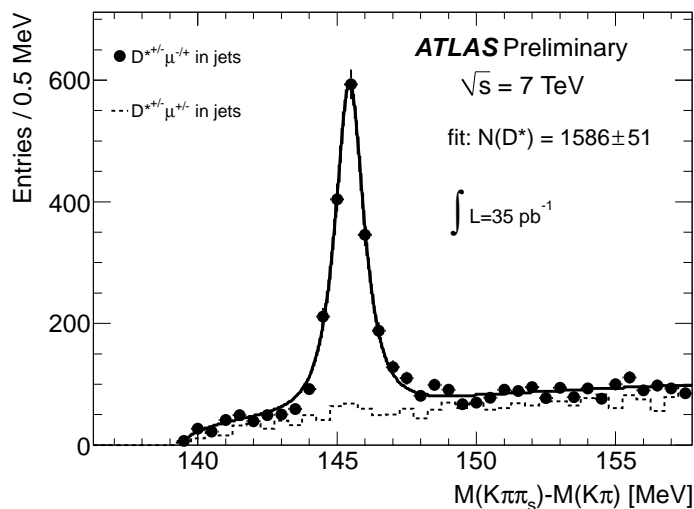
Figure 5.10: Mass difference of the reconstructed D^* and the associated D^0 candidate for opposite sign and for same sign muons. The signal peak is fitted with a modified Gaussian in combination with a power function [40].

With a background subtraction a sample that is ~93% pure in *b*-jets can be created and the efficiency can be measured by applying the tagging criterion on the sample. More details can be found in [41]. Results from this measurement are used as an independent cross-check of the p_T^{rel} method.

This method measures the efficiency for a special category of jets. It probes a track multiplicity of at least 4 (two pions, a kaon and a muon) which enhances the *b*-tagging efficiency. This has to be taken into account when using the measured efficiency in an analysis or when comparing the measurement to other methods.

Top decays

A complementary approach to measure the *b*-tagging efficiency exploits the fact that top quarks decay almost exclusively to a W boson and a *b*-quark. This implies that each event that is identified to be a top-quark pair-production event contains two *b*-quarks. Two different methods are used to extract the cross-section from those events. Both methods apply an event selection and an object selection to enhance top-quark pair-production events similar to the one detailed in Sec. 6.8. A detailed explanation of the methods can be found in [42]. Results from both top-quark pair-production based methods are compared to the results from the p_T^{rel} method in Sec. 6.7.2.

In the tag counting method the number of events after selection with X tagged jets (X=0,1,2) is counted. Due to the detector acceptance or detector resolution or effects like additional *b*-quark production through gluon radiation the number of detectable *b*-quarks in the event is not always exactly 2. With the expected number of observed events in each of the X bins and the tagging efficiencies for *c*-jets and light jets

from simulation the b-tagging efficiency can be extracted. The 0 bin is not used for this since the signal level in this bin is too low compared to the background. The efficiency is measured in the semileptonic channel and in the dileptonic channel with this method. The method allows no kinematic binning since the events contain multiple jets and the jets are not investigated individually.

In the kinematic selection method a b-tag is required on one of the jets. The jets are sorted by p_T and in the L234 sample the highest p_T jet is required to be tagged. Jets 2, 3 and 4 in order are then used to measure the efficiency. In the L1 sample the second-to-leading jet is required to be tagged and the leading jet is used for the efficiency measurement. The efficiency is calculated in two p_T bins from the combined L1+L234 sample (by counting the total number of jets and the number of tagged jets).

5.4.2 Fake rate measurements

The fake rate has been measured with two different approaches that are not discussed in detail here. One of them uses the mass reconstructed secondary vertices in a tagged sample of jets to extract the flavor fractions after tagging. It then extrapolates the b-fraction and c-fraction before fitting using the b-tagging and the c-tagging efficiencies which gives the light fraction before tagging. The light tagging efficiency can then be calculated. Details on this method can be found in [43].

The other method uses the high symmetry of light jets d_0 around the axis defined by $d_0 = 0$ and reflects the number of negative tags to the number of positive tags to get the fake rate. Details on this method can be found in [44].

5.4.3 Scale factors

The resulting calibration numbers are not given as raw efficiencies but as scale factors defined by

$$SF = \frac{\epsilon_d}{\epsilon_s} \tag{5.4}$$

where ϵ_d is the measured efficiency on data and ϵ_s is the efficiency from simulation. This is needed for subsequent analyses using the b-tagging calibration since the efficiencies depend on the jet p_T spectrum which might be different in the client analyses. With the scale factor the efficiency on simulation can be transformed to the efficiency on data if the scale factor is not strongly p_T dependent itself.

6 Application of the p_T^{rel} method

The p_T^{rel} method is used to measure the b-tagging efficiency on the dataset collected with the ATLAS Detector in 2010. Efficiencies are measured for the operating points summarized in Tab. 6.1.

name	SV0 tagger weight	b-tagging efficiency	light rejection
SV040	10.05	0.400	517
SV045	7.85	0.451	393
SV050	5.85	0.501	271

name	-log(JetProb tagger weight)	b-tagging efficiency	light rejection
JetProb40	3.95	0.407	333
JetProb50	3.25	0.507	130
JetProb60	2.65	0.604	51
JetProb70	2.05	0.707	18
JetProb80	1.40	0.804	7
JetProb90	0.6	0.901	2

Table 6.1: Operating points for the SV0 tagger and for the JetProb tagger. The tagger weight cut is implied to be read weight > cut. The values for the efficiency and for the rejection are derived from simulation.

6.1 Physics objects

This section describes the different reconstructed objects used for the p_T^{rel} analysis including the basic cuts applied on these objects.

6.1.1 Tracks

A track is used to represent the bended path of a charged particle traversing the detector. A track includes measurements of the transverse momentum, charge and spatial quantities of the charged particle trajectory. It is built from space-points (clusters of hits) in the tracking devices of the Inner Detector. Track seeds are found by combining three space-points in the silicon based subdetectors. The Pixel Detector layers and the first layer of the SCT are taken into account [34] for the seed finding. The seeds are then extended through the rest of the SCT volume and space-points that are found on the track candidate are collected for a track fit using a Kalman filter algorithm. The track candidates are then extended through the TRT to collect more detector entries and the final track is refit with the additional information. A more detailed description of tracking can be found in [45] which also contains some data to simulation comparisons of tracking input quantities to validate that tracks can be used.

The tracks used for the p_T^{rel} method are required to pass the following quality cuts: They must contain at least seven precision hits (pixel or micro-strip hits) out of which at least two have to be in the Pixel Detector and at least four in the micro-strip detector. The χ^2 per degree of freedom of the track fit cannot be larger than

3. The transverse and longitudinal impact parameters computed with respect to the primary vertex must fulfill $|d_0| < 2$ mm and $|z_0 \sin\theta| < 2$ mm, respectively. The tracks are required to have $p_T > 4$ GeV since muons with a lower p_T cannot be triggered with the ATLAS Detector[1] (and muon tracks are needed for the p_T^{rel} method). In addition, the tracks are required to have $|\eta| < 2.5$ since the Inner Detector does not cover higher values of η.

6.1.2 Muons

Muons are reconstructed with the STACO algorithm. Standalone tracks from the muon system are fit with the Muonboy algorithm [46]. It starts by searching for track segments from drift circles in the MDTs or clusters in the CSCs near activity regions defined by activity in the trigger systems. Segments that roughly point to the interaction region are added starting from the outside of the muon system and extrapolating back through the magnetic field to form a track candidate. The track candidate is then fit to form the final standalone track taking into account material budgets in the muon system and inhomogeneities in the magnetic field and it is extrapolated to the Inner Detector.

The standalone tracks in the muon system are then statistically combined with the tracks measured with the Inner Detector at the point of closest approach to the beam-pipe to form combined STACO muons. The combination is done via the covariance matrix of the single measurements [34].

Muons used for the p_T^{rel} method are required to pass the same cuts as the tracks (with the obvious additional requirement that a combined muon has to be formed by the STACO algorithm).

6.1.3 Jets

Jets represent particle showers in the calorimetry of the detector. The calorimeter systems measure the direction and energy of the particle shower and the anti-k_t algorithm is used to form jets on topological energy clusters. Different jet algorithms have been compared [47] and currently the majority of physics analyses have decided to use the anti-k_t algorithm due to its good performance. Therefore jets found with this algorithm are calibrated.

The algorithm merges the energy clusters to form jets by building a list of d_{ij} for each combination of clusters i and j defined by

$$d_{ij} = min(k_i^{-2}, k_j^{-2}) \frac{(\Delta R)^2_{ij}}{R^2}$$

and calculating

$$d_{iB} = k_i^{-2}$$

where k_i is the transverse momentum of cluster i, R is set to 0.4 and

$$(\Delta R)^2_{ij} = (\Delta \varphi_{ij})^2 + (\Delta y_{ij})^2$$

---

[1]In fact muons can be triggered with transverse momenta as low as 3 GeV but the cut is chosen 1 GeV higher since it partially avoids effects like trigger inefficiencies close to the threshold of the trigger. The trigger used in the analysis was also designed to trigger on 4 GeV muons in the beginning of 2010 data-taking but this threshold was removed later in 2010.

is the square of the radial distance with $\Delta\varphi_{ij}$ being the difference in polar angle and Δy_{ij} being the difference in rapidity between clusters i and j. The minimum of all list entries is found. If it is one of the d_{ij} the two clusters are merged by adding their four-momenta and the list is recalculated, otherwise the jet is considered to be complete and is removed from the list. The algorithm is infrared safe and collinear safe.

Jets are reconstructed at the electromagnetic scale and need to be corrected to the hadronic energy scale as described in [48]. The correction has an uncertainty between 2.5% and 14% depending on the kinematic region of the jet which is accounted for in the systematic uncertainty estimates. The jets are furthermore corrected for the missing energy deposition from the muon and the neutrino if a muon is associated to them to make them comparable to jets without muons associated. The correction is done by subtracting the average energy deposition of a muon in the flight direction of the muon from the jet and then adding contributions from the muon p_T and the assumed neutrino depending on the kinematics. A validation of this additional correction is done in [49].

The p_T^{rel} analysis is done in bins of p_T and η which means that the jet p_T and the jet η have to be inside the limits of the respective bin borders to be considered. When no bin is mentioned jets with 20 GeV $< p_T < 140$ GeV and $|\eta| < 2.5$ are considered. Jets used for the p_T^{rel} method are associated to muons and to tracks to measure the p_T^{rel} quantity. They are associated by doing a spatial matching of jets to tracks with the distance of the jet axis to the track being $\Delta R(\text{jet, track})$. As high p_T jets are more collimated, the association cut varies as a function of the jet p_T according to $\Delta R_{max} = 0.239 + \exp(-1.22 - 1.64\cdot 10^{-5}\cdot p_T^{jet})$, with the additional requirement that the cut cannot exceed 0.4. For jets with a $p_T \lesssim 37$ GeV, the cone size will be limited to 0.4, while for a jet with a p_T around 150 GeV the ΔR cut is 0.26. For muons the association cone is fixed to 0.4.

The labeling of the flavor of a jet for simulated data is done by searching for a spatial match of the jet to a true parton in the simulation. If a b-quark is found within $\Delta R < 0.3$ of the jet direction, the jet is labeled as a b-jet. If no b-quark is found the procedure is repeated searching for a c-quark. A jet for which no such association could be made is labeled as a light jet. With this labeling the truth efficiency can be calculated on simulation by counting the total number of jets that are labeled as b-jets and are tagged and dividing them by the total number of b-jets.

6.1.4 Primary vertices

A reconstructed primary vertex represents the collision point of the two protons that caused a collision event. It defines the origin of the event and for example track displacements are expressed relative to the primary vertex coordinates. It is reconstructed using an adaptive vertex algorithm described in detail in [50] and includes a beam-spot constraint. The algorithm is allowed to fit multiple primary vertices to account for pile-up (additional proton-proton collision events that contaminate the collision event under study). The effect of pile-up will become important for b-tagging when the average number of pile-up vertices increases in the future. At this point the mean number of primary vertices reconstructed is less than 2 for the data considered. A preliminary study showed that the measured efficiency when requiring exactly one primary vertex (and thereby rejecting pile-up) is compatible to the efficiency measured without this requirement. In addition a study where the 2010

data was split up in early and late periods and the p$_T^{rel}$ method was used to extract the efficiency on both did not show a significant dependency on the run period, so no dedicated treatment for pile-up is done.

6.2 Data sets, event selection and object selection

The data sample used in this analysis corresponds to approximately 35 pb^{-1} of 7 TeV collision data collected by the ATLAS experiment between March and November 2010. The analysis uses the official NTUP_BTAG physics containers version p369. The events were collected with the mu4_J5_matched trigger [51]. This trigger requires a muon reconstructed from hits in the muon system which is matched to a calorimeter jet with energy >5 GeV. The jet is not corrected to the hadronic scale in this case. In principle the ATLAS trigger menu contains these triggers with different thresholds for the jet p$_T$. They are specifically designed to provide decent data statistics for the higher p$_T$ bins of the analysis since the lower threshold triggers get heavily prescaled. The analysis was first done adding the events from these trigger streams which consequently resulted in a lower statistical error. However it turned out that the discrepancies in the data to simulation comparisons like the ones done in Sec. 6.6.10 were much larger than they are for a single trigger. Since the muon kinematics are very important for the analysis it was decided to exclude the higher threshold triggers to diminish this discrepancy.

The data is split into run periods A-I in ATLAS nomenclature. In periods A-G the trigger was not prescaled since the luminosity was low enough to collect the full rate of the trigger. Thereafter the trigger was prescaled by factors up to about 160. To assure data quality in these periods a good runs list[2] is applied which discards events where vital parts of the detector for this measurement were not taking data or were not taking data reliably. This selection requires that the Inner Detector, the muon system and the calorimeter all were fully operational. In addition only data collected during stable beam periods in which the silicon systems were operated at full depletion voltage is used.

For an event to be considered for the analysis it has to pass the event selection cuts. The primary vertex cut requires that the jet must contain a reconstructed primary vertex with at least 10 tracks associated to the primary vertex. This rejects events that are triggered by diffractive collisions or spurious interactions in the detector like beam-gas events.

A heavy flavor enhancement cut is applied that requires that the event contains a jet which is tagged with an SV0 weight[3] > 1. The jet so tagged is then excluded from further analysis to avoid a bias on the efficiency measurement. This enhances the b-fraction of the remaining jets since b-quarks are predominantly produced in pairs and events containing double b-quark production are now selected over events containing for example double light-quark production. A jet not containing a muon will, if possible, be discarded rather than one with a muon in order to retain the maximum possible number of jets with muons for the p$_T^{rel}$ measurement.

---

[2]Name of the good runs list: data10_7TeV.pro05.merged_LBSUMM_top_allchannels_7TeV.xml

[3]The operating point of the tagger was chosen to enhance heavy flavor while at the same time retaining a decent efficiency for b-jets. It is not one of the official operating points.

6.3 Simulated Samples

The simulated samples used in this measurement, listed in Tab. 6.2, are dijet samples generated with PYTHIA 6.4.21 [52] using the MRST LO* parton distribution functions [53]. To simulate the detector response, the generated events are processed through a GEANT4 [54] simulation of the ATLAS Detector, and then reconstructed and analyzed as the data. If not explicitly stated otherwise the same event and object selection cuts as described in Sec. 6.1 and 6.2 are applied. The simulated geometry corresponds to a perfectly aligned detector and the majority of the disabled pixel modules and front-end chips seen in data were masked in the simulation.

All samples simulate di-jet events and they are sliced into different p_T regions to allow decent population statistics in the higher p_T regions. The J1-J4 muon-filtered dijet samples, referred to as the JXμ dijet samples, are required to have a muon with $p_T > 3$ GeV at generator level. These samples thus contain muons from b- and c-decays, but have almost no muons from in-flight decays since pions and kaons are treated as stable particles on generator level. These samples are used to extract templates for the p_T^{rel} shape of b-jets and c-jets but they are not expected to represent the inclusive data sample. The J1-J5 dijet samples, referred to as the JX dijet samples, have no muon filter applied and are thus a more appropriate representation of the inclusive data sample.

Sample	# events, rounded	$\sigma(\text{nb}) \cdot \epsilon_{filter}$	Comment
J1 dijet	7400k	$6.78 \cdot 10^5$	$17 < p_T^{jet} < 35$ GeV
J2 dijet	2800k	$4.10 \cdot 10^4$	$35 < p_T^{jet} < 70$ GeV
J3 dijet	2800k	$2.20 \cdot 10^3$	$70 < p_T^{jet} < 140$ GeV
J4 dijet	1400k	$8.77 \cdot 10^1$	$140 < p_T^{jet} < 280$ GeV
J5 dijet	1400k	$2.34 \cdot 10^0$	$280 < p_T^{jet} < 560$ GeV
J1μ dijet	2000k	$5.28 \cdot 10^3$	$17 < p_T^{jet} < 35$ GeV, $p_T^\mu > 3$ GeV
J2μ dijet	1400k	$7.23 \cdot 10^2$	$35 < p_T^{jet} < 70$ GeV, $p_T^\mu > 3$ GeV
J3μ dijet	1000k	$3.87 \cdot 10^1$	$70 < p_T^{jet} < 140$ GeV, $p_T^\mu > 3$ GeV
J4μ dijet	1000k	$3.55 \cdot 10^0$	$140 < p_T^{jet} < 280$ GeV, $p_T^\mu > 3$ GeV

Table 6.2: Simulated samples used for the p_T^{rel} measurement.

The simulation is generally modeling the data well, but there are a few exceptions. The interaction region is wider in simulation than in data. To partly correct for this, the distribution of the primary vertex z position is re-weighted in simulation to follow that observed in data. In addition, the p_T spectrum of jets is harder in data than in simulation. Since the b-tagging efficiency depends strongly on the jet kinematics, the jet p_T spectrum in simulation is re-weighted in order to agree with that observed in data. The derived reweighting functions can be seen in Fig. 6.1. The primary vertex z position reweighting has a small effect, the p_T reweighting has a bigger impact.

To obtain an inclusive spectrum from the samples they are added with relative weights corresponding to their production cross-sections (and their filter efficiencies in the case of the JXμ samples). By doing this procedure, events from the low jet p_T slices get relatively high weights which means that statistical fluctuations are
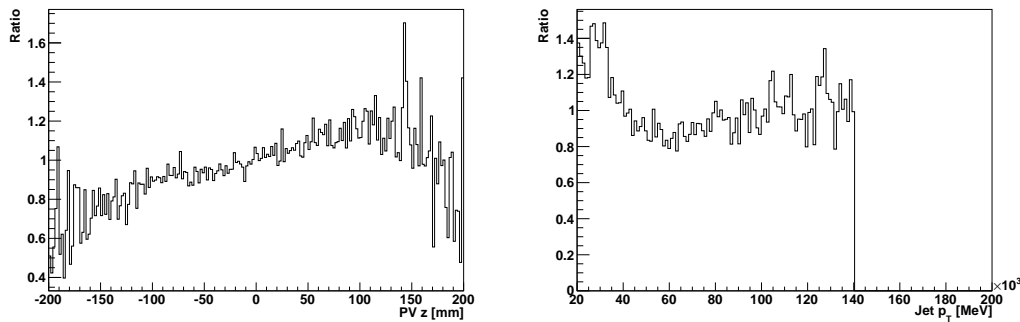
Figure 6.1: Calibration functions used to calibrate the simulated primary vertex z coordinate spectrum on the left and the simulated jet p_T spectrum on the right to data. The ratio shown is data divided by simulation.

expected to induce a high systematic uncertainty for this method. This effect can be seen for example in Fig. 6.2 for the lowest p_T bin shown.

6.4 Templates

The p_T^{rel} fit uses three templates. A b-jet template shape is derived from the JXμ samples by calculating the p_T^{rel} for all jets that pass the selections that are labeled as b-jets. Similarly a c-jet template shape is derived from the p_T^{rel} of all jets labeled as c-jets. The b-jet template from simulation is validated on data by creating a pure b-jet sample. This is done by requiring jets on data to be tagged with an IP3D+SV1 weight > 7.6 highly enhancing the b-jet content. The chosen operating point has a high rejection ($\sim$ only 1 out of 1000 light jets is tagged on simulation). Since the lifetime tagger used is uncorrelated with the p_T^{rel} distribution of the selected jets, the tagged jets can now be used to derive a p_T^{rel} template on data. The shape comparison of those tagged jets with muons can be seen in Fig. 6.2. The template shapes agree well within statistical errors.

In principle the light jet template shape could be derived from the JX samples as well but it is also possible to derive this shape directly from data. For this purpose a light-jet enhanced sample on data is created. The heavy flavor enhancement cut is dropped and instead only events that contain no jet with an IP3D+SV1 weight > -0.85 are considered. The operating point chosen has an efficiency of $\sim 80\%$ on simulation, so the expected b-jet rejection for this antitag is $\sim 96\%$ (since most of the events containing b-quarks contain two b-quarks). This leaves a sample with mostly light jets and c-jets. The remaining contamination from c-jets does not diminish the quality of the measurement since c-jets are fitted with an individual template and the ratio of c-jets to light jets is automatically adjusted by that.

In fact, the c-jet contamination is a positive effect: The light jet to c-jet ratio in the data-driven light jet shape is higher than it is in the sample that is fitted with those shapes. This is due to the fact that the light jet tagging efficiency is lower than the c-jet tagging efficiency and therefore the rejection of c-jets with this antitag is higher than the rejection of light jets which increases the light jet to c-jet ratio. This
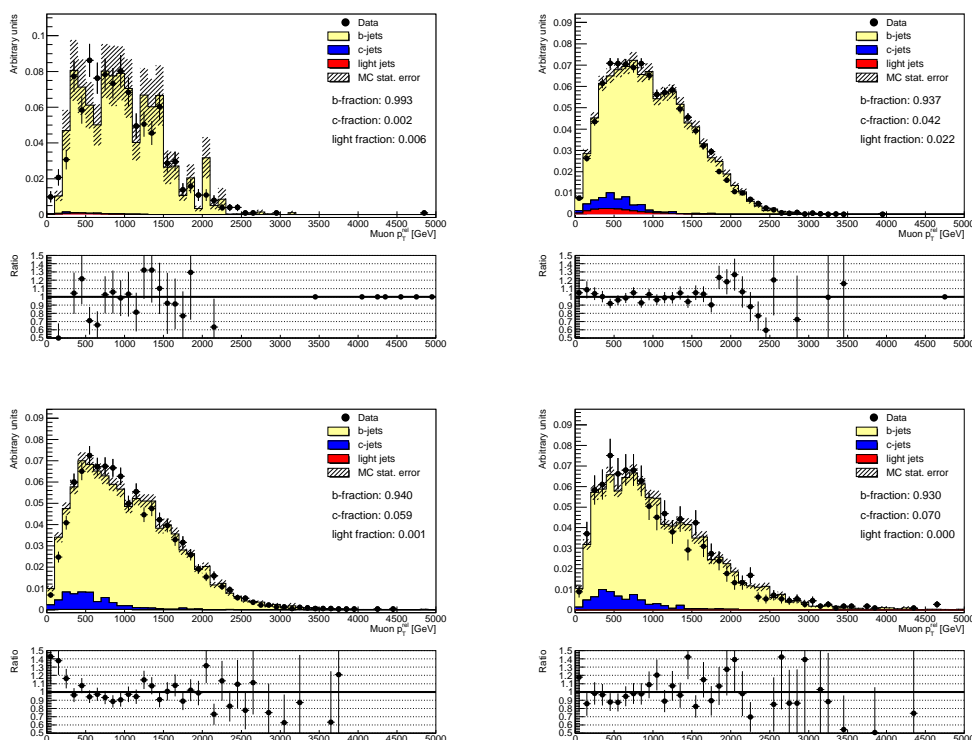
Figure 6.2: Shape validation of the p_T^{rel} shape used to fit the b-jet fractions. The simulation shapes for the different jet flavors are taken from the JXμ samples and the flavor fractions are taken from the JX samples. From top left to bottom right the 20 GeV - 30 GeV bin, the 30 GeV - 60 GeV bin, the 60 GeV - 90 GeV bin and the 90 GeV - 140 GeV bin are shown.

means that part of the c-jets in the sample that is being fit is naturally covered by the fitted contribution of the light template. So potential systematic biases due to a mismodeling of the c-jet template shape can only affect the fraction of c-jets that is not included naturally in the light template fraction.

In principle the overall light jet to c-jet ratio could be fixed to the predicted value from simulation to simplify the fit since both templates have a similar shape. This is not done for this method since it would require a detailed understanding of the c-jet rejection rate to ascertain the exact fraction of c-jets in the data-driven light template. It would also introduce dependencies on the predicted ratio.

The template still contains a small amount of b-jets as shown in Tab. 6.3 but the measured efficiency is corrected for this contribution and a systematic uncertainty is assigned as explained in Sec. 6.6.9.

To exclude possible biases from applying the antitag a comparison of the template shape derived from simulation with this prescription is compared with the true shape of light jets from simulation in Fig. 6.3. The agreement is reasonable, the residual discrepancy stems from the expected c-jet and b-jet contamination of the light template which is higher in the low p_T bins as can be seen in Tab. 6.3. Deriving a template shape from data eliminates different possible biases like a mismodeling of fake muons in light jets or a mismodeling of decays in flight or a mismodeling of the

ratio of those two contributions and is therefore beneficial for the analysis. Furthermore the statistical error on this data-driven template is smaller than the statistical error on the simulation based one.
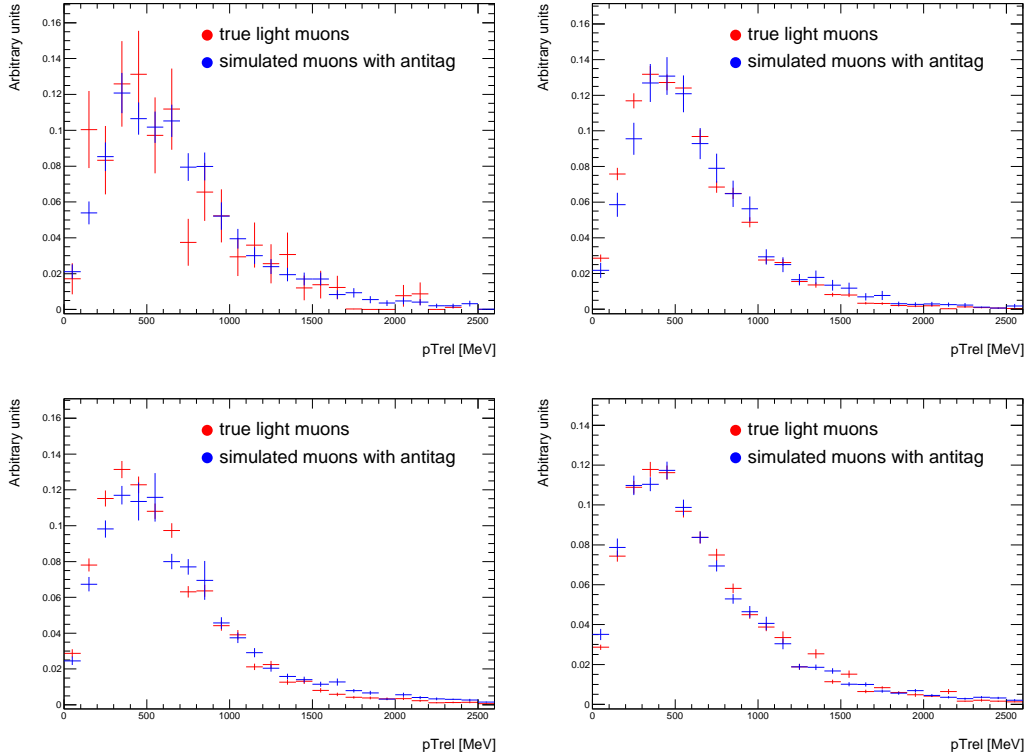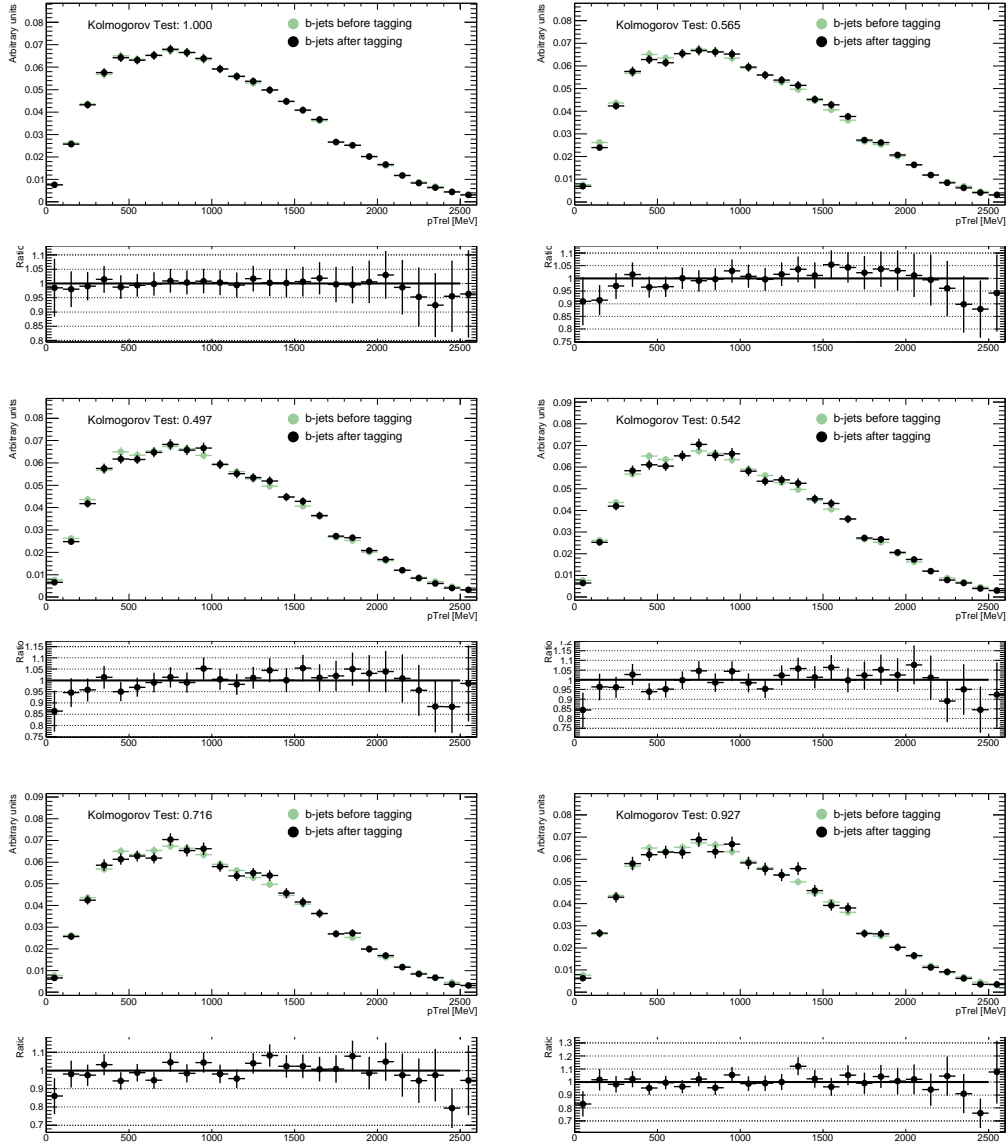

Figure 6.3: Shape comparison of the jets with the antitag requirement to jets that are true light jets on the JX samples. For the two high p$_T$ bins the J1 and J2 samples have been omitted to decrease statistical fluctuations due to reweighting. No backtag requirement was applied to increase statistics. From top left to bottom right the 20 GeV - 30 GeV, the 30 GeV - 60 GeV the 60 GeV - 90 GeV and the 90 GeV - 140 GeV bins are shown. The agreement is not perfect which is expected due to residual contamination of c-jets and b-jets.

For fitting the tagged sample the pretag templates are used as well. This is done since the b-jet and the c-jet template statistics are lower when derived from simulation after tagging and also because the light jet template can be derived on the pretag sample only by definition. To exclude possible biases from that template choice, tagged templates are derived for each operating point for b-jets and c-jets and the template shapes are compared with the template shapes derived from the pretag sample. Figs. 6.4 - 6.7 illustrate the good agreement within statistical errors of the two sets of templates.

6.5 Fit method

The templates are fit to data using a binned likelihood fit implemented using the ROOT TMinuit minimization package. The p$_T^{rel}$ quantity is binned in bins of 0.1 GeV

Figure 6.4: Shape comparison of the pretag sample and the tagged sample b-jet shapes. From top left to bottom right the JetProb90, JetProb80, JetProb70, JetProb60, JetProb50 and the JetProb40 operating points are shown.

size which is a good compromise between granularity and statistical relevance of the single bins. The negative log likelihood function for a given set of templates to model the data distribution is given by

$$\ln \mathscr{L} = - \sum_{i=1}^{n} d_i \ln f_i - f_i$$
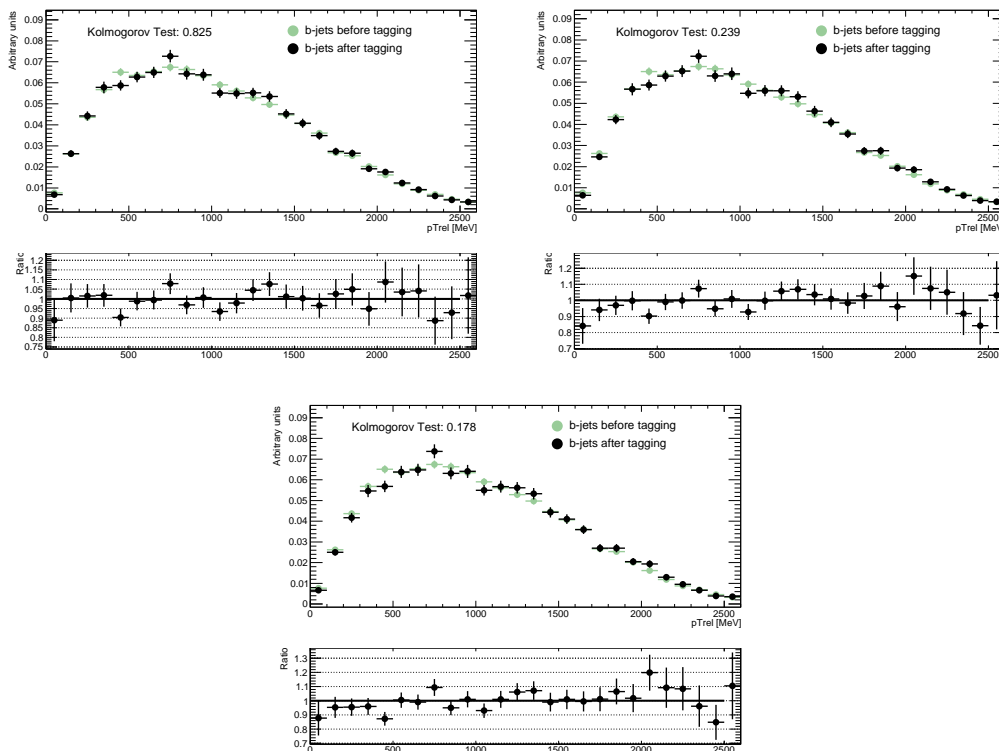
Figure 6.5: Shape comparison of the pretag sample and the tagged sample b-jet shapes. Shown are SV050 on the top left, SV045 on the top right and SV040 on the bottom.

$\mathscr{L}$ is the likelihood function, n is the number of bins in $\mathrm{p_T^{rel}}$, d_i is the number of jets in bin i and f_i is the predicted number of jets in this bin defined as

$$f_i = N_D \sum_{j=1}^{3} n_{ji}$$

where N_D is the total number of data events and n_{ji} is the fraction of simulated events from template j in bin i [55].

This likelihood does not contain a treatment of the finite Monte Carlo statistics of the simulation, instead the finite statistics are treated as a systematic uncertainty. Minimizing this negative log likelihood function using the TMinuit package results in the best fit for the different contributions of the templates. The quoted statistical errors are the range that corresponds to an increase of 0.5 in the likelihood function. The ROOT MINOS error treatment package is used to allow for non-symmetric errors but for the combined error the direction of highest deviation from the central value is used.

The stability of the fit is validated on simulation. The fit is performed on the JX sample with templates derived from the JX sample for all three jet flavors and using tagged samples for the tagged fit. The light jet template shape is also taken from true muons in light jets on simulation. This implies that the fit must reproduce the input from simulation if the fit is unbiased. To also validate the error treatment of the fit 10000 pseudo-experiments are conducted where the pseudo-data from simulation is
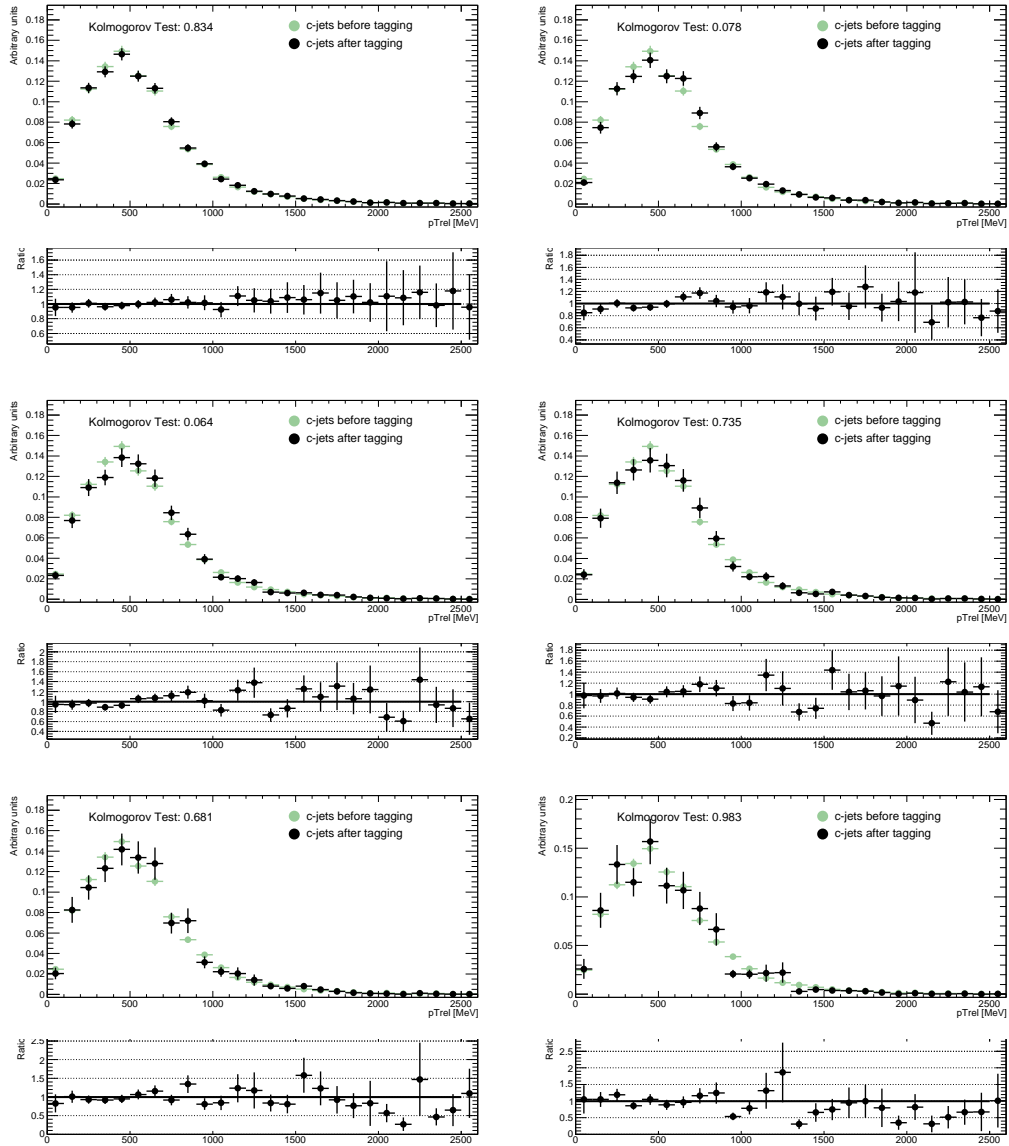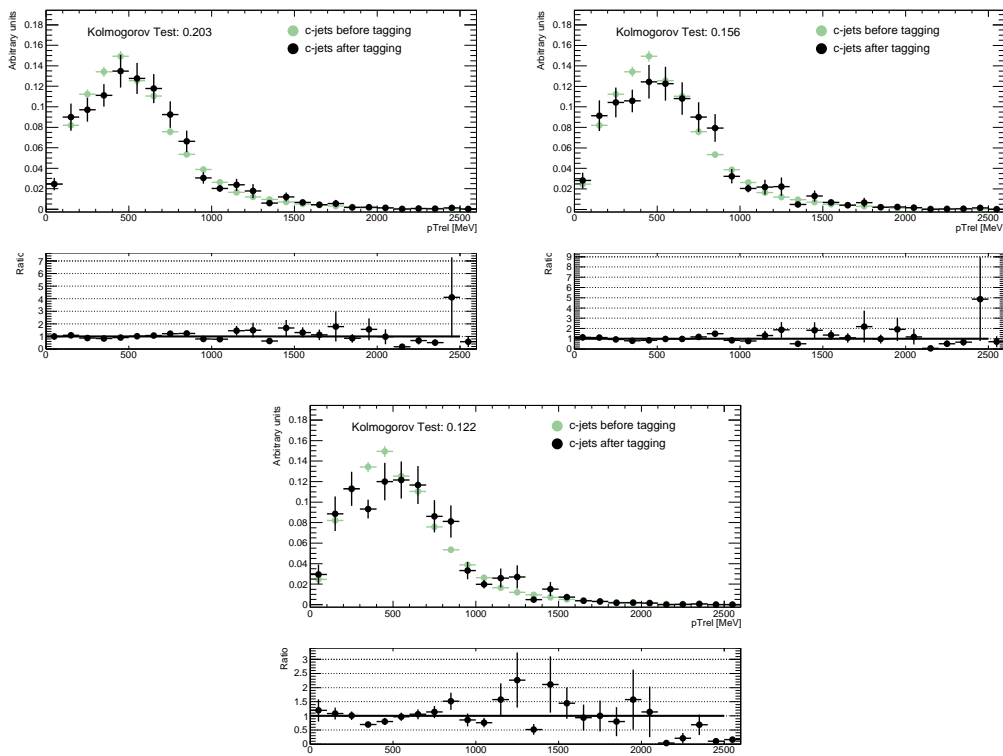
Figure 6.6: Shape comparison of the pretag sample and the tagged sample c-jet shapes. From top left to bottom right the JetProb90, JetProb80, JetProb70, JetProb60, JetProb50 and the JetProb40 operating points are shown.

created by varying each bin of the p_T^{rel} distribution by a Poisson function with the original bin content as parameter.

A pull distribution is created from that where the pull is defined as

$$\text{Pull} = \frac{\epsilon_{true} - \epsilon_{meas}}{\sigma}$$

where ϵ_{meas} is the efficiency from the fit, ϵ_{true} is the true efficiency derived from simulation and σ is the statistical error returned by the fit. Fig. 6.8 shows this distribution and proves that the fit is unbiased and the error treatment is correct.

Figure 6.7: Shape comparison of the pretag sample and the tagged sample c-jet shapes. Shown are SV050 on the top left, SV045 on the top right and SV040 on the bottom.

6.6 Systematic uncertainties

The systematic uncertainties affecting the p_T^{rel} method are those that either change the shapes of the p_T^{rel} templates used to fit the sample composition or those which change the efficiency in simulation used as the denominator in the efficiency scale factor calculation (see Eq. 5.2). Systematics can either have a direct impact on the p_T^{rel} itself, which is the case for the jet direction resolution, or they can indirectly affect the p_T^{rel} distribution by changing the sample composition or the kinematics of the sample. An example of such a systematic is the jet energy scale uncertainty.

If not stated otherwise in the description of a systematic uncertainty it is estimated by repeating the p_T^{rel} fits on data with modified templates. For example the uncertainty from the jet energy scale is estimated by deriving new b- and c-templates from simulated events where the jet energy scale has been increased or decreased by one standard deviation. The difference between the default efficiency scale factor and that derived with the altered templates is taken as the systematic uncertainty due to the jet energy scale uncertainty.

In the following a list of all systematic uncertainties considered for the measurement is presented, the p_T^{rel} measurement with the templates described before is referred to as the central value or the central fit. The systematic uncertainties are summarized in Tabs. C.1 - C.9 in App. C.
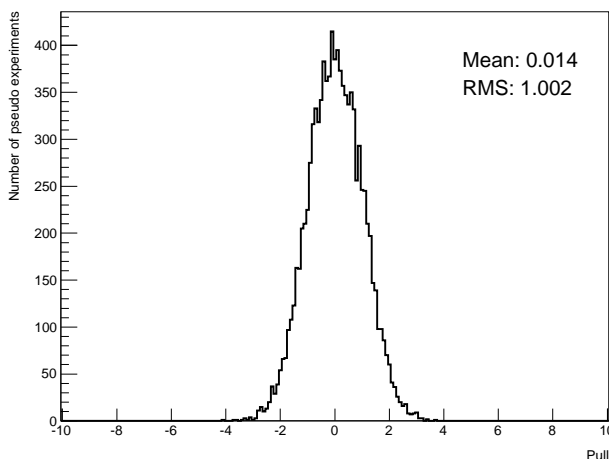
Figure 6.8: Pull distribution for 10000 pseudo-experiments. The mean is ∼0 which shows that the fit method is unbiased. The width is 1 which shows that the statistical error estimate is correct.

6.6.1 Jet direction resolution

The jet direction is one of the variables directly entering the p_T^{rel} calculation. A poor jet direction resolution makes the p_T^{rel} distributions for b-, c- and light-quark jets look more alike. Any difference in the jet direction resolution between data and simulation would therefore result in a bias of the method.

To investigate if any such bias is present, an independent jet axis was formed by vectorially adding the p_T of all tracks associated to the jet. The difference between the jet based and the track based axis in both azimuthal ($\Delta\varphi(\text{calo}, \text{track})$), and polar ($(\Delta\eta(\text{calo}, \text{track}))$ directions was derived in both data and simulation. It was found that data and simulation are consistent with each other but a discrepancy on the order of 10 mrad could not be ruled out. The p_T^{rel} fit was therefore repeated after smearing the individual jet axis with a Gaussian function with a width of 10 mrad. It is however conservative to assume that the jet direction resolution is the only cause of this mismatch between data and simulation. An equally likely scenario is that the jet direction between data and simulation agree and that the discrepancies observed in the $\Delta R(\text{calo}, \text{track})$ distribution are due to a poor modeling of the tracks in jets in the simulation. Therefore for each tagger calibrated the efficiency scale factor is corrected for half of the difference between the unsmeared case and the 10 mrad smeared case. A 100% relative systematic uncertainty is assigned to this correction covering the full possible range of perfect calorimeter jet axis resolution to perfect track jet axis resolution.

6.6.2 Muon momentum resolution

As the muon momentum enters the p_T^{rel} calculation, any difference between the muon momentum scale in data and simulation would lead to a bias in the efficiency scale factor. ATLAS has reconstructed the J/ψ from muon track daughters which is

summarized in [56]. The reconstructed mass is found to be 3.095±0.001 GeV, to be compared with the PDG mass of 3.096916±0.000011 GeV. The good agreement with the prediction shows that simulation models the muon p$_T$ spectrum well and momentum resolution effects higher than a few per mill are excluded. Therefore the systematic uncertainty on this measurement is negligible and no further treatment is required.

6.6.3 Jet energy scale

A jet energy scale in simulation which is different from that in data would bias the p$_T$ spectrum of the simulated events used to build the p$_T^{\text{rel}}$ templates. It would also cause migration between different jet p$_T$ bins used in the analysis. The migration effect is dominating since the change in b-tagging efficiency is large if the jet p$_T$ of a low p$_T$ jet is changed by a small amount whereas the change in the p$_T^{\text{rel}}$ shapes is low.

The systematic uncertainty originating from the jet energy scale is obtained by scaling the p$_T$ of each jet in the simulation up or down by one standard deviation according to the uncertainty of the jet energy scale for each individual jet and re-deriving the b- and c-templates. This results in two new sets of b- and c-templates which are used to evaluate the b-tagging efficiency and give the systematic uncertainty on the central fit. The jet p$_T$ re-weighting function is not re-derived for the scaled samples. This leads to a slight overestimation of the systematic uncertainty since a new re-weighting of jet p$_T$ would mitigate part of the effect of the jet energy change on simulation but since this is not a leading uncertainty no further studies were conducted to get a more precise estimate.

6.6.4 Modeling of b-production

In dijet data, b-jets can be produced via several mechanisms: flavor creation, flavor excitation and gluon splitting as has been explained in Sec. 2.5. In the latter case the angle between the two b-quarks can be so small that both of them end up within the same jet cone. Such a b-jet, containing two b-quarks, has a larger probability of being b-tagged than those containing just one b-quark. A study aimed at selecting b-jets from gluon splitting containing two b-quarks [57] finds that the b-tagging efficiency for a jet with two b-quarks is larger than for jets with a single b-quark by 10% - 25%, depending on jet p$_T$. If the ratio of double-b to single-b jets is different in data and simulation due to a wrong input fraction of the production processes a bias is therefore introduced in the b-tagging efficiency measurement.

The systematic uncertainty associated with the b-production was estimated by varying the ratio of double-b jets to single-b jets by 100% in simulation and redoing the p$_T^{\text{rel}}$ fit with the so changed template. The difference to the central fit was taken as a systematic uncertainty. The modified templates were built by assigning a weight of either two or zero to events which contain two b-quarks with a relative opening angle of $\Delta R < 0.8$ on simulation.

6.6.5 Fragmentation

An incorrect modeling of the fragmentation in simulation can affect the momentum spectrum of the muons from the b-decays and thus the p$_T^{\text{rel}}$ distribution. To

investigate the impact of fragmentation on the efficiency scale factor, the p_T^{rel} templates were re-derived on a simulated sample where the X_b, i.e. the fraction of the b-quark energy carried onto the b-hadron, was changed by 5%. The p_T^{rel} fits were then re-done on data using these altered p_T^{rel} templates, and the difference in the b-tagging efficiency between this and the default scenarios was taken as a systematic uncertainty.

6.6.6 Fake muons in b-jets

The p_T^{rel} templates for b-quark jets are obtained from the simulated JXμ dijet samples where a muon with $p_T > 3$ GeV is required at generator level. This filter will suppress b-jets containing a fake muon. The fraction of fake muons in the p_T^{rel} templates built from these samples is therefore likely to be lower than in data. As can be seen in Fig. 6.9, fake muons have a p_T^{rel} spectrum different from muons from b-decays. Thus a mismodeling of the contribution from fake muons in b-jets will influence the b-tagging efficiency measurement.
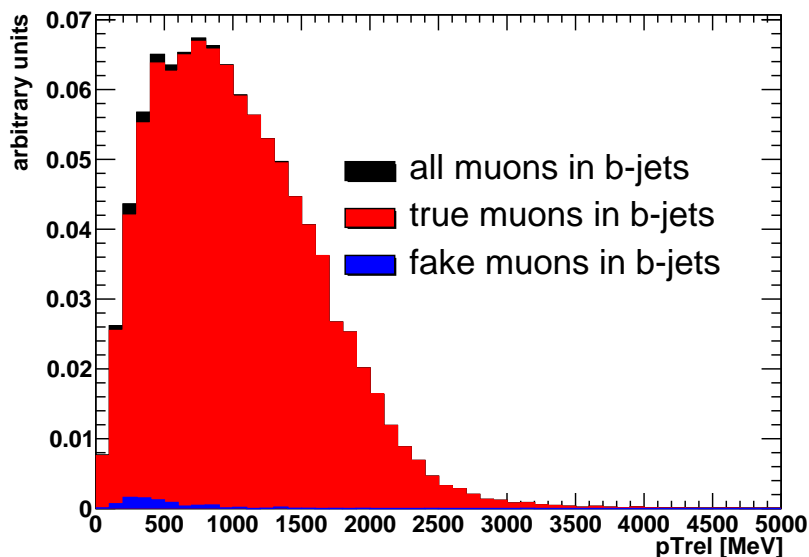
Figure 6.9: The p_T^{rel} distribution of truth-matched (red) and fake (blue) muons in b-jets. The p_T^{rel} spectrum of the fake muons is softer than that of truth-matched muons and the fraction is 0.8%.

To investigate the impact of fake muons on the b-tagging efficiency measurement p_T^{rel} fits were performed using b-templates with different fake muon fractions. Fake muons were defined as those not matched to a truth track from a muon. To get a conservative estimate no requirement on the matching probability was made so that each track that is loosely associated to a non-muon track counts as a fake muon. With this definition, 0.8% of the muons were categorized as fake muons. The fraction of fake muons in b-jets was then increased by a factor of three to create a new p_T^{rel} templates for b-jets. The p_T^{rel} fit was repeated to obtain the difference in measured b-tagging efficiency.

6.6.7 p_T^{rel} template statistics

The templates derived from simulation have a non-negligible statistical error. This statistical error is not included in the likelihood function so it has to be treated as a separate systematic uncertainty. To ascertain this systematic uncertainty pseudo-experiments are conducted on simulation where the template shapes are varied independently bin-by-bin with a Gaussian function that takes into account the statistical error due to the cross-section reweighting 1000 times. The modified templates are then used to fit the data and the standard deviation of the resulting efficiency distribution is taken as a systematic error.

The choice of templates is different from the default templates to measure this systematic uncertainty. The light template is taken from true muons in light jets from simulation without requiring a tagged jet to increase the light content. For the fit on the tagged sample the templates are still taken from simulation without tag, but the variation of those templates is done with respect to the variation of the templates before tagging because the template after tagging is a subset of the template before tagging. Therefore the same random number is used for the Poisson fluctuation on the tagged template and on the pretagged template. In addition the error on the templates used for the tagged sample is assumed to be the error from the tagged templates (the templates derived from simulation with a tagging requirement). With this choice of templates for the fit the template statistics systematic also contains part of the systematic error that might arise from modeling the light template with the data-driven template since statistics for the comparison in Fig. 6.3 are limited. The variation of the simulated light template within its statistical error covers this effect.

Furthermore the usage of untagged templates to fit the tagged sample is validated in a similar way. Figs. 6.4 - 6.7 show that the templates before and after applying the tagging requirement agree well within statistical errors. When evaluating this systematic the statistical errors of the tagged templates are used for the fit on the tagged sample so that possible biases are covered.

6.6.8 Scale factor for inclusive b-jets

The p_T^{rel} method can only measure the b-tagging efficiency scale factor in data for semileptonically decaying b-jets. The scale factor is the same for inclusive b-jets if the modeling of the difference in b-tagging efficiencies between the two classes of jets is perfect. To assess the quality of the modeling of this difference the number of tracks associated to jets and displaced by $d_0 > 2.3\,mm$ is used. The efficiency for semileptonically decaying b-jets and inclusive b-jets is similar when fixing the number of displaced tracks and the difference between the two categories arises through different respective distributions of displaced tracks in jets. This mismodeling can be absorbed by an additional scale factor given by the following calculation.

The p_T^{rel} measurement measures the tagging efficiency for b-jets containing muons in data and yields a scale factor to use on simulation given by

$$SF_{MC \to Data}^{\mu} = \frac{\epsilon_{Data}^{\mu}}{\epsilon_{MC}^{\mu}}$$

which is only valid for jets with muons as discussed above. Here ϵ_{Data}^{μ} is the b-tagging efficiency measured on data with the p_T^{rel} method and ϵ_{MC}^{μ} is the efficiency derived

from simulation for jets containing muons (corresponding to the p_T^{rel} object and event selection). The users who apply the scale factor measurement to their analyses are interested in the efficiency for inclusive b-jets in a given sample since they will likely not have a specific selection on jets containing muons. This inclusive scale factor can be written as

$$\epsilon_{Data}^{incl} = \epsilon_{MC}^{\mu} \cdot SF_{MC\to Data}^{\mu} \cdot SF_{Data}^{\mu\to incl}$$

$$= \epsilon_{MC}^{incl} \cdot SF_{MC\to Data}^{\mu} \cdot \frac{SF_{Data}^{\mu\to incl}}{SF_{MC}^{\mu\to incl}} \tag{6.1}$$

where $SF_{Data}^{\mu\to incl}$ is the scale factor for going from jets with muons to inclusive jets on data and $SF_{MC}^{\mu\to incl}$ is the respective scale factor on MC. ϵ_{MC}^{incl} is the efficiency for all jets derived from simulation.

The user applies the scale factor provided to ϵ_{MC}^{incl} by default so the fraction in Eq. (6.1) can be treated as an additional multiplicative term to the scale factor.

The denominator is derived from MC, the enumerator can be written as

$$SF_{Data}^{\mu\to incl} = \frac{\sum\limits_{bin} N_{bin}^{incl} \cdot \epsilon_{bin}^{incl} \Big/ \sum\limits_{bin} N_{bin}^{incl}}{\sum\limits_{bin} N_{bin}^{\mu} \cdot \epsilon_{bin}^{\mu} \Big/ \sum\limits_{bin} N_{bin}^{\mu}}$$

$$= \frac{\sum\limits_{bin} R_{bin}^{incl} \cdot \epsilon_{bin}^{incl}}{\sum\limits_{bin} R_{bin}^{\mu} \cdot \epsilon_{bin}^{\mu}} \tag{6.2}$$

$$= \frac{\sum\limits_{bin} R_{bin}^{incl} \cdot \epsilon_{bin,MC}^{\mu}}{\sum\limits_{bin} R_{bin}^{\mu} \cdot \epsilon_{bin,MC}^{\mu}} \tag{6.3}$$

where N_{bin}^{incl} is the number of jets in a bin of an arbitrary binning, N_{bin}^{μ} is the respective number of jets with associated muons. R_{bin} is the ratio of all jets in that bin ($R_{bin} = \frac{N_{bin}}{\sum\limits_{bin} N_{bin}}$) with higher index from the respective N_{bin} used. The binning is arbitrary in principle, here a binning in number of displaced tracks is used as explained above. Going from Eq. (6.2) to Eq. (6.3) the assumption is made that the efficiency in a given bin is the same for jets with muons and inclusive jets (the prerequisite for doing this method) and that the scale factor $SF_{MC\to Data}^{\mu}$ is close to unity which turns out to be true in Sec. 6.7.

The resulting additional scale factor is calculated with equation Eq. (6.3). For the calculation the displaced track multiplicities are taken from jets labeled as b-jets for simulation and from jets tagged with the SV050 tagger for data. The inclusive sample used is not the true inclusive sample but the sample where jets with muons are subtracted. Allowing a muon contribution in the sample would lower the systematic uncertainty but this is not done since the inclusive input data is not available for the analysis in a feasible way so the conservative estimate is used. Since the systematic

uncertainty is known to be overestimated it is not taken as a correction to the measured value but is fully assigned as a systematic uncertainty.

6.6.9 Modeling of the light template

As indicated in Sec. 6.4 the sample used to derive the light template is not a pure light jet sample since the tagger requirement does not reject all contamination from b-jets and c-jets. Fig. 6.3 shows that this template from unfiltered simulation and the true light template of the same samples have a residual disagreement due to contamination from heavier jets.

The influence of the non-light-content is studied with the JX samples. The flavor fractions of the light templates derived with the JX samples are shown in Tab. 6.3. The b-jet contamination will influence the fitted number of b-jets in the p$_\text{T}^\text{rel}$ dis-

	$p_\perp$ [GeV]			
Template	$20 - 30$	$30 - 60$	$60 - 90$	$90 - 140$
light	63.1	65.8	74.1	80.4
c	31.2	29.5	22.8	17.5
b	5.7	4.7	3.1	2.1

Table 6.3: The true fractions of b, c and light quarks in the antitagged template in bins of p$_\text{T}$ in percent.

tribution and therefore directly influence the fit result. To evaluate the effect of a potential mismodeling of the b-fraction in the light template the fraction is varied up and down by 100% and the p$_\text{T}^\text{rel}$ fit result with the created templates is compared to the normal fit on simulation. The central fit result is also corrected for the additional b-jet fraction that is contained in the light template. The c-jet content is beneficial for the analysis as discussed before so no variation of the c-jet content is done.
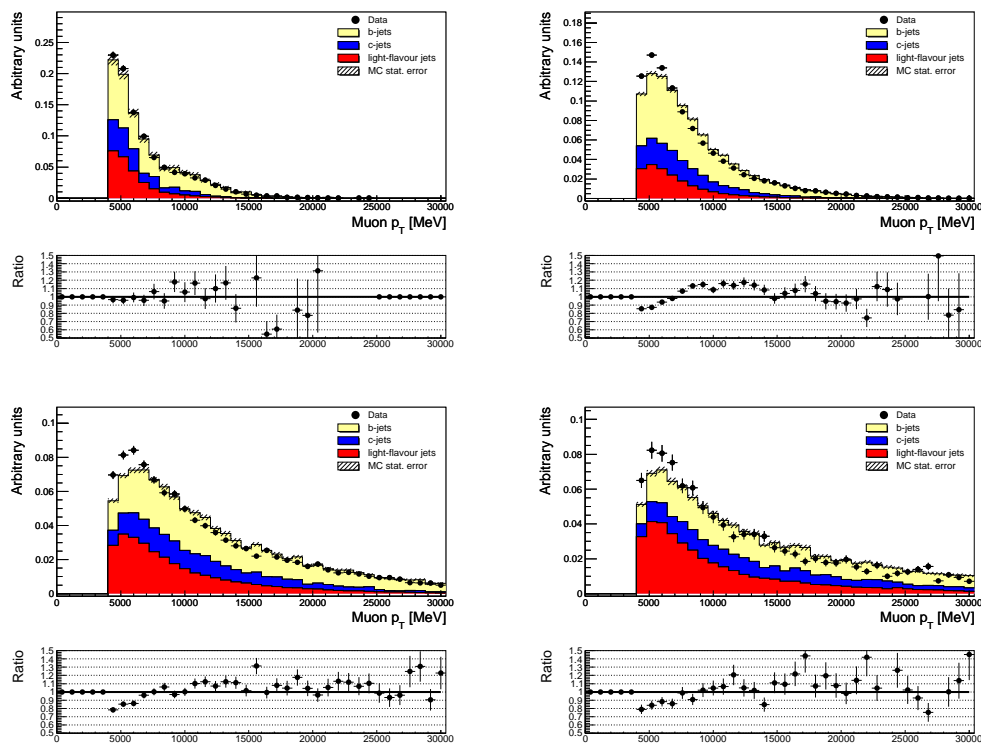
6.6.10 Muon p$_\text{T}$ spectrum

The muon p$_\text{T}$ spectrum is not perfectly modeled by simulation as can be seen in Fig. 6.10. To estimate the effect of this mismodeling on the p$_\text{T}^\text{rel}$ measurement the measurement is repeated after explicitly reweighting the muon p$_\text{T}$ spectrum on simulation to match the one in data. The difference to the central fit is assigned as a systematic uncertainty.

The muon p$_\text{T}$ discrepancies are also the reason for the choice of trigger as stated before. When combining triggers with different jet momentum thresholds the discrepancy in the muon p$_\text{T}$ spectrum is even bigger. This can be seen in Fig. 6.11 and is the reason for choosing only the low p$_\text{T}$ threshold trigger to maintain a low systematic uncertainty from this.

6.7 Results

Tab. 6.4 summarizes the measured scale factors for the different tagger operating points in bins of jet p$_\text{T}$. Most measured scale factors are lower than 1 which means that the simulated efficiency is too high and has to be corrected. A trend to lower scale factors is visible when increasing the JetProb tagger cut from high efficiency to low efficiency. The fit results for the untagged and the tagged samples are shown
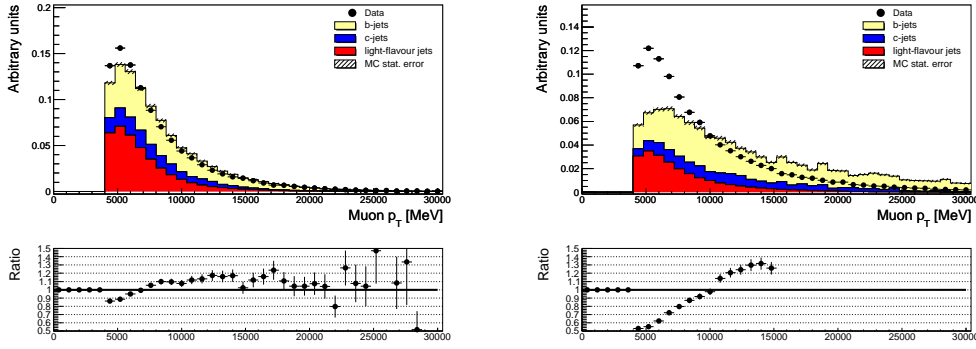
Figure 6.10: Data to simulation comparison of the muon p_T spectrum. A discrepancy is visible which gets larger when going from lower p_T to higher p_T. The p_T shapes are taken from the JXμ samples for the b-jets and the c-jets and from the data-driven template for the light jets. The fractions of the different jet flavors are taken from the JX samples. To estimate the impact of this discrepancy the p_T spectrum in simulation is reweighted to fit the p_T spectrum in data and the resulting difference in the p_T^{rel} fit is taken as a systematic error. From top left to bottom right the 20 GeV - 30 GeV bin, the 30 GeV - 60 GeV bin, the 60 GeV - 90 GeV bin and the 90 GeV - 140 GeV bin are shown.

in App. A in Figs. A.9 - A.17 for all p_T bins to give a visual impression of the fit quality. The scale factors are shown in bins of p_T in Figs. A.1 and A.2 and in bins of $|\eta|$ in Figs. A.3 and A.4. The graphical representation shows that the scale factor is compatible with being flat in p_T and $|\eta|$. The data to simulation comparison of the b-tagging efficiency is also appended in Figs. A.5 - A.8.

The available simulation statistics are a leading systematic uncertainty. By increasing the amount of simulated events it will be possible to decrease this source of error for future measurements. The reweighting of the muon p_T spectrum also contributes a significant part of the total systematic uncertainty. Detailed studies of the triggers used are underway to get an understanding of the source of the discrepancy in the p_T spectra on data and on simulation. If the agreement can be improved this source of systematic error will no longer have to be considered.

It is planned to redo the calibration for each new period of datataking if the run conditions change significantly since in this case the b-tagging efficiency might change. The ATLAS experiment is still in an early phase of running so the conditions change

Figure 6.11: Data to simulation comparison of the muon p_T spectrum for a combination of muon to jet matched triggers with jet thresholds of 5,10,15,30 and 55 GeV. It is evident that the agreement is worse than in Fig. 6.10 The p_T shapes are taken from the JXμ samples for the b-jets and the c-jets and from the data-driven template for the light jets. The fractions of the different jet flavors are taken from the JX samples. On the left the 30 GeV - 60 GeV bin is shown and on the right the 60 GeV - 90 GeV bin is shown.

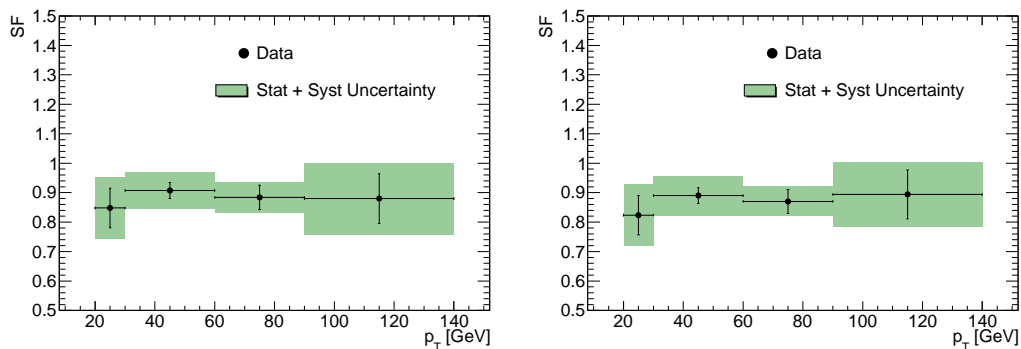| Operating point	p_T bin [GeV]			
	20-30	30-60	60-90	90-140
SV050	$0.85 \pm 7.5\% \pm 9.1\%$	$0.91 \pm 2.9\% \pm 6.0\%$	$0.88 \pm 4.6\% \pm 3.6\%$	$0.88 \pm 9.8\% \pm 10.1\%$
SV045	$0.80 \pm 7.9\% \pm 9.3\%$	$0.92 \pm 3.1\% \pm 7.5\%$	$0.89 \pm 4.7\% \pm 5.6\%$	$0.87 \pm 10.0\% \pm 9.4\%$
SV040	$0.77 \pm 8.4\% \pm 9.9\%$	$0.92 \pm 2.6\% \pm 9.3\%$	$0.90 \pm 4.8\% \pm 7.2\%$	$0.86 \pm 10.4\% \pm 10.7\%$
JetProb90	$0.99 \pm 6.0\% \pm 2.0\%$	$1.00 \pm 2.9\% \pm 1.7\%$	$0.97 \pm 4.5\% \pm 2.1\%$	$0.99 \pm 8.7\% \pm 0.9\%$
JetProb80	$0.97 \pm 6.3\% \pm 4.3\%$	$0.99 \pm 2.7\% \pm 4.1\%$	$0.94 \pm 4.1\% \pm 3.2\%$	$1.00 \pm 8.5\% \pm 3.4\%$
JetProb70	$0.93 \pm 6.7\% \pm 5.6\%$	$0.97 \pm 2.6\% \pm 5.3\%$	$0.94 \pm 4.2\% \pm 2.9\%$	$0.94 \pm 8.7\% \pm 4.8\%$
JetProb60	$0.90 \pm 6.7\% \pm 8.9\%$	$0.93 \pm 2.7\% \pm 5.9\%$	$0.91 \pm 4.3\% \pm 3.2\%$	$0.87 \pm 9.2\% \pm 6.1\%$
JetProb50	$0.82 \pm 7.7\% \pm 9.2\%$	$0.89 \pm 2.9\% \pm 6.7\%$	$0.87 \pm 4.6\% \pm 3.5\%$	$0.89 \pm 9.5\% \pm 8.2\%$
JetProb40	$0.86 \pm 9.3\% \pm 10.1\%$	$0.84 \pm 3.2\% \pm 7.2\%$	$0.82 \pm 4.9\% \pm 4.0\%$	$0.85 \pm 10.2\% \pm 9.9\%$

Table 6.4: Measured scale factors for the different operating points. The first uncertainty quoted is the statistical error, the second uncertainty quoted is the systematic error.

frequently. This means that the statistical error is not expected to decrease significantly since the trigger streams used in the analysis are prescaled to give an approximately constant rate independent of the luminosity.

6.7.1 p_T and $|\eta|$ dependence

The p_T dependence of the scale factor is shown in Fig. 6.12 for the 50% operating points of the SV0 tagger and the JetProb tagger as an example. The chosen binning due to the amount of available data and simulation statistics is 20 GeV $< p_T <$ 30 GeV, 30 GeV $< p_T <$ 60 GeV, 60 GeV $< p_T <$ 90 GeV, and 90 GeV $< p_T <$ 140 GeV. There is no trend visible in the scale factor distribution. No additional assumption is made about a flat general scale factor but the results are provided to all physics analyses in this form.

The η dependence of the scale factor is shown in Fig. 6.13 for the 50% operating points of the SV0 tagger and the JetProb tagger. There is no strong dependence on

Figure 6.12: p_T dependence of the scale factor for the 50% operating point, left for the SV0 tagger, right for the JetProb tagger. The first bin has a high statistical error since the bin population is small due to the semileptonic correction of the jet energy.

η in this binning so it suffices to use the p_T dependent scale factor for subsequent analyses.
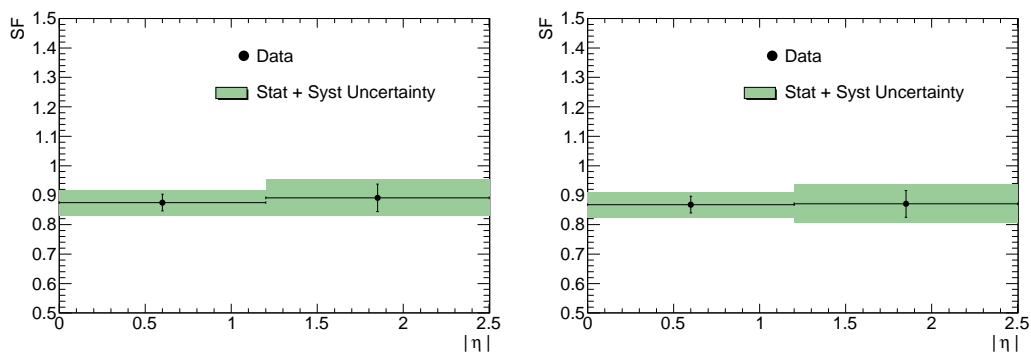
Figure 6.13: η dependence of the scale factor for the 50% operating point, left for the SV0 tagger, right for the JetProb tagger. No significant η dependence is visible in the chosen binning.

6.7.2 Comparison

Fig. 6.14 shows the comparison of the measured efficiencies to the efficiencies derived by the other methods described in Sec. 5.4.1 for three operating points. All methods agree within their combined uncertainties. The measurements cannot be combined since the efficiencies are derived for different classes of b-jets. The efficiency is derived for inclusive jets in the case of the p_T^{rel} method. It is derived for jets that pass the D*μ selection and respectively the top selection for the other methods. The measured scale factors with the top-quark based methods tends to be higher than the scale factor measured with the muon-in-jet based methods. With more statistics for the top-quark based methods it will be possible to investigate if this is a systematic effect.
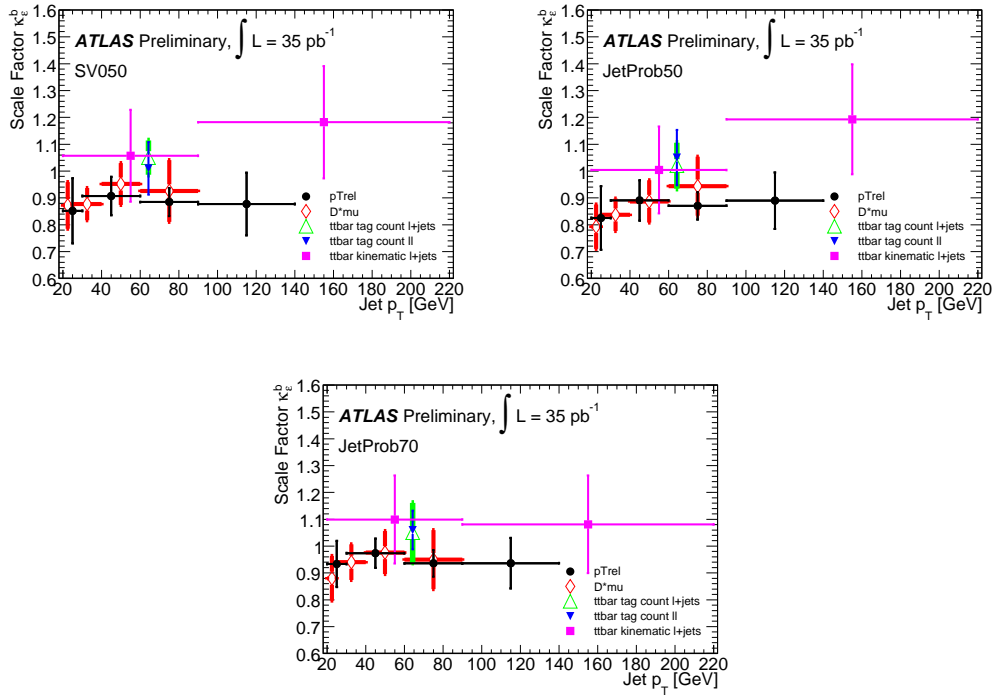
Figure 6.14: Comparison of measured scale factors with the p_T^{rel} method to the scale factor measured with the other available methods. The uncertainties are statistical uncertainty and systematic uncertainty combined. On the top left the SV050 operating point is shown, on the top right the JetProb50 operating point is shown and on the bottom the JetProb70 operating point is shown.

6.7.3 Cross-checks

Two cross-checks are performed to validate the results of the p_T^{rel} method. The intermediate results used to calculate the efficiency are the fraction of b-jets in the sample before tagging and in the sample after tagging. The fraction after tagging can be validated for the SV0 tagger using control plots of the SV0 mass distribution and the number of tracks used for the secondary vertex in the SV0 fit in data and simulation. For the JetProb tagger this is done as well but the cross-check is dominated by the zero bin where no secondary vertex is reconstructed. For simulation the template shapes are taken from the JXμ samples. The relative fractions of the jet flavors are the fit result from the p_T^{rel} method. The p_T^{rel} method cannot distinguish c-jets and light jets so most of the jets identified as light jets by the fit on the tagged sample are c-jets in reality (the fraction of light jets in a heavy flavor enriched sample after tagging is low due to the low fake rate of the b-tagging algorithms). The c-jet shape is also taken for the light jets to reflect this. The cross-checks for the different p_T bins and the different taggers can be seen in Figs. B.1 - B.16 in App. B.

The agreement of the data to simulation shapes is not perfect but a perfect agreement cannot be expected due to the usage of the c-jet template shape for light jets. In addition the mass distributions and number of track distributions are not modeled well on simulation as can be seen in Figs. B.17 - B.20. Here the cross-checks are

done before tagging and using the light jet shape from JX simulation. In one case the fractions from the p_T^{rel} method are used and in the other case the fractions from JX simulation are used. In both cases the comparisons show discrepancies.

However it can be demonstrated that the disagreement is covered by the calculated systematic errors and that the cross-checks therefore do not contradict the results of the p_T^{rel} method. The most striking disagreement is in the 90 GeV $< p_T <$ 140 GeV bin where the SV0 mass cross-check does not show good agreement. To show that the systematic error on the measurement covers this disagreement the error on the b-fraction after tagging is calculated (as opposed to the error on the resulting efficiency which is used for the result). The error on this fraction is 20% especially due to the muon reweighting systematic (which is expected since the muon spectrum shows the worst agreement in this bin, see Fig. 6.10). The b-fraction is increased by 20% and the light fraction is decreased by 20% and the cross-check is redone. Fig. 6.15 shows both the cross-check with the central value and after the 20% fraction changes and the agreement is good after the fraction change.
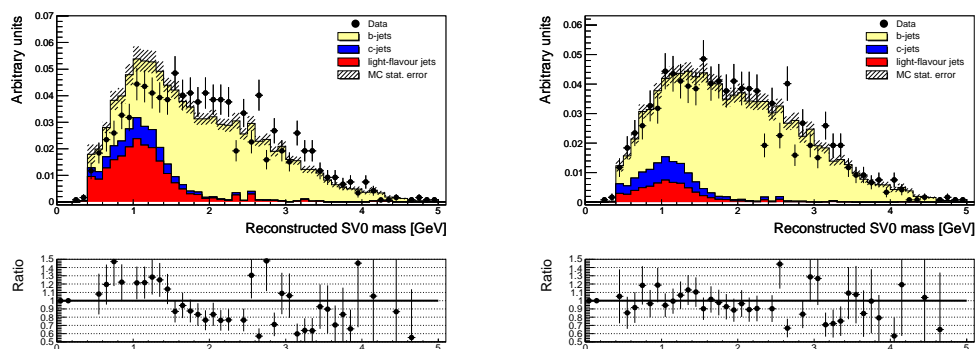
Figure 6.15: Data to simulation comparison of the mass of the reconstructed SV0 secondary vertex on the tagged sample with a 50% SV0 tagger efficiency. Left for the central fit, right with 20% increased b-jet fraction and 20% decreased light jet fraction. The templates are taken from the JXμ samples and the fractions are taken from the p_T^{rel} fit.

6.8 Application of b-tagging for a top-quark pair-production cross-section measurement

The b-tagging algorithms can be used to assist a measurement of the top-quark pair-production cross-section $\sigma_{t\bar{t}}$. As mentioned in Sec. 2.6 one of the top-quark decay products is a b-quark so a typical event where two top quarks are produced will contain two b-quarks. A multitude of measurements of $\sigma_{t\bar{t}}$ has been performed on the dataset of 2010. Some of the measurements use information from b-tagging algorithms while others do not. In this chapter the benefits of using the b-tagging algorithms are shown while at the same time showing that a smaller uncertainty on the calibration results would directly benefit the measurements since the b-tagging calibration uncertainty leads to the largest systematic contribution for the measurement of $\sigma_{t\bar{t}}$. Furthermore it will be shown how b-tagging can be used for data-driven cross-checks for one of the methods. The measurements presented are detailed in [58] and [59] and this chapter focuses on measurements in the semileptonic channel.

6.8.1 Event topology

The semileptonic decay topology discussed in Sec. 2.6 can be translated into objects measurable with the detector. The exact cut values are only given if they are the same for each of the discussed analyses. Most cut values differ slightly between analyses since they are individually optimized but the principle of the event selection is the same for all measurements.

The typical signature in the detector is an isolated electron or muon, missing energy from the neutrino and 4 jets with a p_T spectrum that is hard enough to distinguish them from the softer QCD spectrum. In addition two of the jets are b-jets and are likely to be tagged by b-tagging algorithms. This results in a common baseline event selection to suppress background events that contain leptons (muons or electrons) of $p_T > 20$ GeV in the acceptance of the Inner Detector. In the case of an electron the isolation requirement is satisfied by requiring that a cone around the electrons energy deposits in the calorimeter (excluding the smaller inside cone which contains the energy deposits from the electron itself) contains only a small amount of energy. The muon isolation is tested by excluding muons that have jets in the vicinity. The missing transverse energy is the imbalance of the vector sum of all calorimeter energies[4]. It is required to be > 35 GeV if the lepton is an electron and > 20 GeV if the lepton is a muon.

The different measurements impose different requirements on the additional jets in the event. Some explicitly require 4 high momentum jets while others combine samples where 3 high momentum jets are chosen with the 4 jet sample to retain more signal statistics. The events with lower jet multiplicities are also used to cross-check measurement inputs as shown in Sec. 6.8.4.

---

[4]In an event which does not contain neutrinos the hermeticity of the detector and momentum conservation imply that the total directed energy in the transverse plane has to be 0. If it is not 0 a particle has escaped the detector without detection and the only particle that does that is a neutrino.

6.8.2 Backgrounds

Background remnants that pass the event selection have similar event topologies or they occur at high rates so that they can fake similar event topologies. The main background for all $\sigma_{t\bar{t}}$ measurements stems from W-boson production in association with jets where the W-boson decays leptonically. It can be suppressed by *b*-tagging requirements except for the case where the associated jets include *b*-quarks. Z-boson production in association with jets is a similar but less important background. There is also a background contribution from QCD multi-jet events which is an example of the second class of backgrounds since those events only pass the event selection if a fake lepton is reconstructed[5]. There are additional small amounts of background events from single top-quark production and diboson production which are mostly fixed to their predictions from simulation with a generous uncertainty assigned.

6.8.3 Selected measurements of $\sigma_{t\bar{t}}$

The main published measurements of $\sigma_{t\bar{t}}$ use a combination of kinematic quantities like the aplanarity of the event or the η distribution of the lepton created in the semileptonic W-boson decay. The quantities are combined in a likelihood fit which is used to extract the amount of top-quark pair-production events assuming that the kinematic shapes are similar to the ones in simulation. The method without *b*-tagging results in $\sigma_{t\bar{t}} = 171 \pm 17(stat.)^{+20}_{-17}(syst.) \pm 6(lumi.)$ pb where the method with *b*-tagging results in $\sigma_{t\bar{t}} = 186 \pm 10(stat.)^{+21}_{-20}(syst.) \pm 6(lumi.)$ pb. The methods cannot be directly compared since they have more differences than the *b*-tagging requirement but it can be noted that the statistical error is lower when using *b*-tagging. This is due to a better suppression of the background and becomes more obvious when using the simpler count measurements.

The count measurements do not fit kinematic distributions but count the total number of events after the selection and subtract the expected or measured background. Without *b*-tagging the dominating systematic uncertainty of a count measurement is the uncertainty on the amount of W+jets events with 23%. With *b*-tagging this uncertainty this uncertainty is 8% [60]. Now the leading uncertainty is the *b*-tagging uncertainty with 12%. This implies that a refinement of the *b*-tagging calibration will improve this and other measurements and is an example of the importance of a good understanding of *b*-tagging.

6.8.4 One-dimensional kinematic fit method

A measurement that is a middle ground between the robustness of the count methods and the good performance of the sophisticated multidimensional likelihood fits uses a likelihood fit with only one input variable, in this case the lepton $|\eta|$. Kinematic shapes for top-quark pair-production events as well as for the W+jets events are derived from simulation and fit to data. The other backgrounds are fixed to their prediction from simulation with the exception of the multijet shape normalization which is derived from data. The fit result with the data points overlaid can be seen in

---

[5]This means that either a hadron is not stopped by the calorimeter and is measured as a muon in the muon system or that a high momentum muon from a heavy flavor decay is created and the isolation cut fails to discriminate against this.
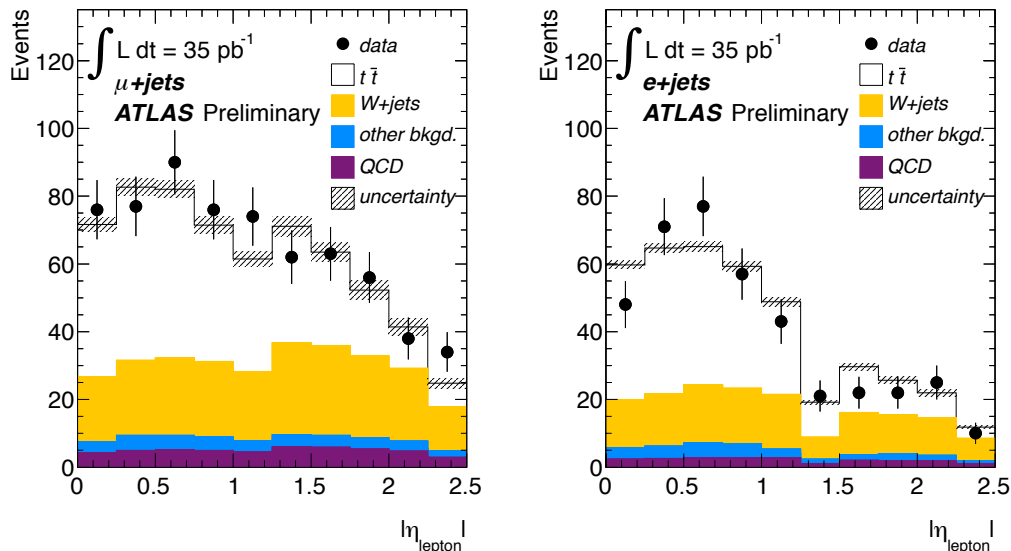
Figure 6.16: Distributions of the lepton $|\eta|$ in data and in the different sources from simulation. The normalization of the simulation templates is the fit result. It can be seen that the $t\bar{t}$ shape is more central than the other shapes. On the left the fit result in the muon channel is shown and on the right the fit result in the electron channel is shown.

Fig. 6.16. The measured cross-section is $\sigma_{t\bar{t}} = 204 \pm 25(stat.) \pm 39(syst.) \pm 7(lumi.)$ pb Details about this method can be found in [61].

Here a cross-check for the template shapes is shown. It is possible to extract pure kinematic shapes for the two templates that are free to float using b-tagging. This is very useful since it establishes trust in the method and helps to validate Monte Carlo simulation generators. For that purpose pure samples of W+jets event and top-pair events respectively are created.

The W+jets sample is created by requiring that an event must not contain a b-tag with an SV0 tagger weight higher than 5.85 which corresponds to the SV050 operating point calibrated in Chap. 5.4. Only three jets are required for this shape comparison to enhance the available data and simulation statistics. This results in a sample of 84.9% purity in the muon channel and 83.4% purity in the electron channel. Shape comparisons for different jet selections are shown in Fig. 6.17.

The $t\bar{t}$ shape is extracted by requiring two jets with an SV0 tagging weight greater than 5.85. This result in a purity of 91.7% in the muon channel and a purity of 91.3% in the electron channel. A shape comparison of this shape on simulation and data is shown in Fig. 6.18. The compared shapes agree well within their statistical errors which is underlined by the result of a Kolmogorov test that is displayed in the figures.
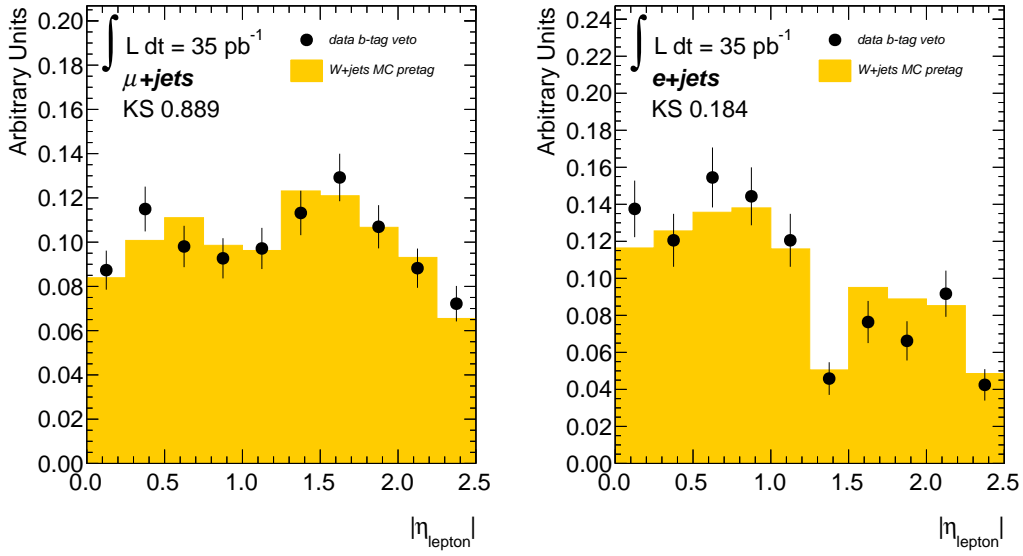
Figure 6.17: Distributions of $|\eta|$ in events with three jets with an anti-*b*-tag selection for the muon (left) and electron (right) channels. As simulation the prediction for the W+jets shape before tagging is shown.
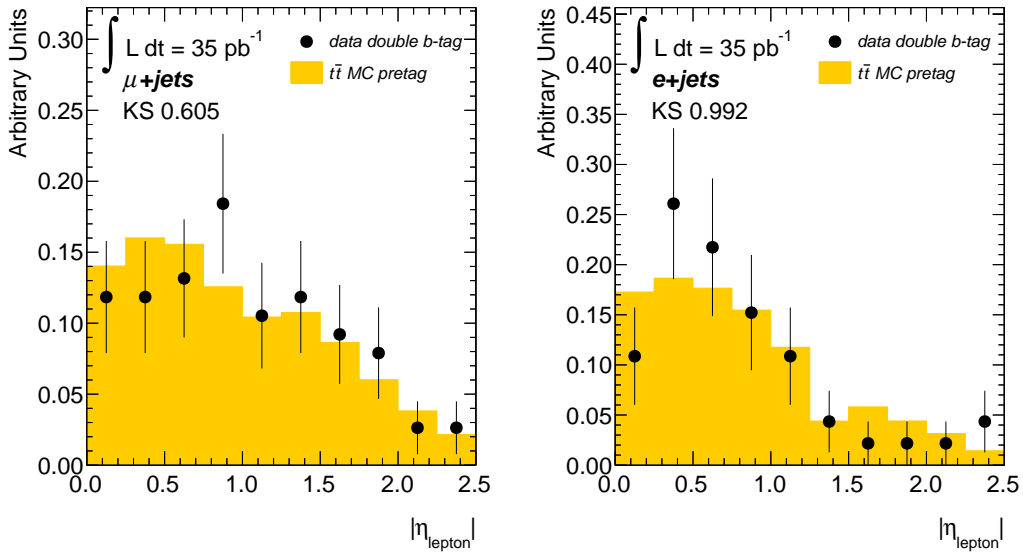
Figure 6.18: Comparisons of the $t\bar{t}$ shape with normal selection from simulation with double *b*-tagged data for the muon channel and for the electron channel. As simulation the prediction for the $t\bar{t}$ shape before tagging is shown.

7 Summary and Conclusion

The sensor studies presented in this work show that the ATLAS Pixel Detector is an operational device that can be used with detector conditions (like the supply voltages) in nominal operating ranges. Sensor damages are low with 0.1% disconnected bumps which guarantees high efficiency data-taking. The measured quantities will be re-evaluated and a trend over time will be established which will aid in the understanding of radiation damage or other damage (like thermal stress due to cooling cycles) to the detector and will therefore help in the planning process of future detector upgrades.

The high efficiency of the Pixel Detector is vital for the performance of the b-tagging algorithms which has been assessed and is close to the prediction from simulation. With the p_T^{rel} method it is found that the scale factor that has to be applied to transform the simulated b-tagging efficiency into the b-tagging efficiency on data is between 0.85 and 1.0 for most operating points of the JetProb and of the SV0 tagger. The variation of this scale factor when changing p_T between 20 GeV and 140 GeV or $|\eta|$ between 0 and 2.5 is smaller than the combined errors of the measurements.

The measurement of the b-tagging scale factors allow measurements of $\sigma_{t\bar{t}}$ with b-tagging. The application of b-tagging generally lowers the uncertainty on the measurements as has been shown so b-tagging is a useful tool. The usefulness will extend as soon as calibrations are done for the advanced taggers which generally have a higher efficiency while at the same time having a lower fake rate. This will result in a better signal enhancement over background and therefore in lower measurement errors.

The measurement uncertainties that arise from the combined measurement error on the b-tagging scale factors tend to be the dominating systematic uncertainties as is the case for the $\sigma_{t\bar{t}}$ measurements. This means that it is beneficial to improve the necessary future calibrations of b-tagging algorithms to reduce this uncertainty. This will be achieved especially by exploiting the top-quark based calibration algorithms more since the luminosity in 2011 is high enough to provide decent event counts for these methods.

It is possible to search for specific signatures of Higgs boson decays or processes predicted by theories that extend the standard model and compare them to expectations from simulations. This will eventually lead to the discovery of those particles if they exist. The application of b-tagging will aid a first discovery and especially the subsequent cross-section measurements for the discovered particles in a similar way as it helps the $\sigma_{t\bar{t}}$ measurement.
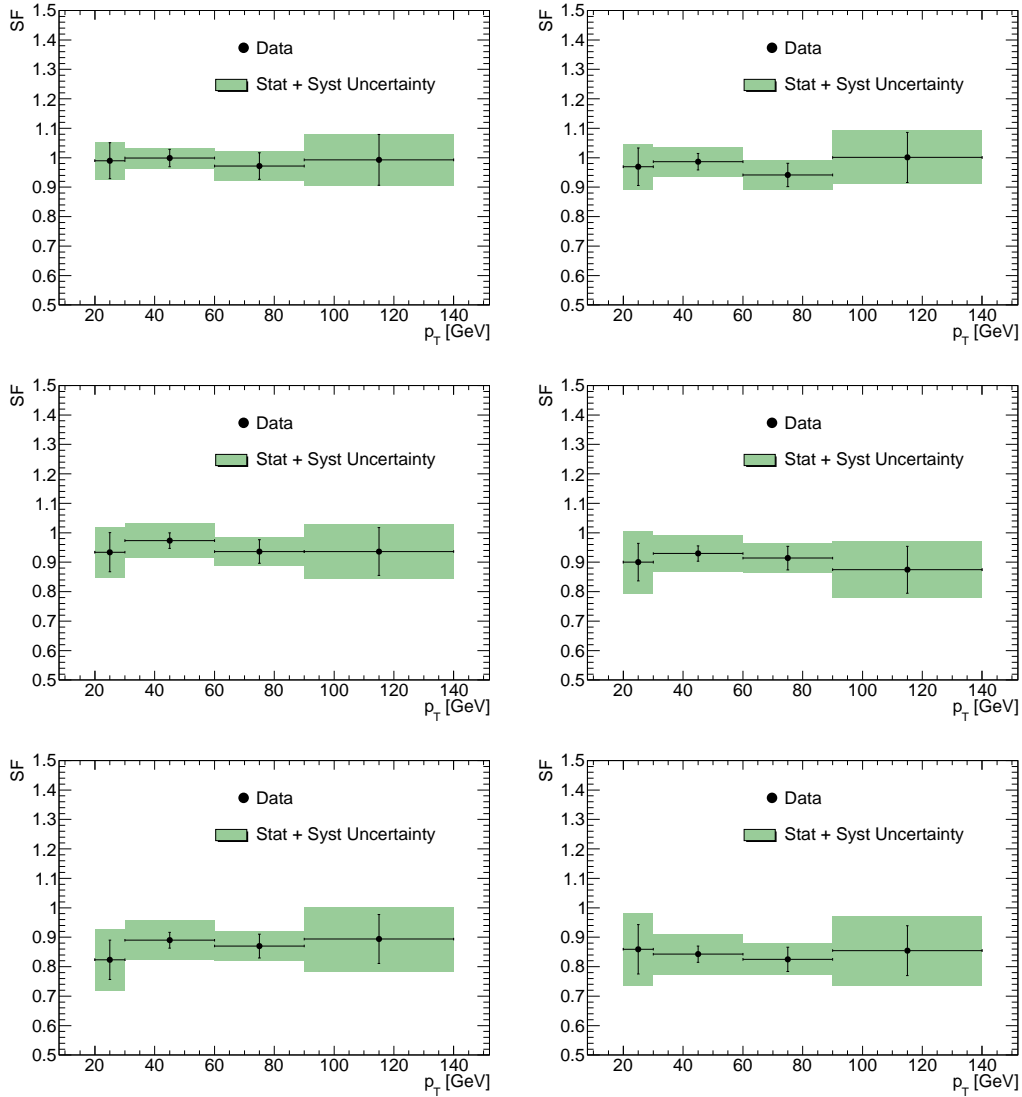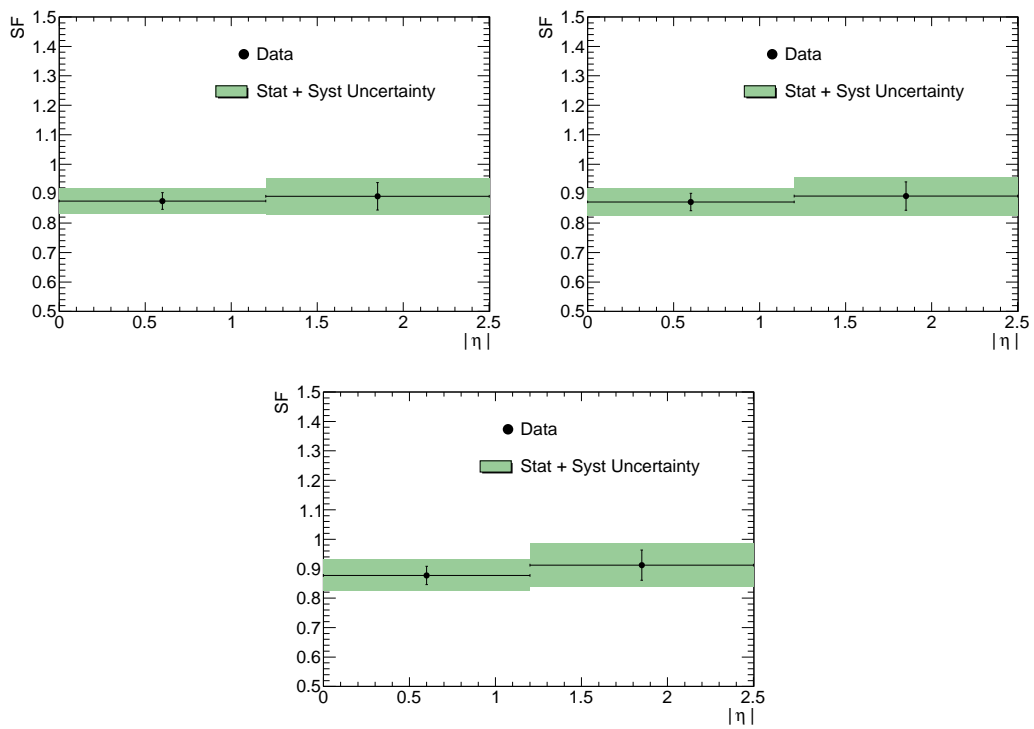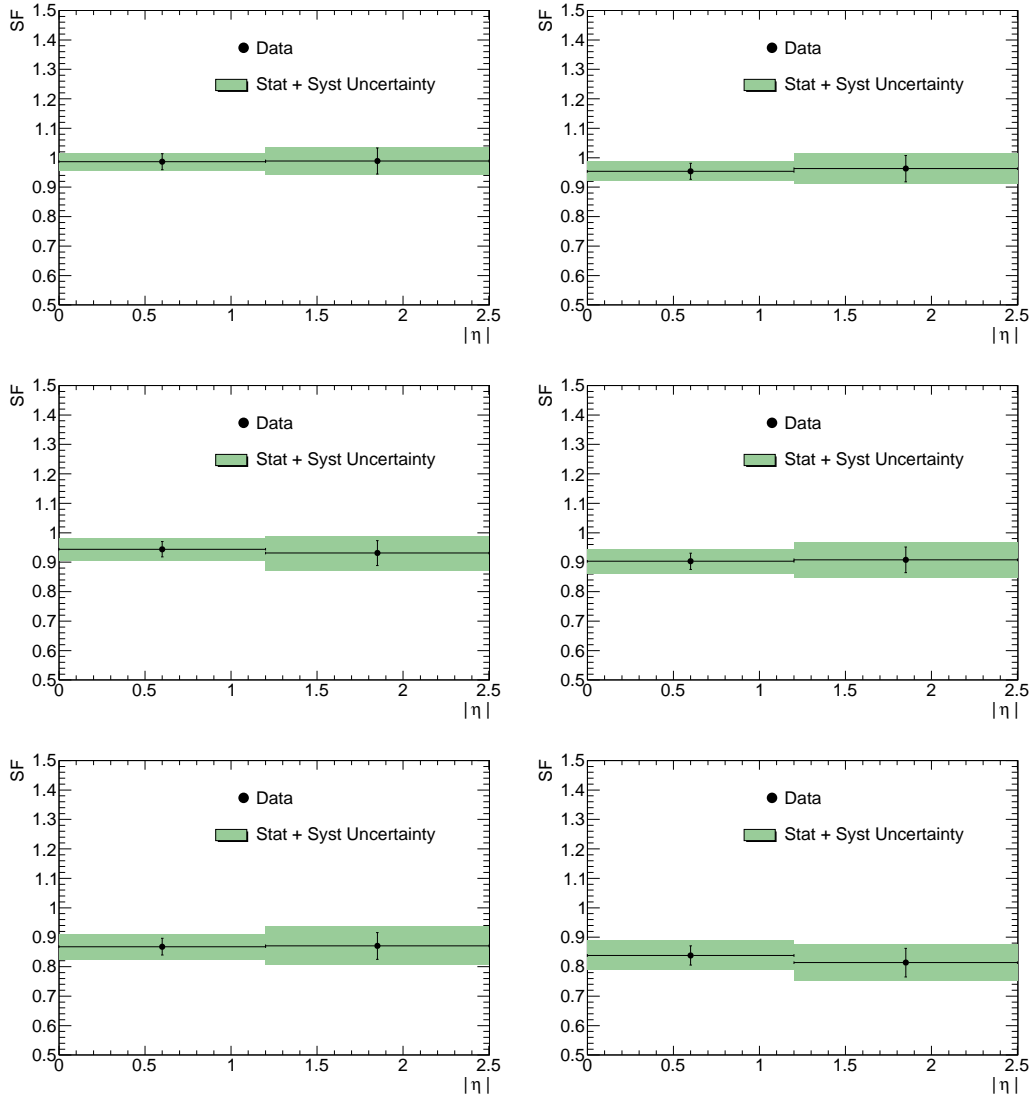
A p_T^{rel} method results
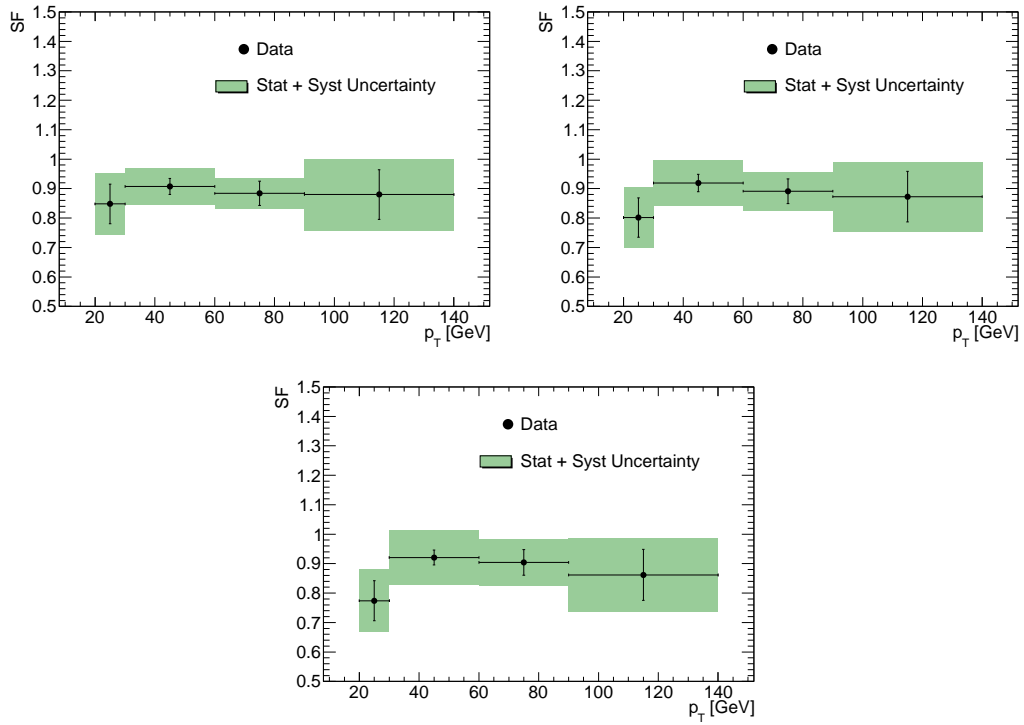
Figure A.1: Scale factor versus p_T for the different operating points under study. Shown are SV050 on the top left, SV045 on the top right and SV040 on the bottom.
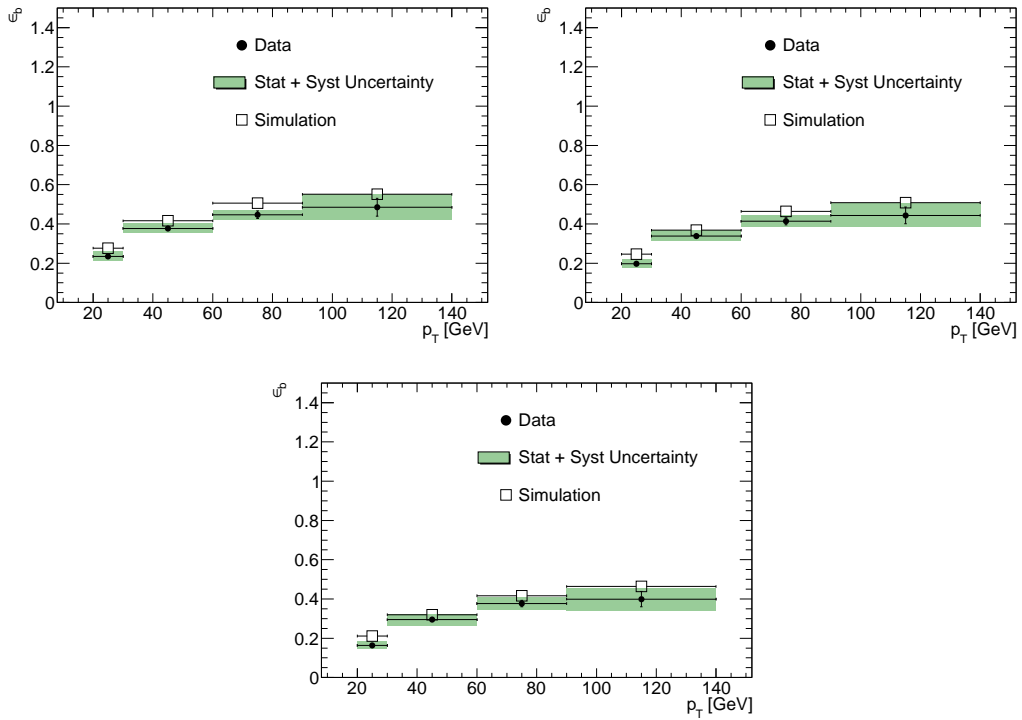
Figure A.2: Scale factor versus p$_\mathrm{T}$ for the different operating points under study. From top left to bottom right the operating points shown are JetProb90, JetProb80, JetProb70, JetProb60, JetProb50 and JetProb40.
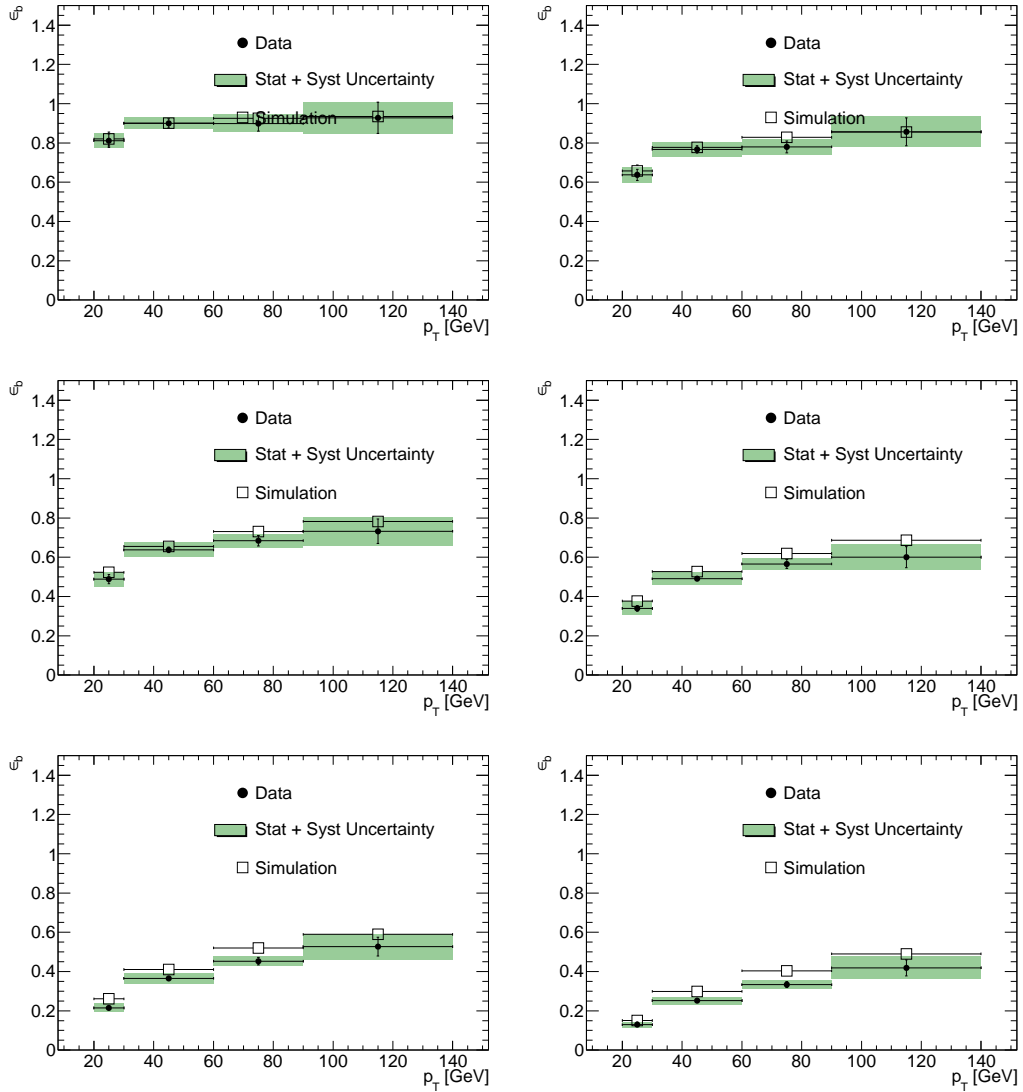
Figure A.3: Scale factor versus $|\eta|$ for the different operating points under study. Shown are SV050 on the top left, SV045 on the top right and SV040 on the bottom.
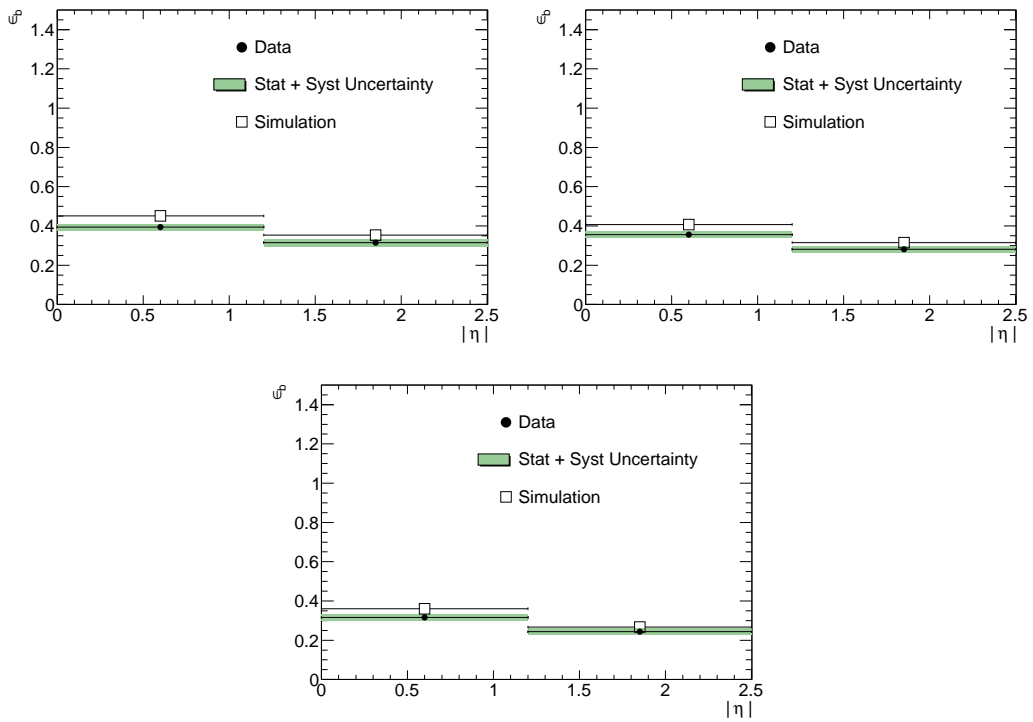
Figure A.4: Scale factor versus $|\eta|$ for the different operating points under study. From top left to bottom right the operating points shown are JetProb90, JetProb80, JetProb70, JetProb60, JetProb50 and JetProb40.

Figure A.5: Comparison of measured efficiency and predicted efficiency from simulation versus p_T for the different operating points under study. Shown are SV050 on the top left, SV045 on the top right and SV040 on the bottom.

Figure A.6: Comparison of measured efficiency and predicted efficiency from simulation versus p_T for the different operating points under study. From top left to bottom right the operating points shown are JetProb90, JetProb80, JetProb70, JetProb60, JetProb50 and JetProb40.
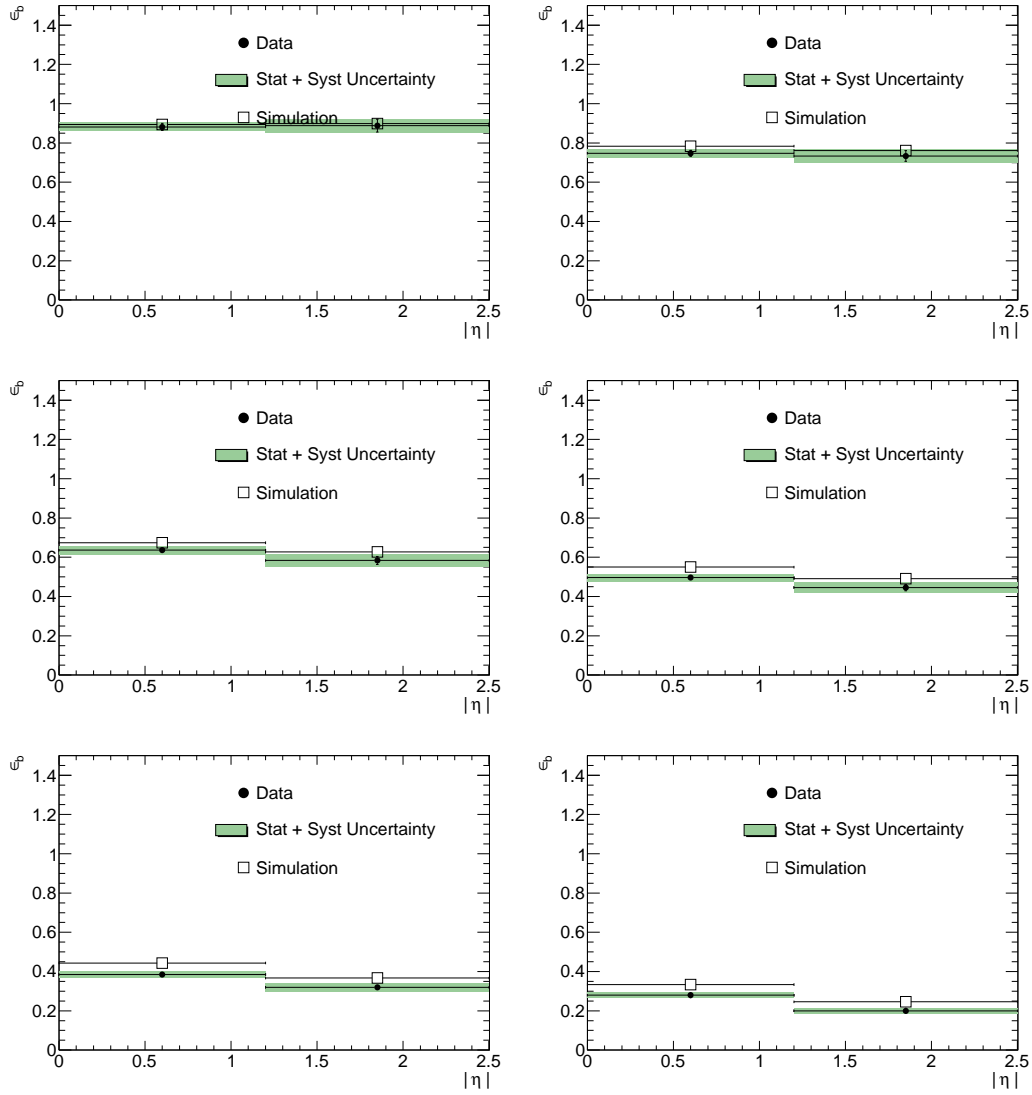
Figure A.7: Comparison of measured efficiency and predicted efficiency from simulation versus $|\eta|$ for the different operating points under study. Shown are SV050 on the top left, SV045 on the top right and SV040 on the bottom.

Figure A.8: Comparison of measured efficiency and predicted efficiency from simulation versus $|\eta|$ for the different operating points under study. From top left to bottom right the operating points shown are JetProb90, JetProb80, JetProb70, JetProb60, JetProb50 and JetProb40.
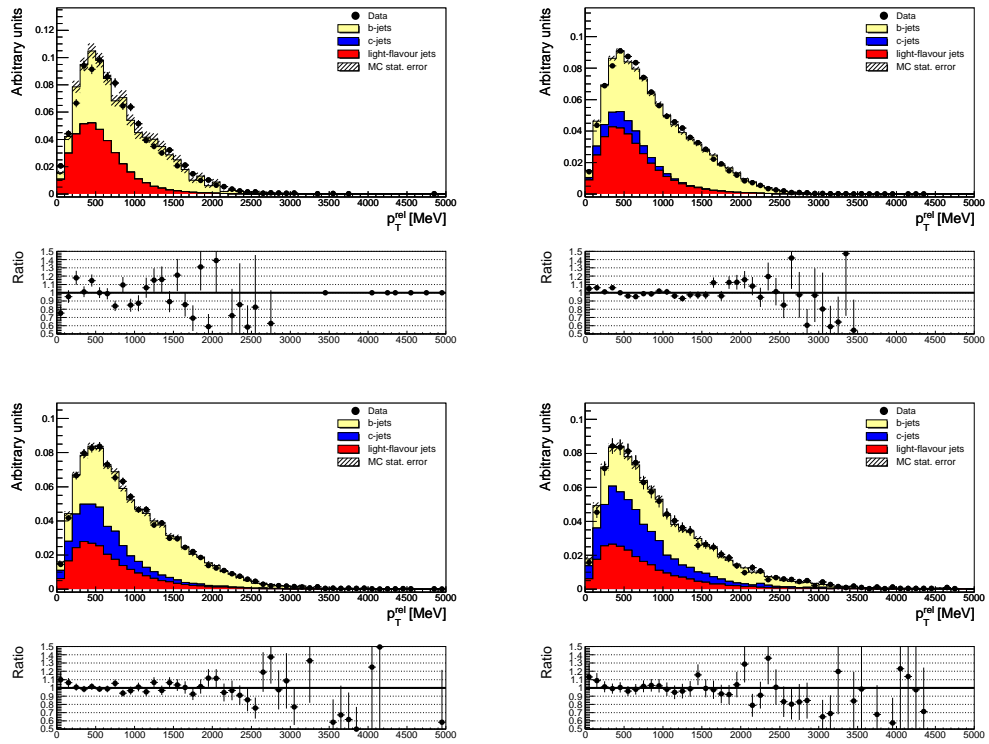
Figure A.9: Result from the p_T^{rel} fit on the sample before tagging. From top left to bottom right the 20 GeV - 30 GeV, the 30 GeV - 60 GeV the 60 GeV - 90 GeV and the 90 GeV - 140 GeV bins are shown.
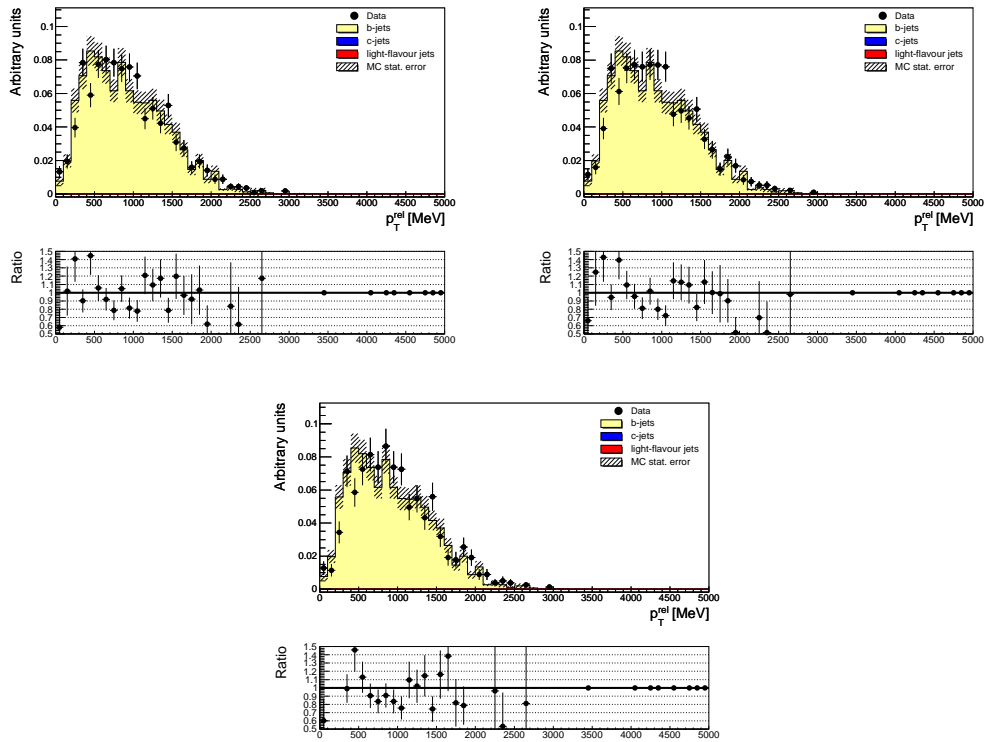
Figure A.10: Result from the p$_T^{rel}$ fit on the sample after tagging for the 20 GeV - 30 GeV bin. Shown are SV050 on the top left, SV045 on the top right and SV040 on the bottom.

Figure A.11: Result from the p_T^{rel} fit on the sample after tagging for the 20 GeV - 30 GeV bin. From top left to bottom right the operating points shown are JetProb90, JetProb80, JetProb70, JetProb60, JetProb50 and JetProb40.

Figure A.12: Result from the p$_{\mathrm{T}}^{\mathrm{rel}}$ fit on the sample after tagging for the 30 GeV - 60 GeV bin. Shown are SV050 on the top left, SV045 on the top right and SV040 on the bottom.

Figure A.13: Result from the p_T^{rel} fit on the sample after tagging for the 30 GeV - 60 GeV bin. From top left to bottom right the operating points shown are JetProb90, JetProb80, JetProb70, JetProb60, JetProb50 and JetProb40.
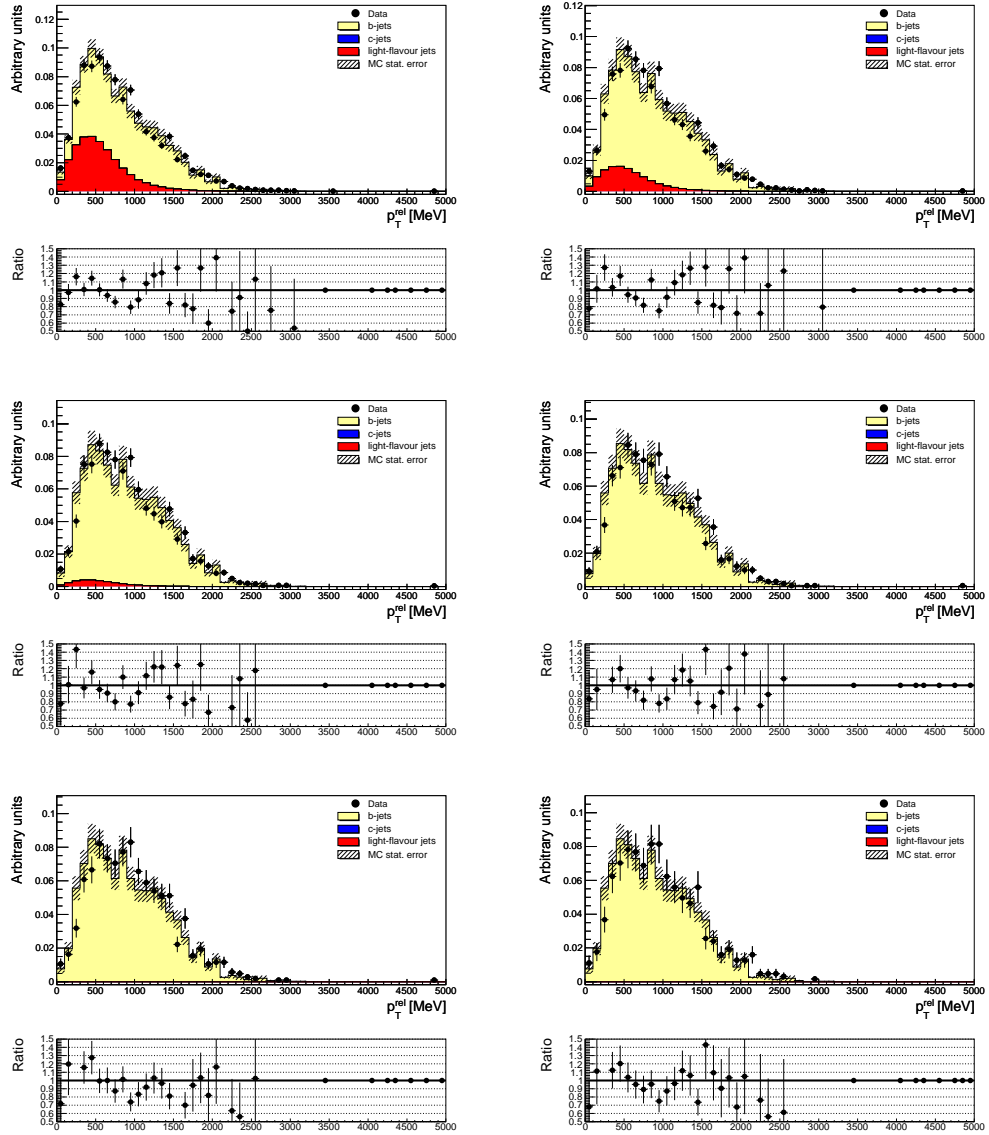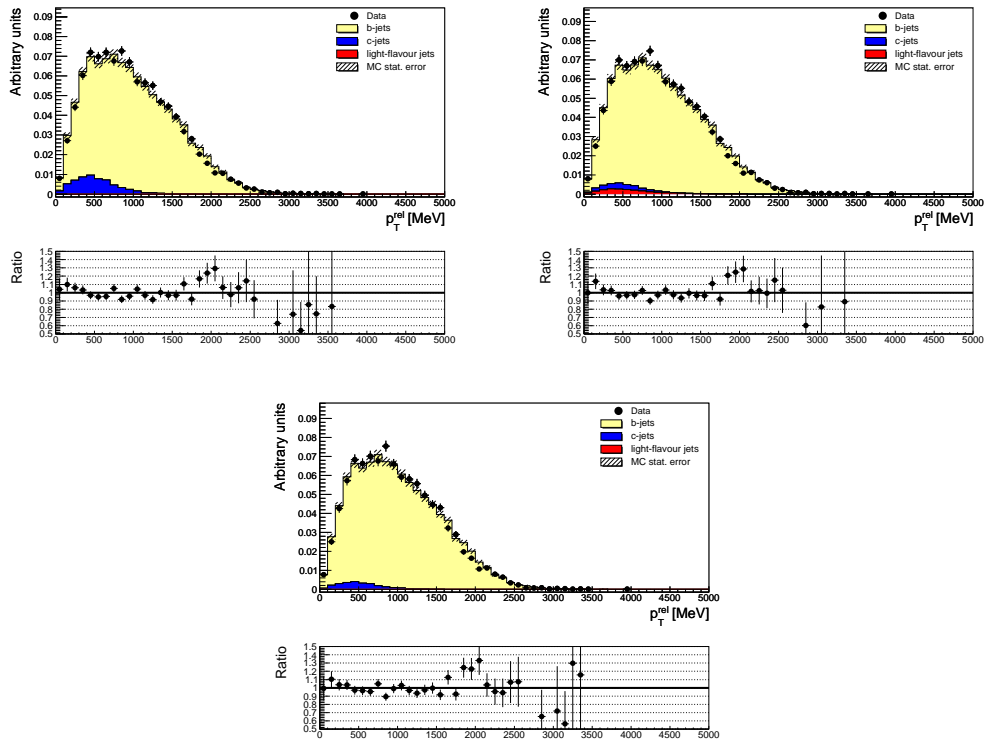
Figure A.14: Result from the p$_T^{rel}$ fit on the sample after tagging for the 60 GeV - 90 GeV bin. Shown are SV050 on the top left, SV045 on the top right and SV040 on the bottom.
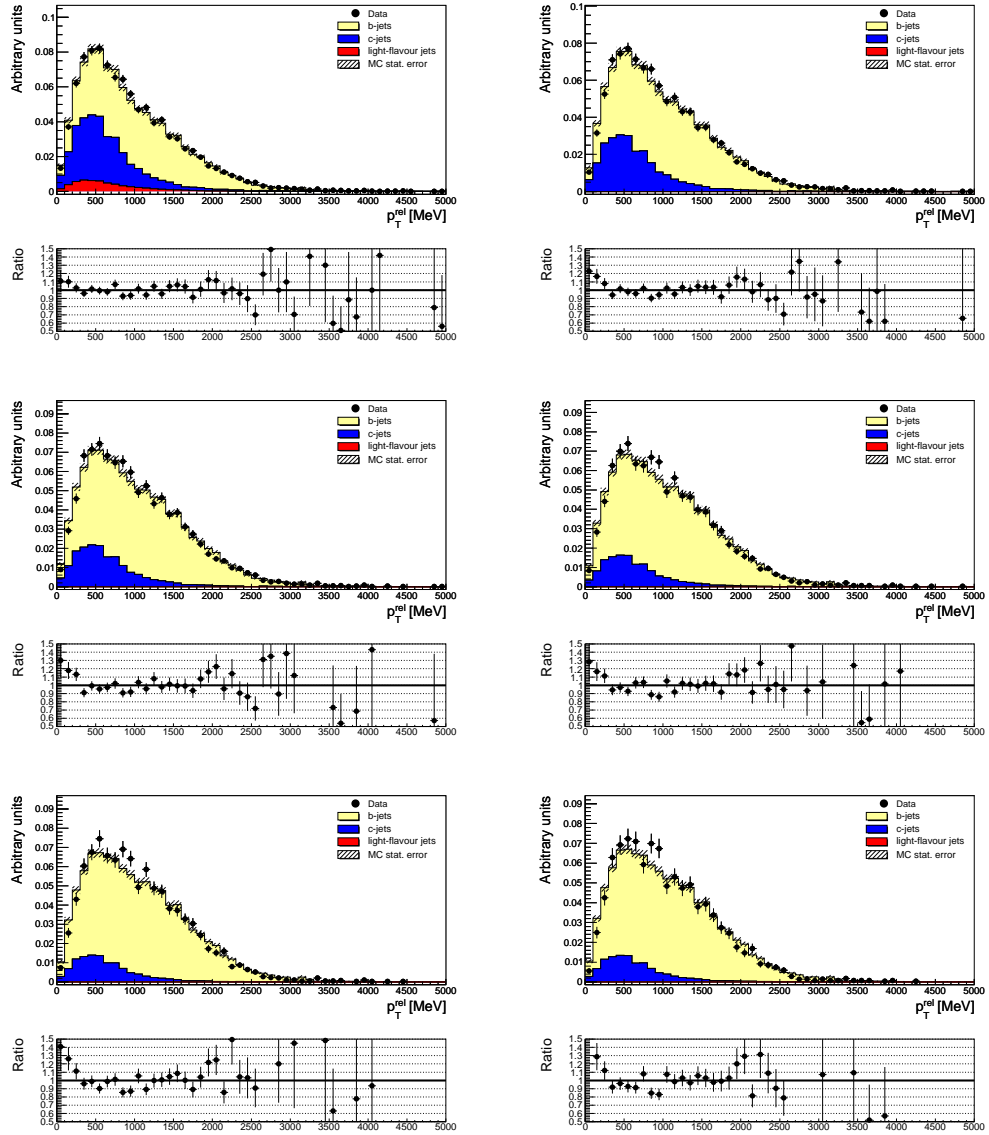
Figure A.15: Result from the p_T^{rel} fit on the sample after tagging for the 60 GeV - 90 GeV bin. From top left to bottom right the operating points shown are JetProb90, JetProb80, JetProb70, JetProb60, JetProb50 and JetProb40.
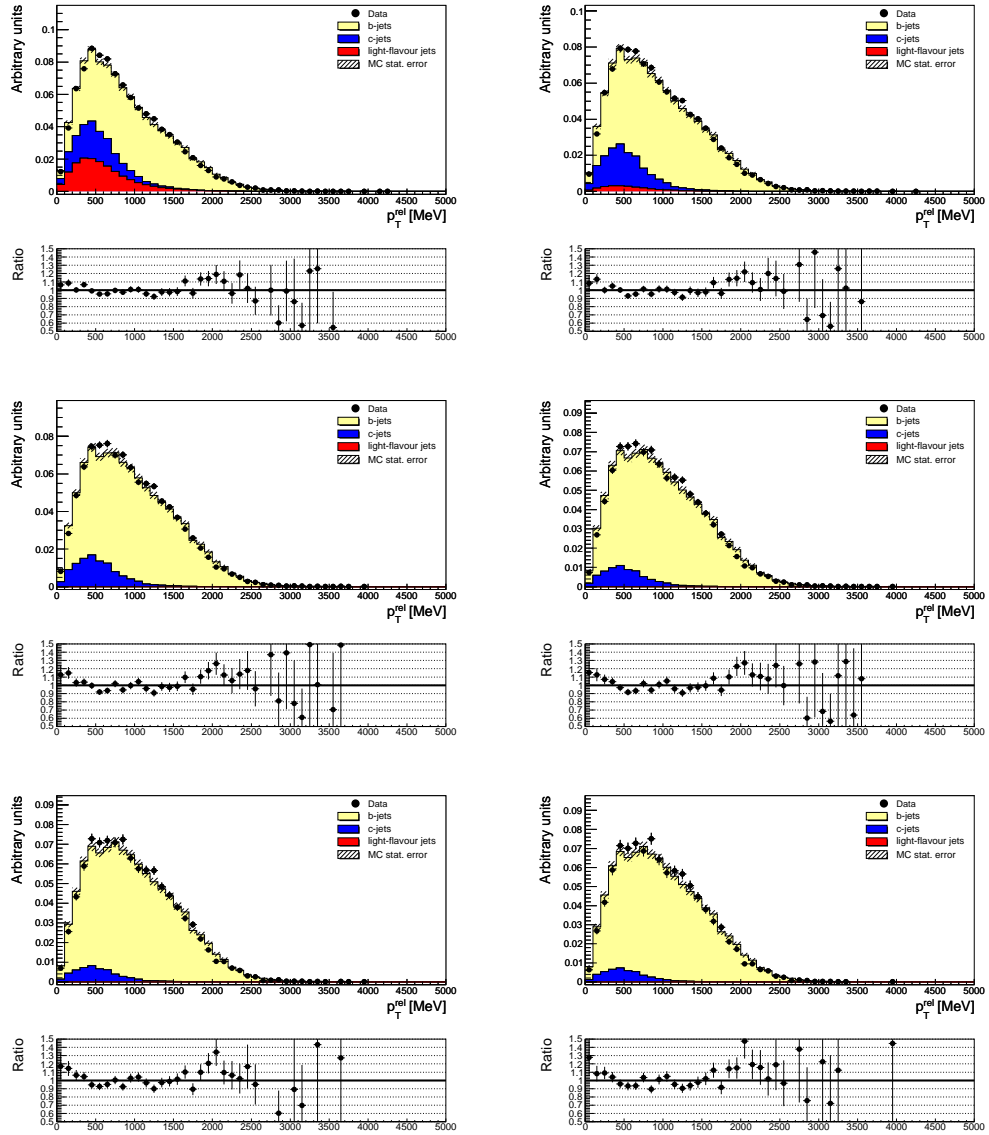
Figure A.16: Result from the p$_T^{rel}$ fit on the sample after tagging for the 90 GeV - 140 GeV bin. Shown are SV050 on the top left, SV045 on the top right and SV040 on the bottom.
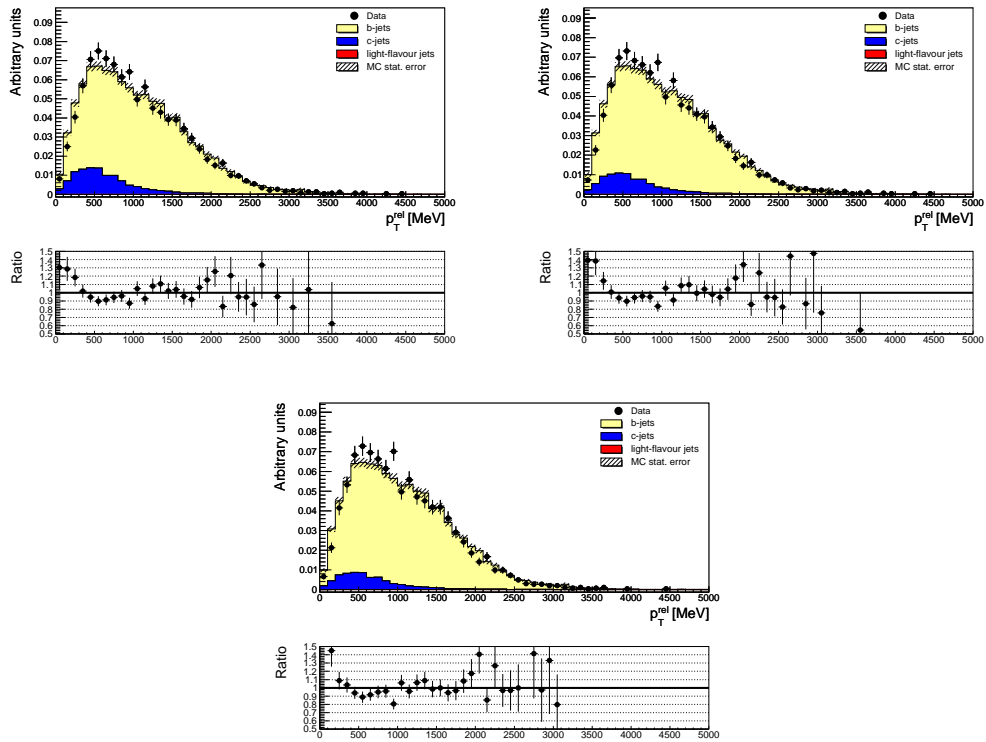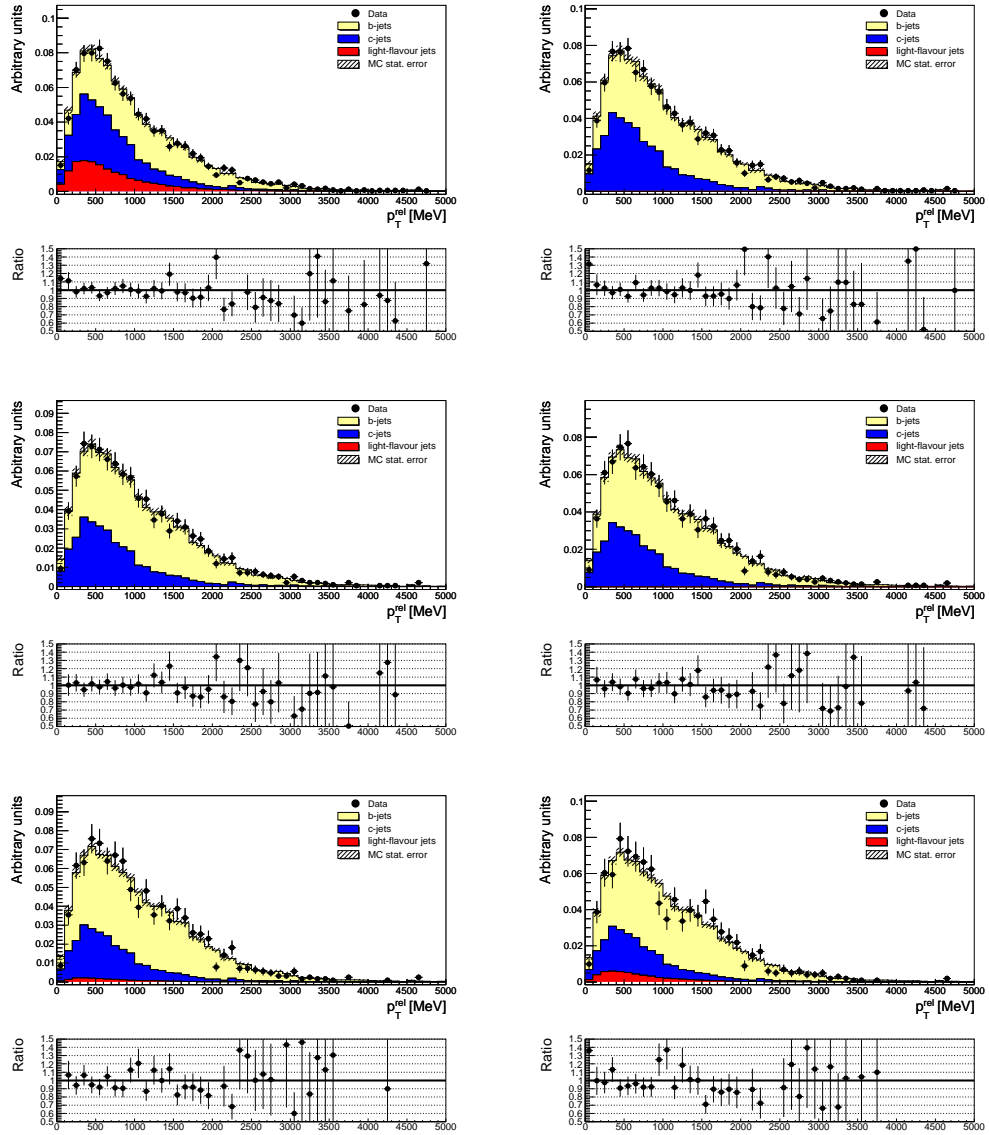
Figure A.17: Result from the p_T^{rel} fit on the sample after tagging for the 90 GeV - 140 GeV bin. From top left to bottom right the operating points shown are JetProb90, JetProb80, JetProb70, JetProb60, JetProb50 and JetProb40.
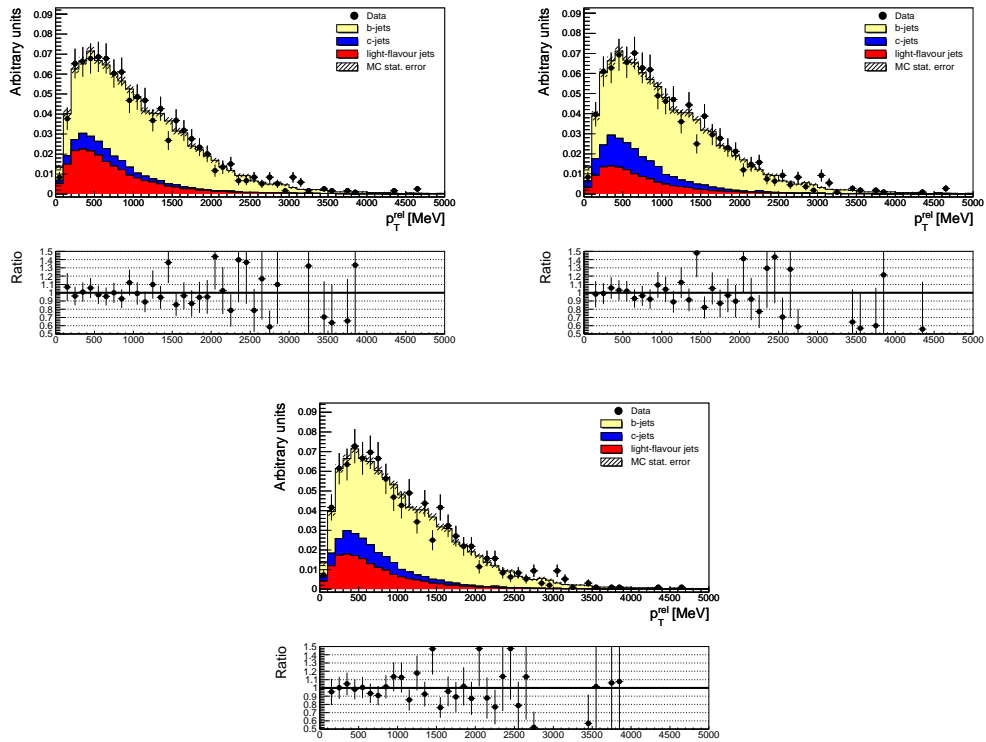
B p_T^{rel} method cross-checks
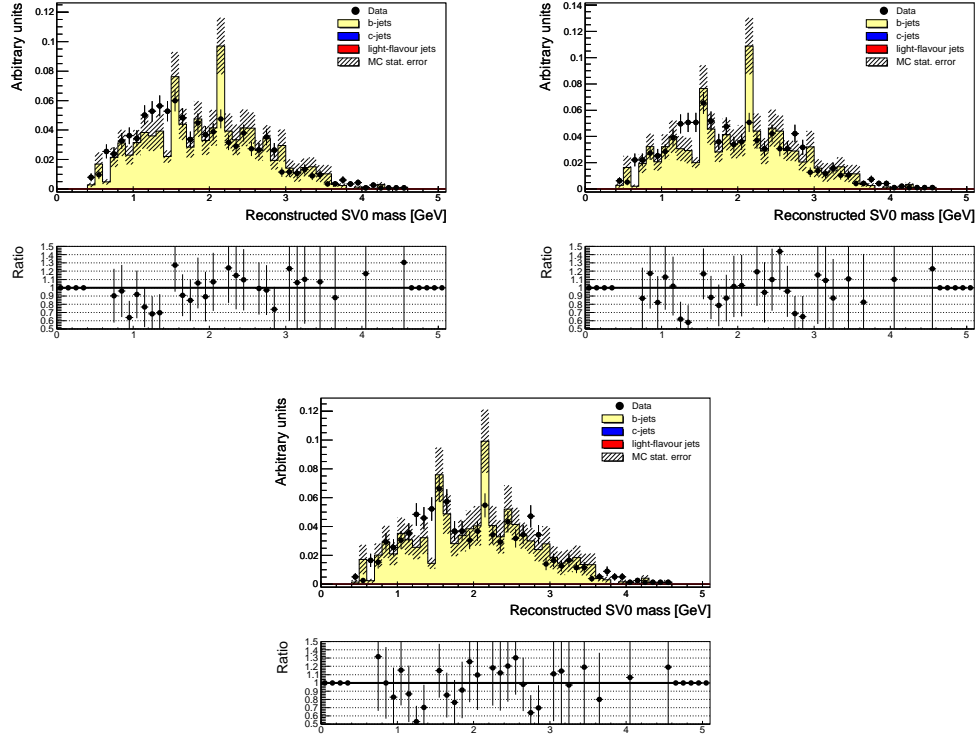
Figure B.1: Data to simulation comparison of the mass of the reconstructed SV0 secondary vertex on the tagged sample for the 20 GeV - 30 GeV bin. The templates are taken from the JXμ samples and the fractions are taken from the p_T^{rel} fit. Shown are SV050 on the top left, SV045 on the top right and SV040 on the bottom. The c-jet template is used for the light jets since the fit cannot distinguish c-jets from light jets but a c-jet is more likely to be tagged. Therefore perfect agreement cannot be expected.
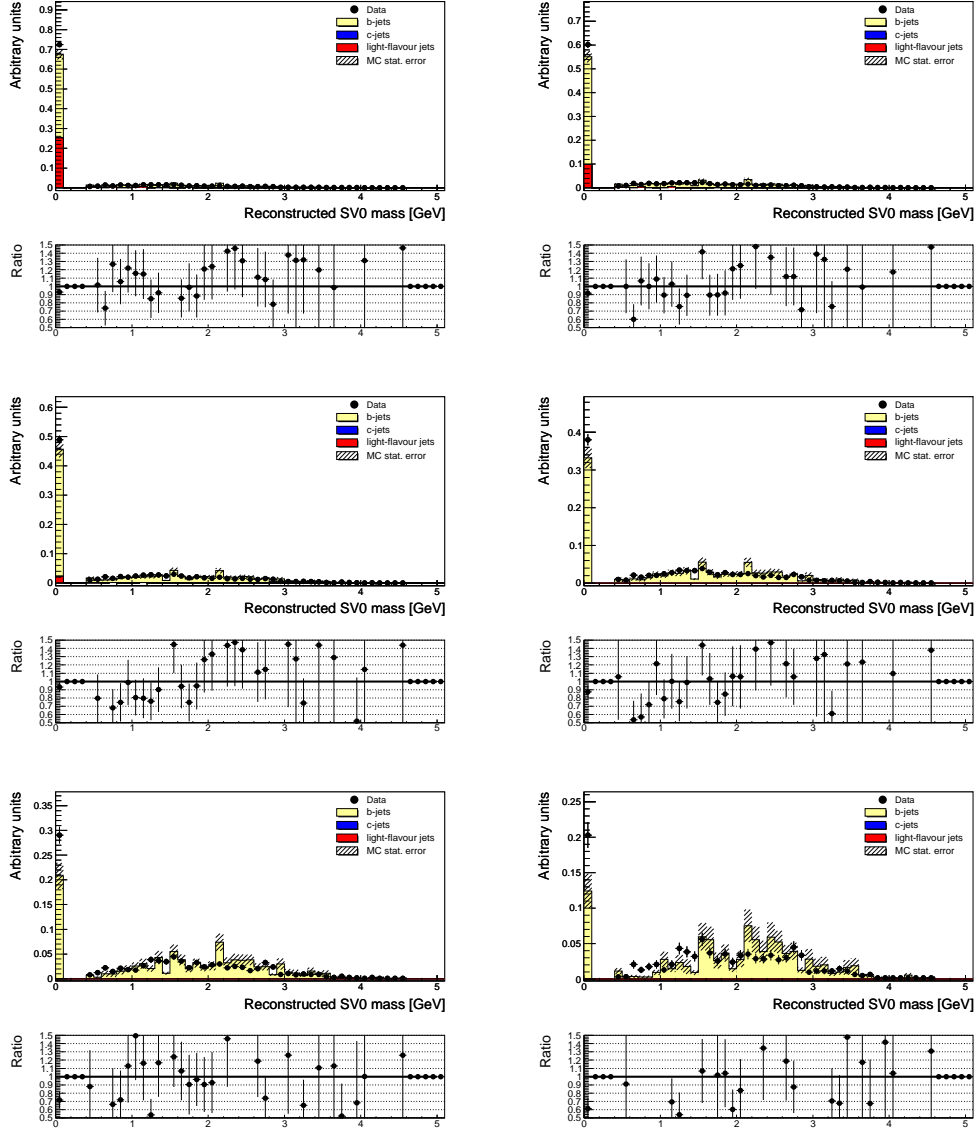
Figure B.2: Data to simulation comparison of the mass of the reconstructed SV0 secondary vertex on the tagged sample for the 20 GeV - 30 GeV bin. The templates are taken from the JXμ samples and the fractions are taken from the p$_T^{rel}$ fit. From top left to bottom right the operating points shown are JetProb90, JetProb80, JetProb70, JetProb60, JetProb50 and JetProb40. The c-jet template is used for the light jets since the fit cannot distinguish c-jets from light jets but a c-jet is more likely to be tagged. Therefore perfect agreement cannot be expected.

Figure B.3: Data to simulation comparison of the mass of the reconstructed SV0 secondary vertex on the tagged sample for the 30 GeV - 60 GeV bin. The templates are taken from the JXμ samples and the fractions are taken from the p_T^{rel} fit. Shown are SV050 on the top left, SV045 on the top right and SV040 on the bottom. The c-jet template is used for the light jets since the fit cannot distinguish c-jets from light jets but a c-jet is more likely to be tagged. Therefore perfect agreement cannot be expected.

Figure B.4: Data to simulation comparison of the mass of the reconstructed SV0 secondary vertex on the tagged sample for the 30 GeV - 60 GeV bin. The templates are taken from the JXμ samples and the fractions are taken from the p$_{\mathrm{T}}^{\mathrm{rel}}$ fit. From top left to bottom right the operating points shown are JetProb90, JetProb80, JetProb70, JetProb60, JetProb50 and JetProb40. The c-jet templa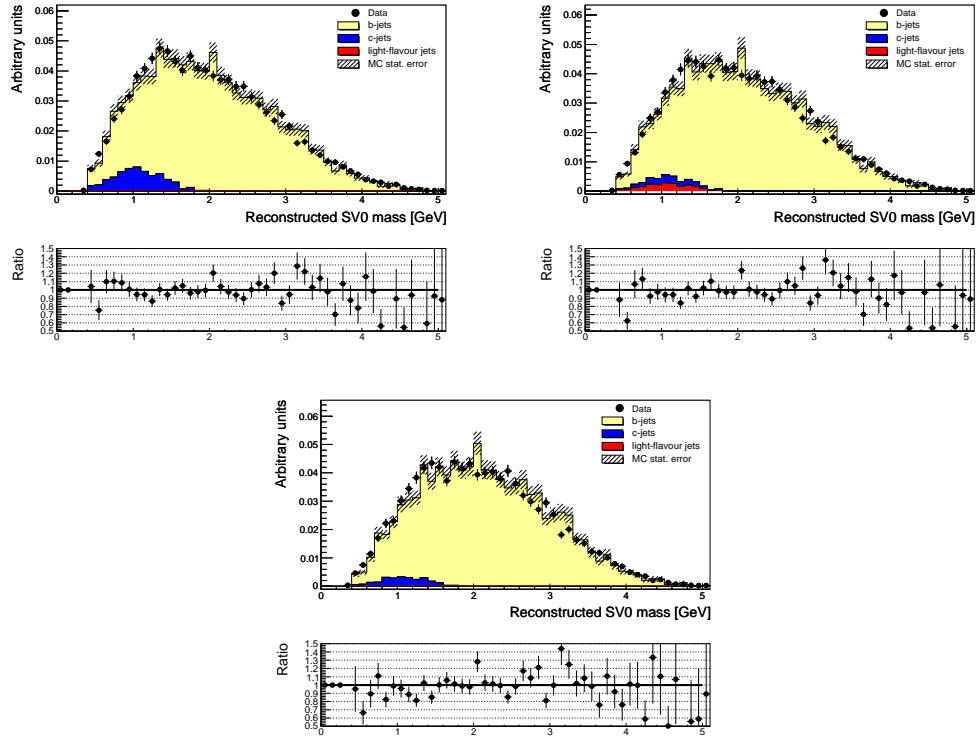te is used for the light jets since the fit cannot distinguish c-jets from light jets but a c-jet is more likely to be tagged. Therefore perfect agreement cannot be expected.
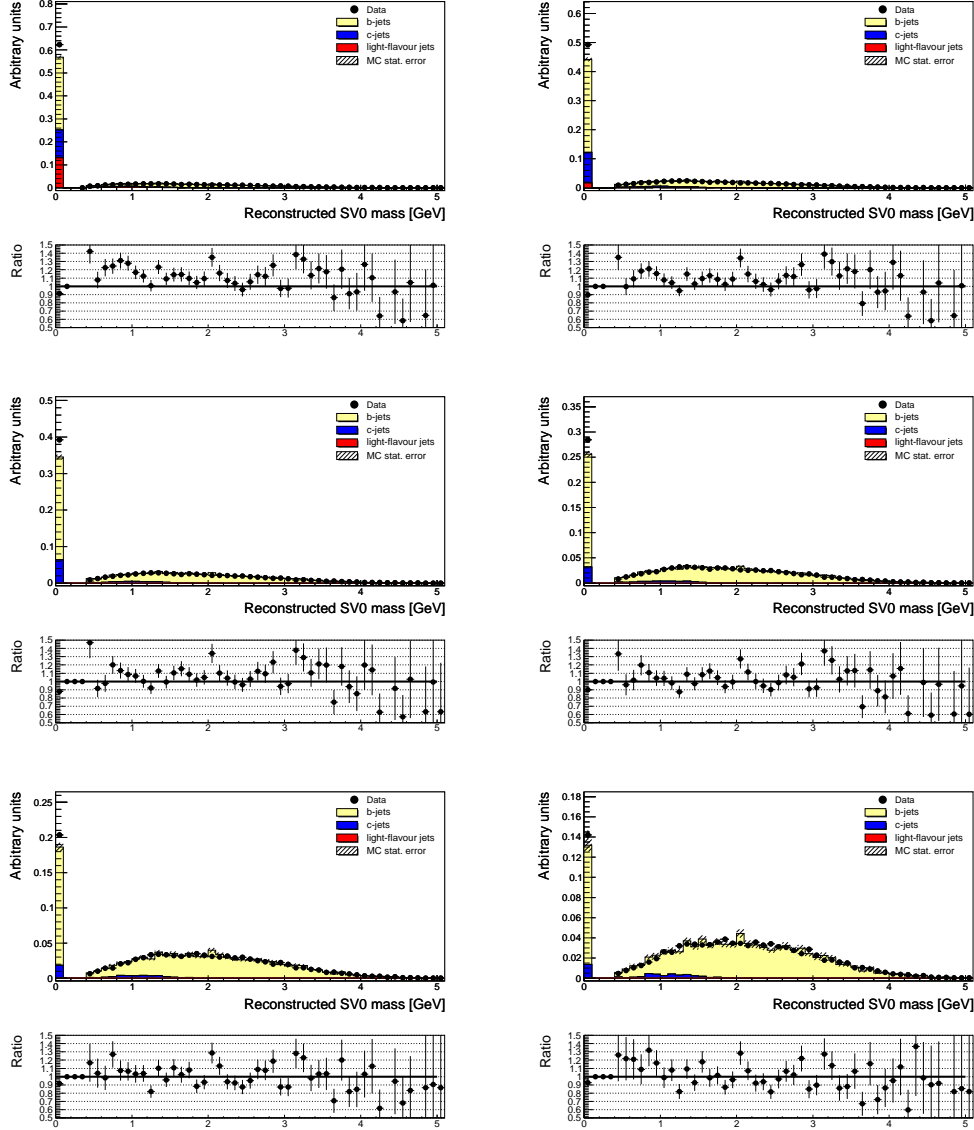
Figure B.5: Data to simulation comparison of the mass of the reconstructed SV0 secondary vertex on the tagged sample for the 60 GeV - 90 GeV bin. The templates are taken from the JXμ samples and the fractions are taken from the p_T^{rel} fit. Shown are SV050 on the top left, SV045 on the top right and SV040 on the bottom. The c-jet template is used for the light jets since the fit cannot distinguish c-jets from light jets but a c-jet is more likely to be tagged. Therefore perfect agreement cannot be expected.

Figure B.6: Data to simulation comparison of the mass of the reconstructed SV0 secondary vertex on the tagged sample for the 60 GeV - 90 GeV bin. The templates are taken from the JXμ samples and the fractions are taken from the p$_T^{\text{rel}}$ fit. From top left to bottom right the operating points shown are JetProb90, JetProb80, JetProb70, JetProb60, JetProb50 and JetProb40. The c-jet template is used for the light jets since the fit cannot distinguish c-jets from light jets but a c-jet is more likely to be tagged. Therefore perfect agreement cannot be expected.
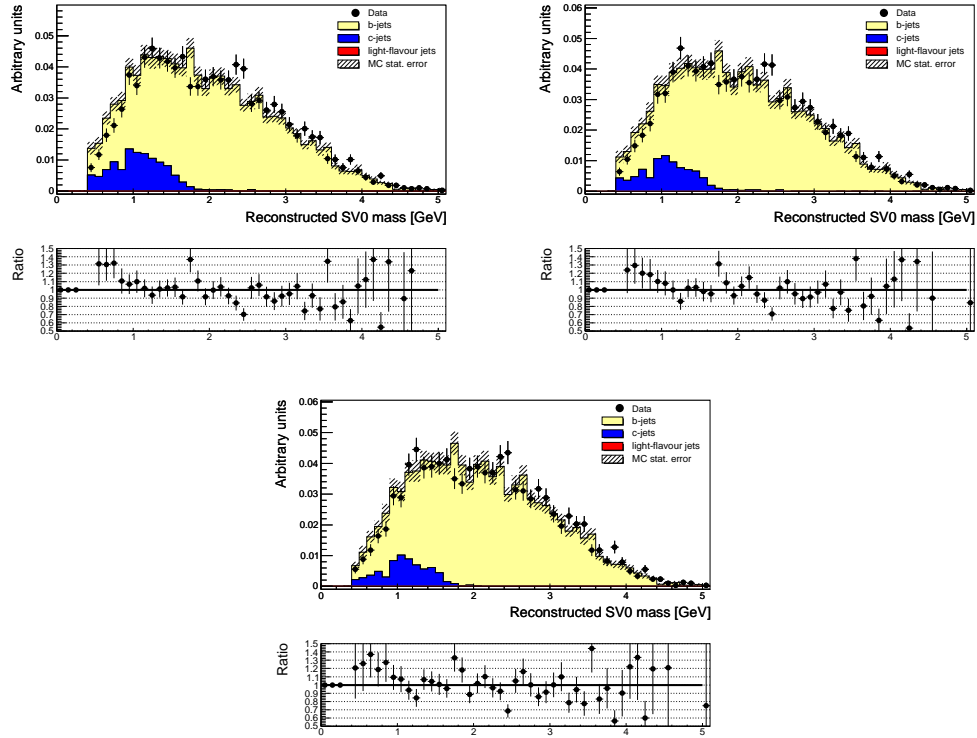
Figure B.7: Data to simulation comparison of the mass of the reconstructed SV0 secondary vertex on the tagged sample for the 90 GeV - 140 GeV bin. The templates are taken from the JXμ samples and the fractions are taken from the p_T^{rel} fit. Shown are SV050 on the top left, SV045 on the top right and SV040 on the bottom. The c-jet template is used for the light jets since the fit cannot distinguish c-jets from light jets but a c-jet is more likely to be tagged. Therefore perfect agreement cannot be expected.
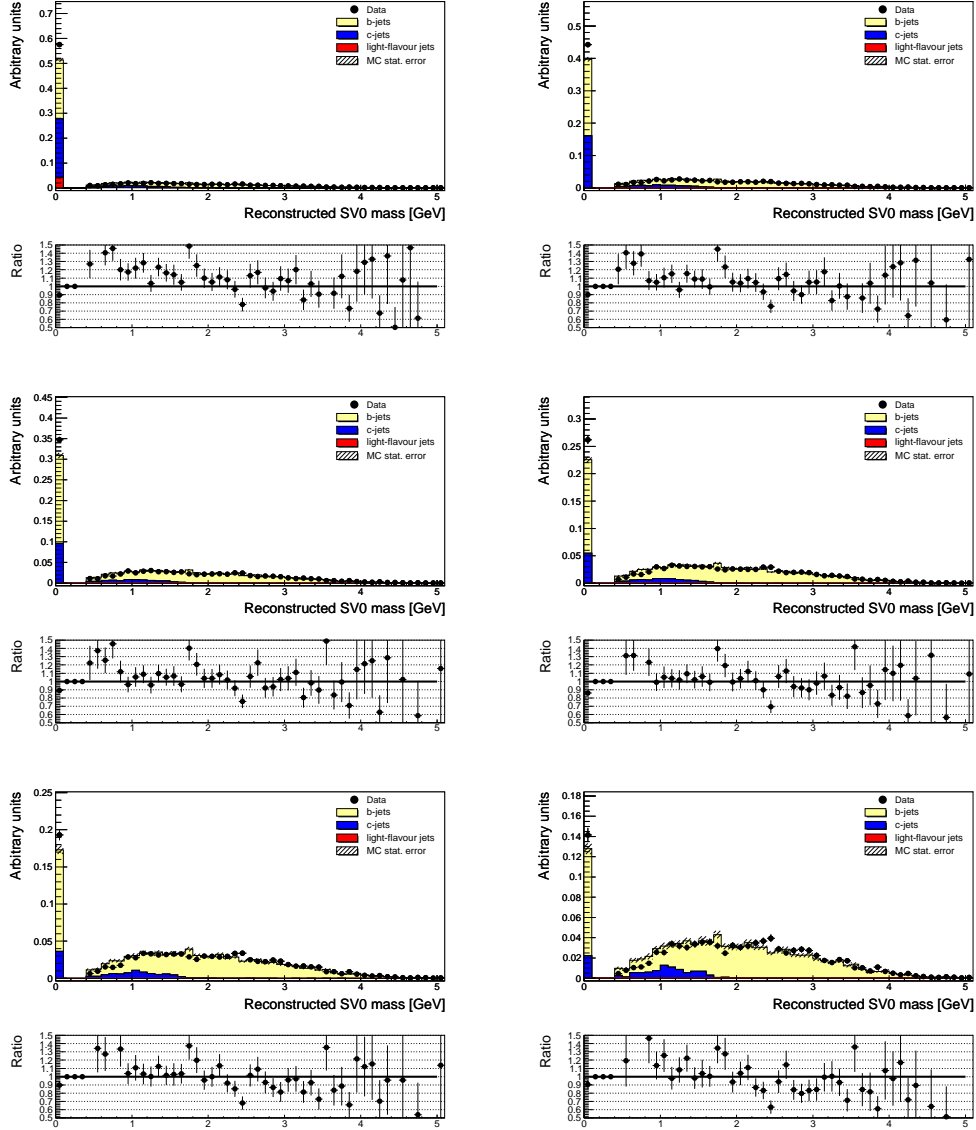
Figure B.8: Data to simulation comparison of the mass of the reconstructed SV0 secondary vertex on the tagged sample for the 90 GeV - 140 GeV bin. The templates are taken from the JXμ samples and the fractions are taken from the p$_T^{rel}$ fit. From top left to bottom right the operating points shown are JetProb90, JetProb80, JetProb70, JetProb60, JetProb50 and JetProb40. The c-jet template is used for the light jets since the fit cannot distinguish c-jets from light jets but a c-jet is more likely to be tagged. Therefore perfect agreement cannot be expected.

Figure B.9: Data to simulation comparison of the number of tracks used for the reconstructed SV0 secondary vertex on the tagged sample for the 20 GeV - 30 GeV bin. The templates are taken from the JXμ samples and the fractions are taken from the p_T^{rel} fit. Shown are SV050 on the top left, SV045 on the top right and SV040 on the bottom. The c-jet template is used for the light jets since the fit cannot distinguish c-jets from light jets but a c-jet is more likely to be tagged. Therefore perfect agreement cannot be expected.
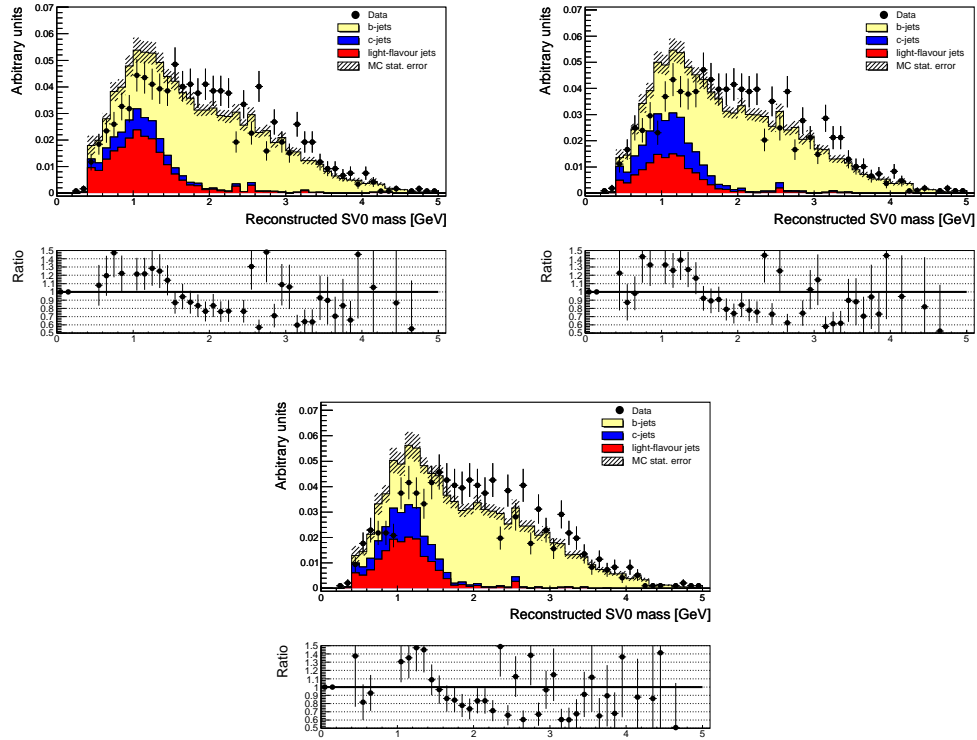
Figure B.10: Data to simulation comparison of the number of tracks used for the reconstructed SV0 secondary vertex on the tagged sample for the 20 GeV - 30 GeV bin. The templates are taken from the JXμ samples and the fractions are taken from the p$_T^{rel}$ fit. From top left to bottom right the operating points shown are JetProb90, JetProb80, JetProb70, JetProb60, JetProb50 and JetProb40. The c-jet template is used for the light jets since the fit cannot distinguish c-jets from light jets but a c-jet is more likely to be tagged. Therefore perfect agreement cannot be expected. The 0 bin is suppressed.
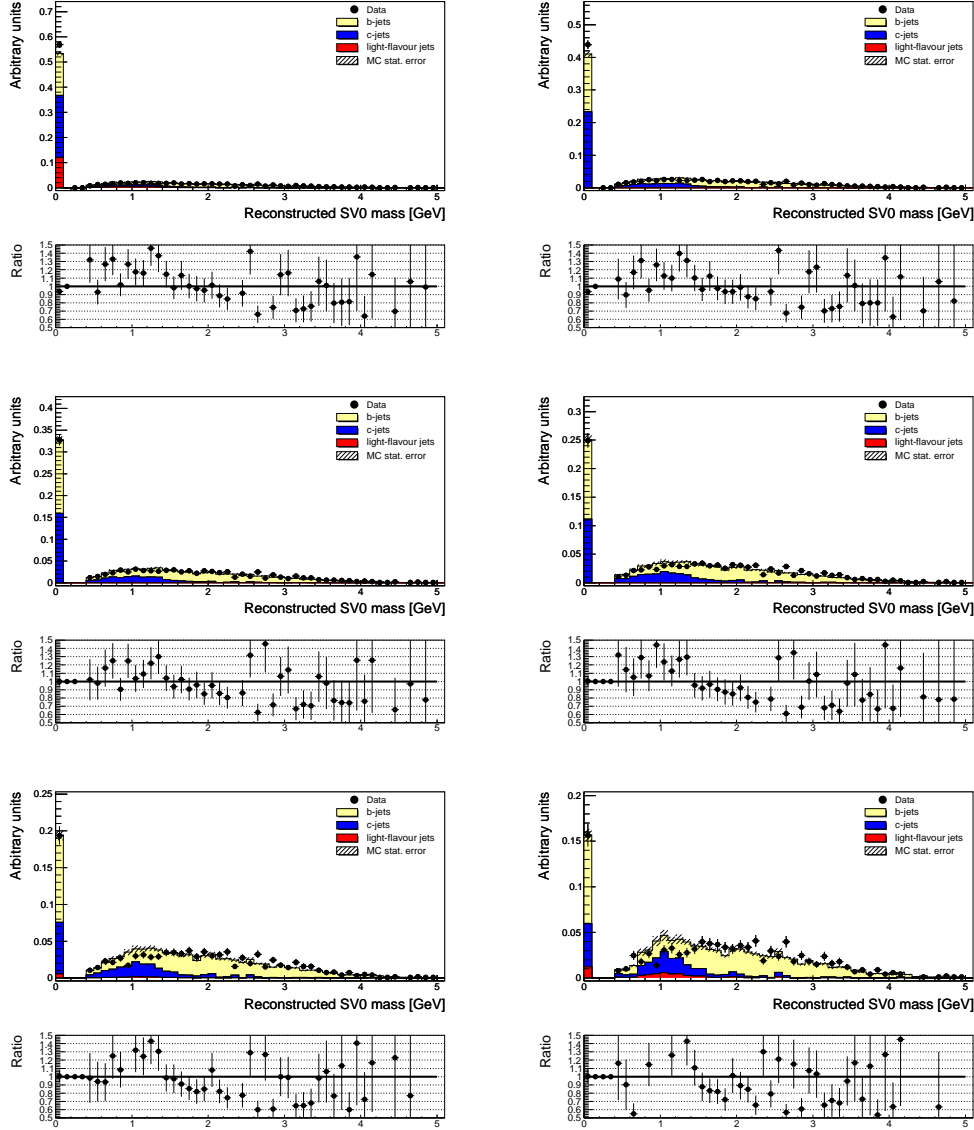
Figure B.11: Data to simulation comparison of the number of tracks used for the reconstructed SV0 secondary vertex on the tagged sample for the 30 GeV - 60 GeV bin. The templates are taken from the JXμ samples and the fractions are taken from the p$_T^{rel}$ fit. Shown are SV050 on the top left, SV045 on the top right and SV040 on the bottom. The c-jet template is used for the light jets since the fit cannot distinguish c-jets from light jets but a c-jet is more likely to be tagged. Therefore perfect agreement cannot be expected.
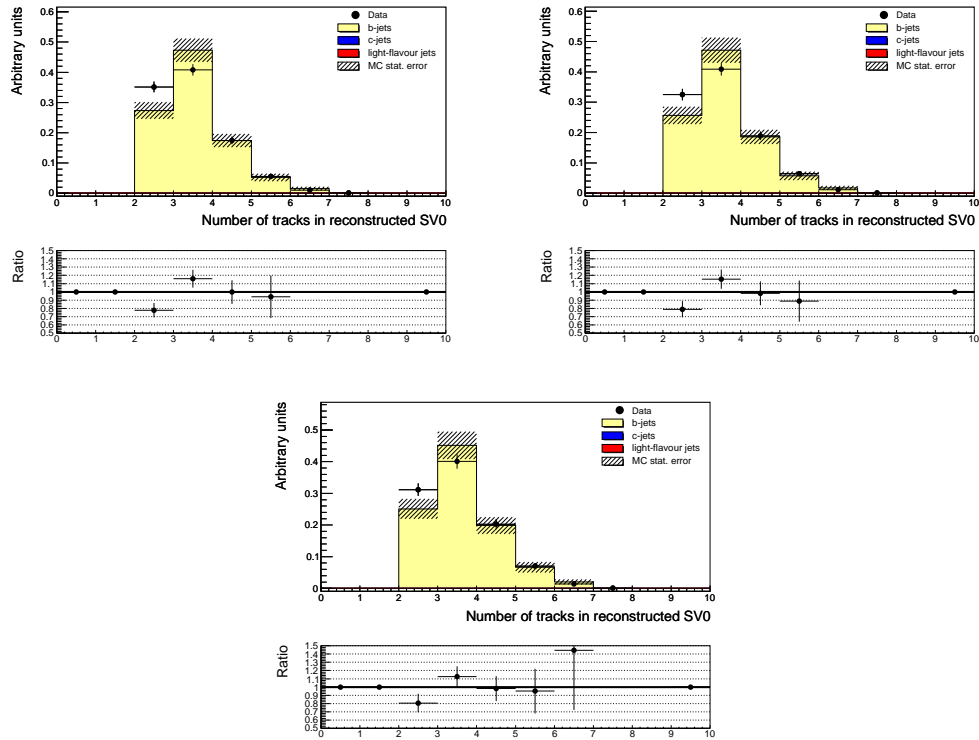
Figure B.12: Data to simulation comparison of the number of tracks used for the reconstructed SV0 secondary vertex on the tagged sample for the 30 GeV - 60 GeV bin. The templates are taken from the JXμ samples and the fractions are taken from the p$_{\mathrm{T}}^{\mathrm{rel}}$ fit. From top left to bottom right the operating points shown are JetProb90, JetProb80, JetProb70, JetProb60, JetProb50 and JetProb40. The c-jet template is used for the light jets since the fit cannot distinguish c-jets from light jets but a c-jet is more likely to be tagged. Therefore perfect agreement cannot be expected. The 0 bin is suppressed.
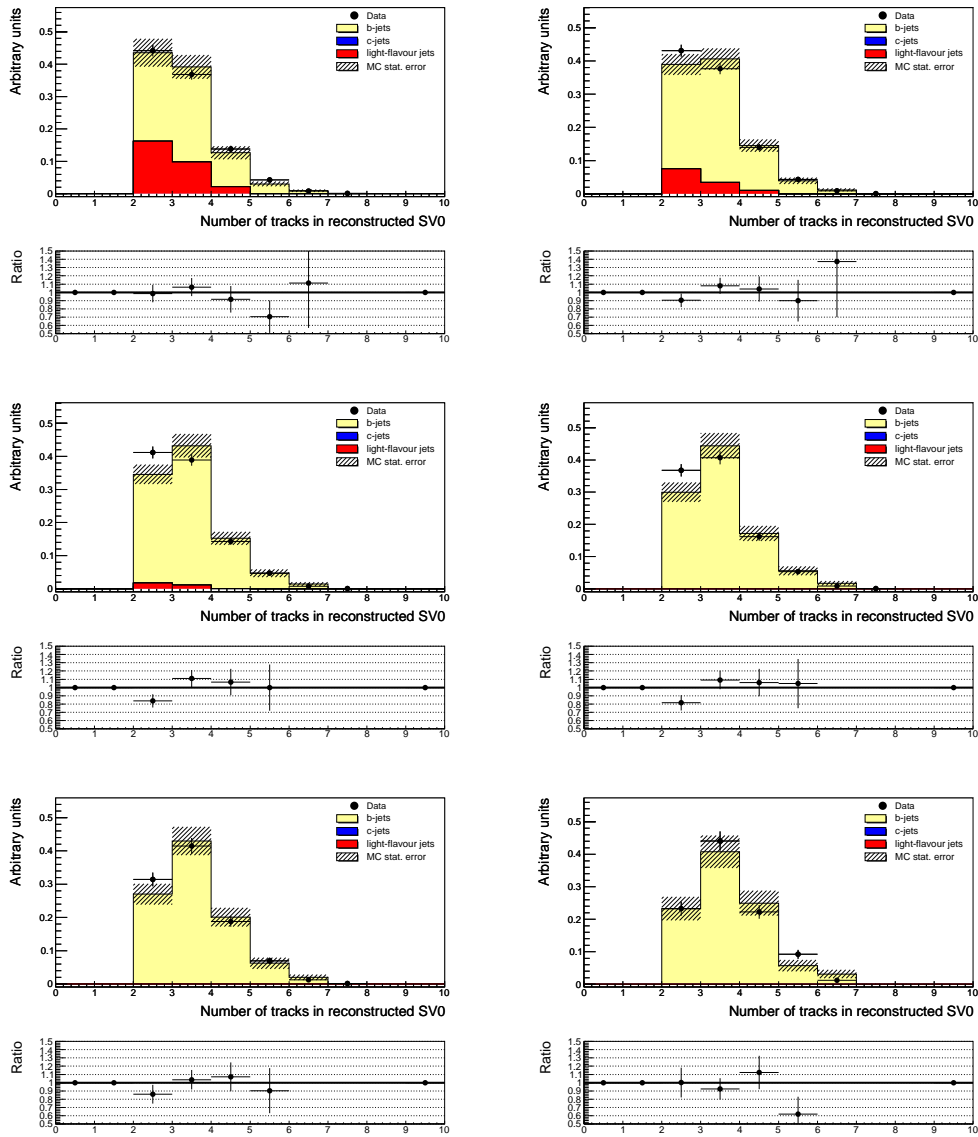
Figure B.13: Data to simulation comparison of the number of tracks used for the reconstructed SV0 secondary vertex on the tagged sample for the 60 GeV - 90 GeV bin. The templates are taken from the JXμ samples and the fractions are taken from the p$_T^{rel}$ fit. Shown are SV050 on the top left, SV045 on the top right and SV040 on the bottom. The c-jet template is used for the light jets since the fit cannot distinguish c-jets from light jets but a c-jet is more likely to be tagged. Therefore perfect agreement cannot be expected.
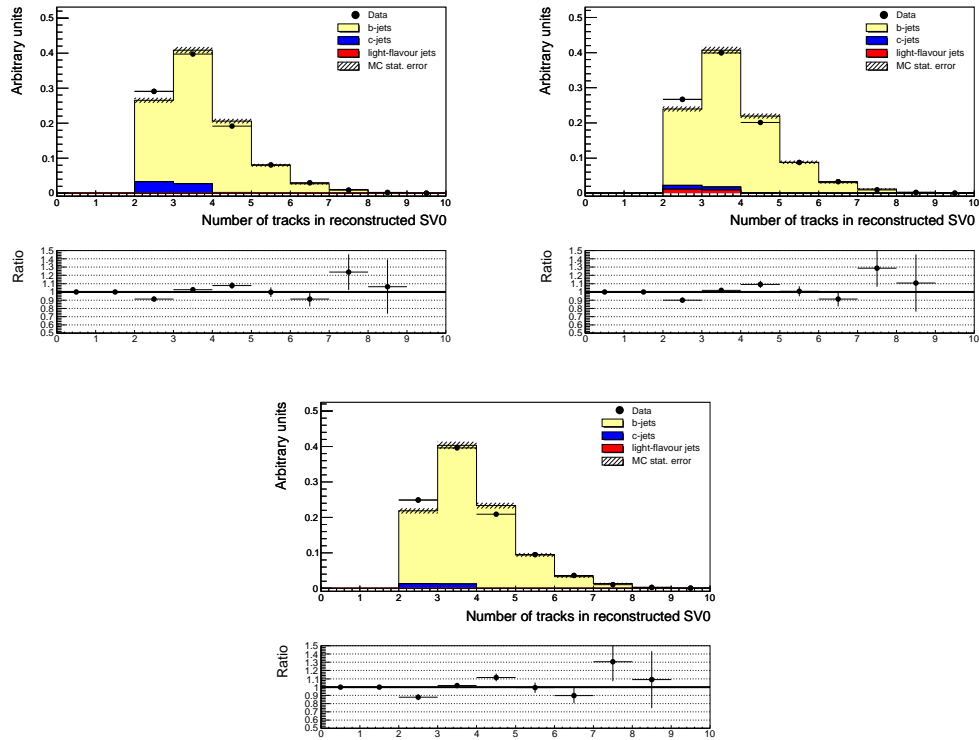
Figure B.14: Data to simulation comparison of the number of tracks used for the reconstructed SV0 secondary vertex on the tagged sample for the 60 GeV - 90 GeV bin. The templates are taken from the $JX\mu$ samples and the fractions are taken from the p_T^{rel} fit. From top left to bottom right the operating points shown are JetProb90, JetProb80, JetProb70, JetProb60, JetProb50 and JetProb40. The c-jet template is used for the light jets since the fit cannot distinguish c-jets from light jets but a c-jet is more likely to be tagged. Therefore perfect agreement cannot be expected. The 0 bin is suppressed.
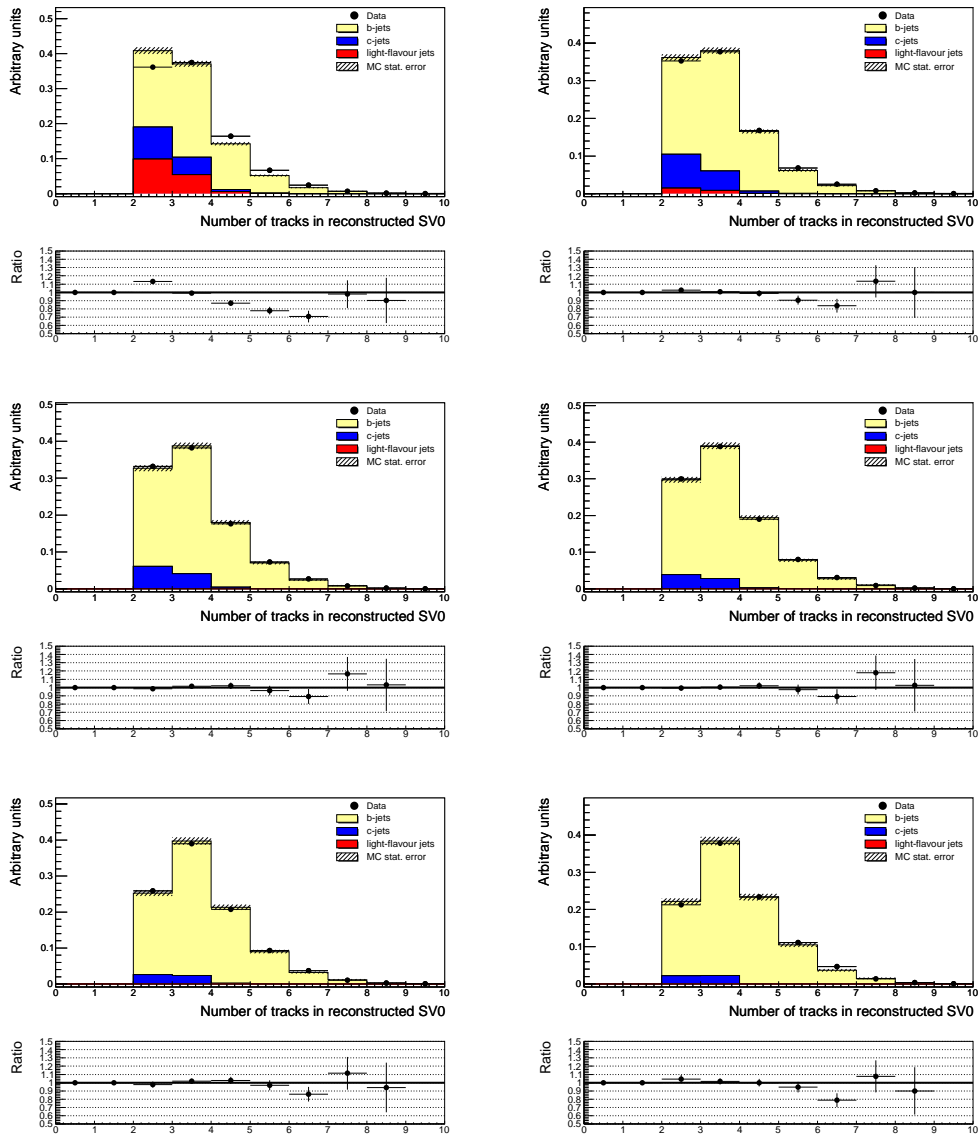
Figure B.15: Data to simulation comparison of the number of tracks used for the reconstructed SV0 secondary vertex on the tagged sample for the 90 GeV - 140 GeV bin. The templates are taken from the JXμ samples and the fractions are taken from the p_T^{rel} fit. Shown are SV050 on the top left, SV045 on the top right and SV040 on the bottom. The c-jet template is used for the light jets since the fit cannot distinguish c-jets from light jets but a c-jet is more likely to be tagged. Therefore perfect agreement cannot be expected.
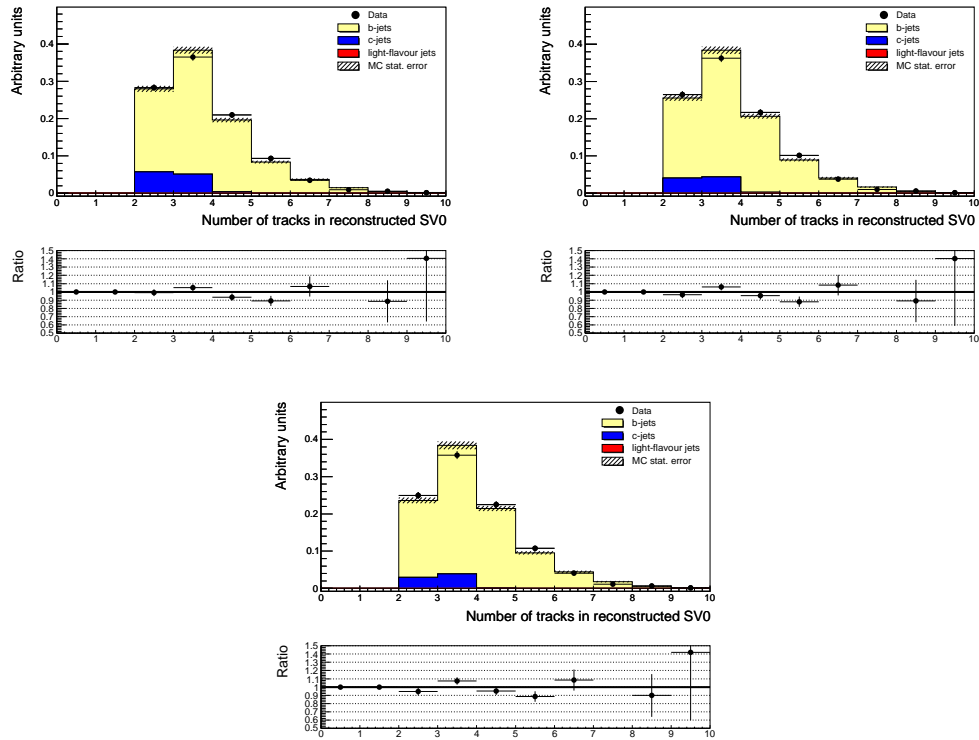
Figure B.16: Data to simulation comparison of the number of tracks used for the reconstructed SV0 secondary vertex on the tagged sample for the 90 GeV - 140 GeV bin. The templates are taken from the JXμ samples and the fractions are taken from the p$_T^{rel}$ fit. From top left to bottom right the operating points shown are JetProb90, JetProb80, JetProb70, JetProb60, JetProb50 and JetProb40. The c-jet template is used for the light jets since the fit cannot distinguish c-jets from light jets but a c-jet is more likely to be tagged. Therefore perfect agreement cannot be expected. The 0 bin is suppressed.
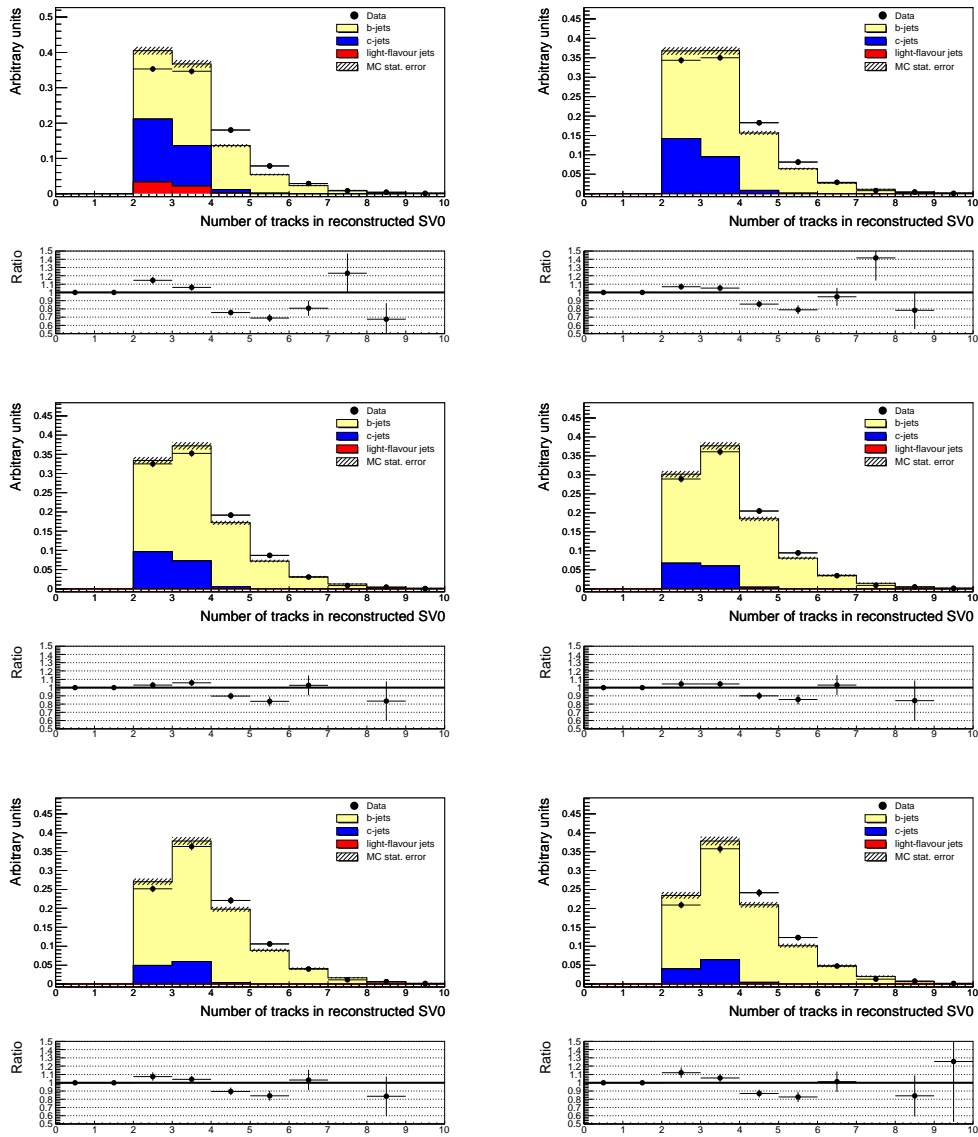
Figure B.17: Data to simulation comparison of the mass of the reconstructed SV0 secondary vertex before tagging. The fractions are the taken from JX simulation. The light template is also taken from JX simulation. From top left to bottom right the 20 GeV - 30 GeV, the 30 GeV - 60 GeV the 60 GeV - 90 GeV and the 90 GeV - 140 GeV bins are shown.

Figure B.18: Data to simulation comparison of the number of tracks used for the reconstructed SV0 secondary vertex before tagging. The fractions are the taken from JX simulation. The light template is also taken from JX simulation. From top left to bottom right the 20 GeV - 30 GeV, the 30 GeV - 60 GeV the 60 GeV - 90 GeV and the 90 GeV - 140 GeV bins are shown.

Figure B.19: Data to simulation comparison of the mass of the reconstructed SV0 secondary vertex before tagging. The fractions are the results from the p_T^{rel} method. The light template is taken from JX simulation. From top left to bottom right the 20 GeV - 30 GeV, the 30 GeV - 60 GeV the 60 GeV - 90 GeV and the 90 GeV - 140 GeV bins are shown.
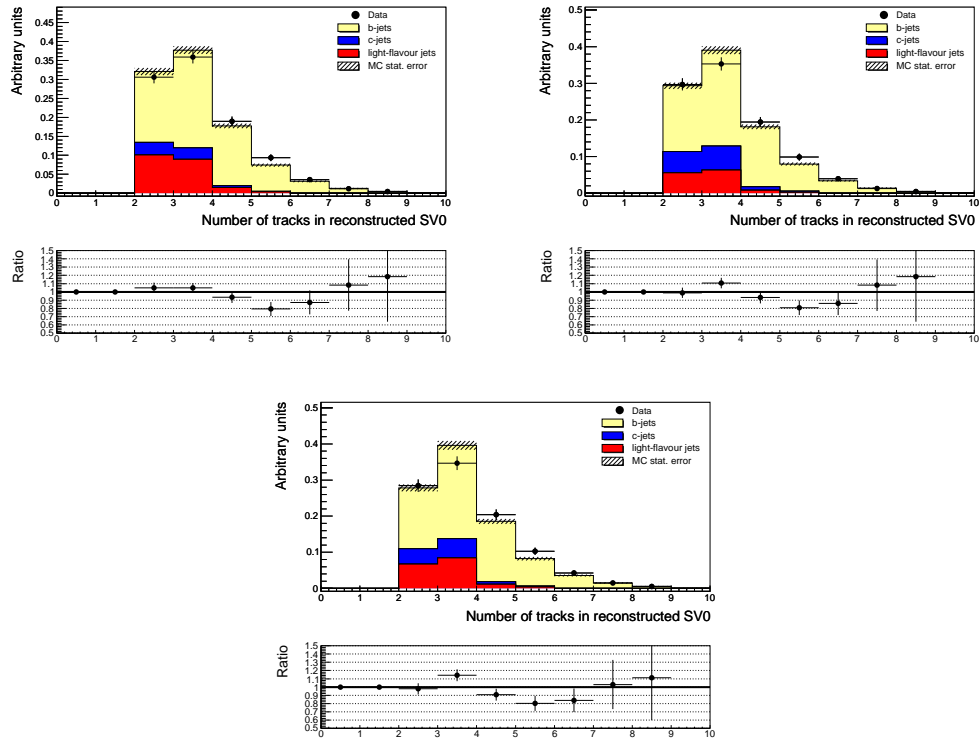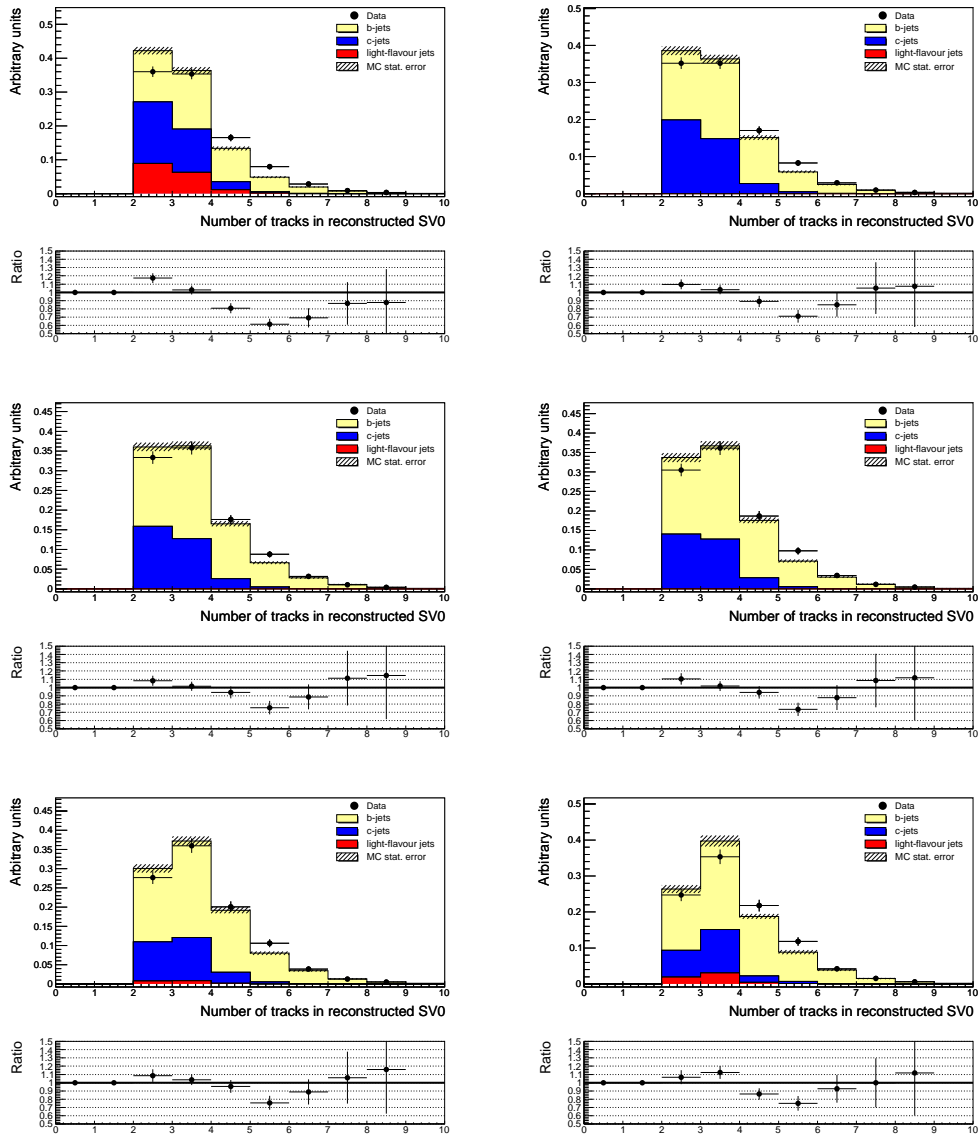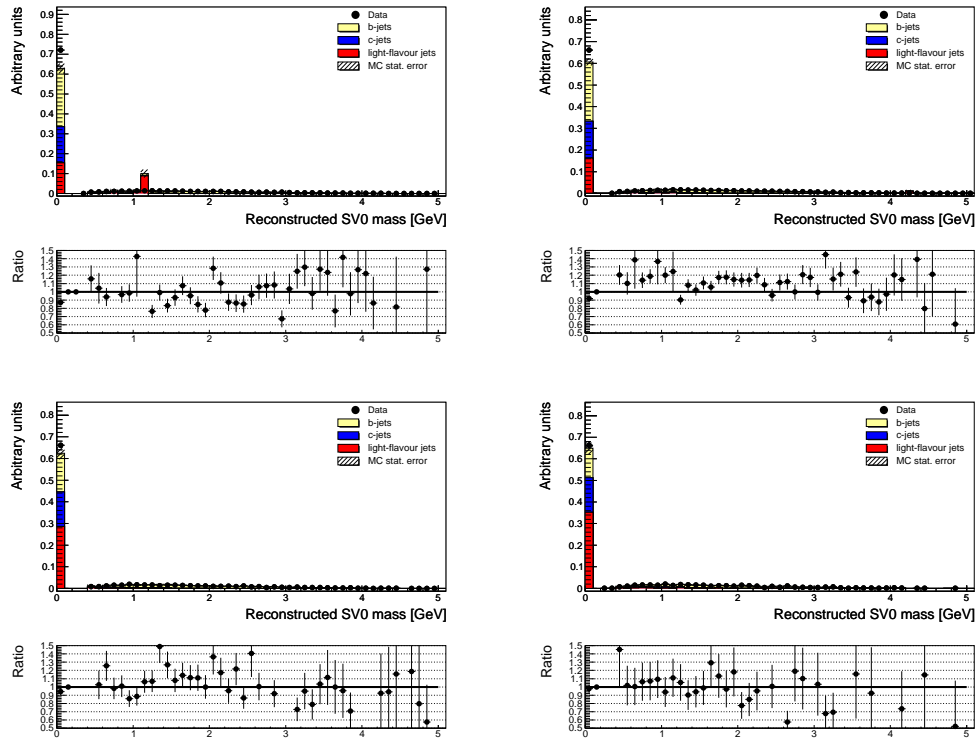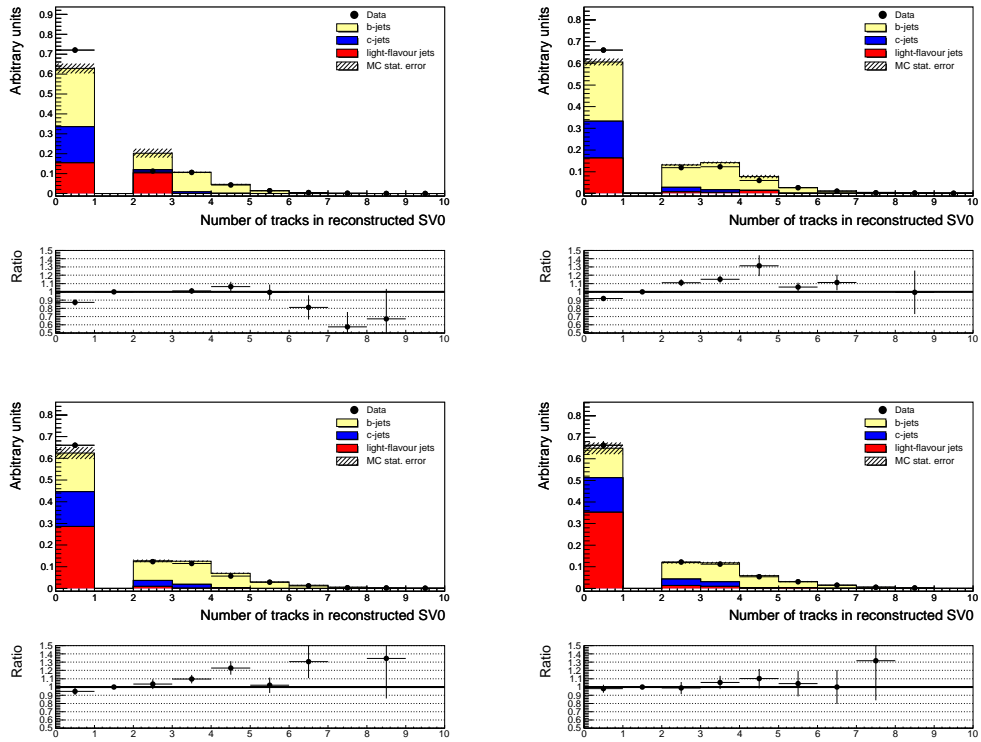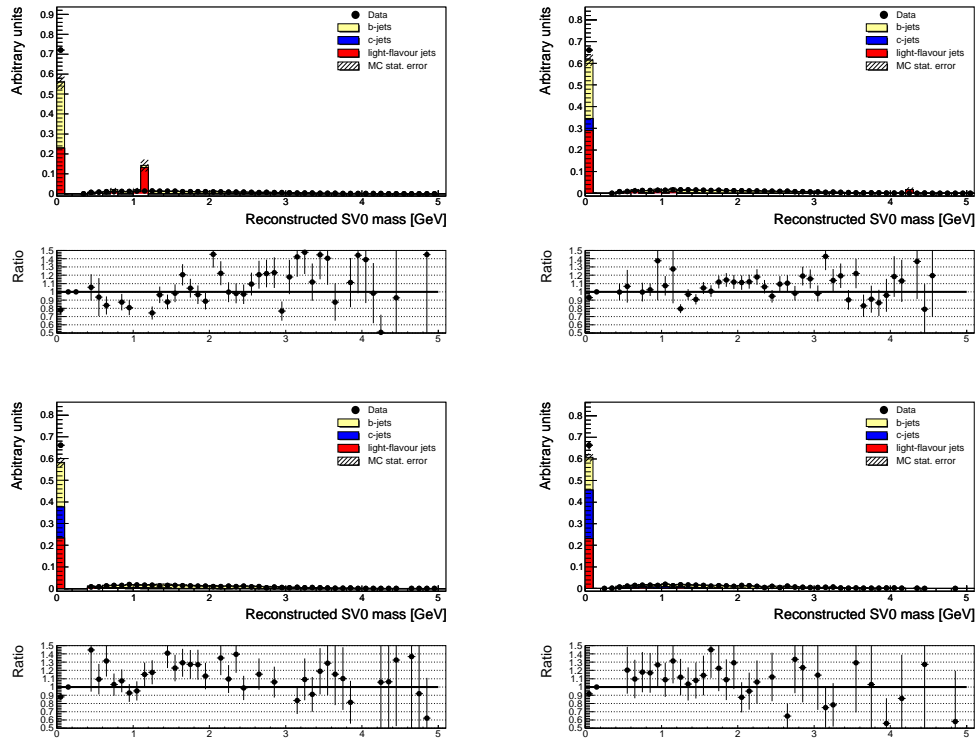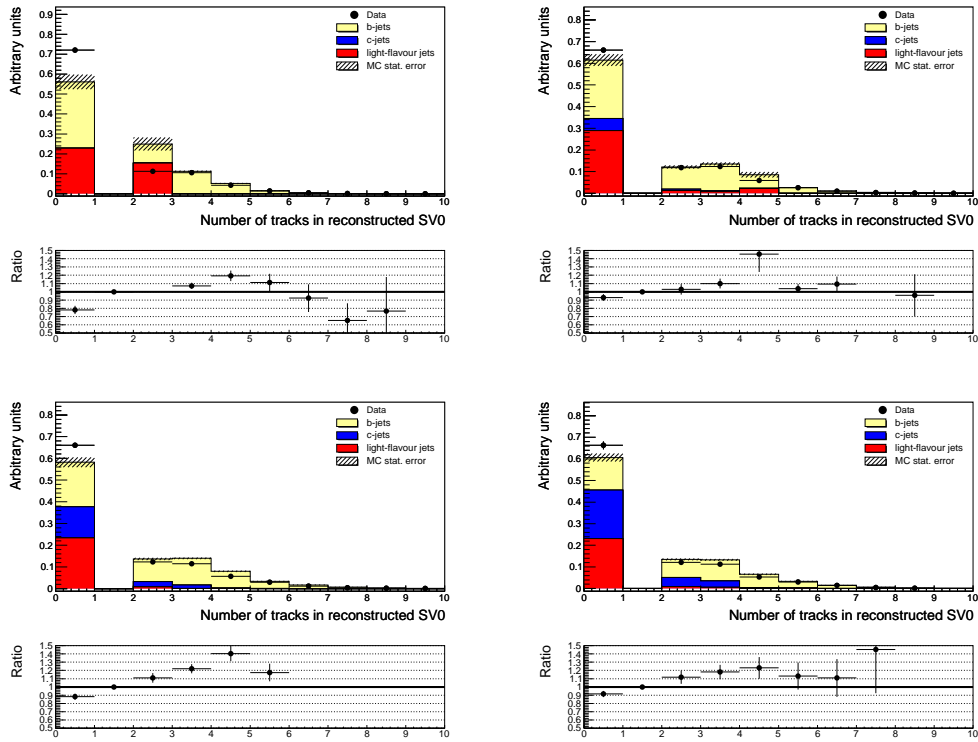
Figure B.20: Data to simulation comparison of the number of tracks used for the reconstructed SV0 secondary vertex before tagging. The fractions are the results from the p$_T^{rel}$ method. The light template is taken from JX simulation. From top left to bottom right the 20 GeV - 30 GeV, the 30 GeV - 60 GeV the 60 GeV - 90 GeV and the 90 GeV - 140 GeV bins are shown.

C Systematic uncertainties of the p_T^{rel} method

Systematic	No Cut	η		$p_\perp$ [GeV]			
		$0-1.2$	$1.2-2.5$	$20-30$	$30-60$	$60-90$	$90-140$
B-hadron direction	0.58	0.14	0.15	2.21	0.08	1.55	3.77
Light Template Modeling (b variation)	0.88	0.79	0.95	0.81	0.80	0.65	0.24
Jet Energy Scale	0.20	0.18	0.04	0.80	0.15	0.33	0.12
B Fragmentation	0.03	0.12	0.24	1.11	0.17	0.09	0.15
Fake Muons	0.20	0.18	0.04	0.80	0.15	0.33	0.12
B Decay	2.47	1.85	2.35	4.58	3.00	0.70	0.42
B Decay (up/down)	0.33	0.12	0.42	1.04	0.41	0.07	0.01
mc Stats	1.70	1.81	2.71	5.14	2.00	1.83	2.39
Gluon Splitting C	0.59	0.21	0.74	0.12	0.61	0.92	7.25
Gluon Splitting B	0.36	0.54	0.59	2.40	0.07	0.60	0.75
Muon Reweighting	3.34	0.71	2.11	4.13	3.62	1.87	3.37
SF to inclusive jets	1.40	2.19	0.79	1.59	2.91	1.08	4.16
Total	4.89	3.61	4.47	9.05	5.98	3.57	10.10

Table C.1: Systematic uncertainties in percent for the SV050 working point.

Systematic	No Cut	η		$p_\perp$ [GeV]			
		$0-1.2$	$1.2-2.5$	$20-30$	$30-60$	$60-90$	$90-140$
B-hadron direction	0.50	0.08	0.05	1.72	0.32	1.93	3.23
Light Template Modeling (b variation)	0.88	0.83	0.95	0.81	0.76	0.65	0.35
Jet Energy Scale	0.19	0.19	0.05	0.80	0.35	0.33	0.05
B Fragmentation	0.03	0.11	0.23	1.10	0.08	0.09	0.15
Fake Muons	0.19	0.19	0.05	0.80	0.35	0.33	0.05
B Decay	3.05	1.92	2.39	4.58	3.02	0.63	0.30
B Decay (up/down)	0.33	0.13	0.42	1.04	0.23	0.07	0.02
mc Stats	1.73	1.85	2.80	5.46	2.01	1.93	2.60
Gluon Splitting C	0.17	0.23	0.72	0.17	0.14	0.73	6.44
Gluon Splitting B	0.16	0.54	0.59	2.92	0.48	0.60	0.68
Muon Reweighting	5.83	1.31	2.62	4.14	5.71	4.59	2.80
SF to inclusive jets	1.32	2.34	0.34	1.58	3.03	1.19	4.57
Total	7.02	3.92	4.75	9.28	7.50	5.64	9.39

Table C.2: Systematic uncertainties in percent for the SV045 working point.

Systematic	No Cut	η		$p_\perp$ [GeV]			
		$0-1.2$	$1.2-2.5$	$20-30$	$30-60$	$60-90$	$90-140$
B-hadron direction	0.41	0.12	0.10	1.71	0.18	2.13	5.07
Light Template Modeling (b variation)	0.88	0.85	0.95	0.81	0.80	0.65	0.30
Jet Energy Scale	0.19	0.18	0.05	0.80	0.14	0.32	0.11
B Fragmentation	0.03	0.10	0.23	1.10	0.18	0.08	0.22
Fake Muons	0.19	0.18	0.05	0.80	0.14	0.32	0.11
B Decay	4.33	1.93	2.50	4.59	4.52	0.62	0.35
B Decay (up/down)	0.34	0.12	0.43	1.04	0.40	0.08	0.01
mc Stats	1.75	1.93	2.85	6.59	2.11	2.09	2.99
Gluon Splitting C	0.47	0.22	0.66	0.09	0.27	0.63	6.77
Gluon Splitting B	0.38	0.54	0.61	2.93	0.20	0.62	0.78
Muon Reweighting	7.08	2.84	3.63	4.14	7.17	6.34	2.92
SF to inclusive jets	1.17	2.39	0.29	1.22	3.03	1.26	4.99
Total	8.65	4.73	5.44	9.94	9.30	7.25	10.72

Table C.3: Systematic uncertainties in percent for the SV040 working point.

Systematic	No Cut	η		$p_\perp$ [GeV]			
		$0-1.2$	$1.2-2.5$	$20-30$	$30-60$	$60-90$	$90-140$
B-hadron direction	0.59	0.42	0.76	0.56	0.69	1.21	0.33
Light Template Modeling (b variation)	0.45	0.37	0.43	0.30	0.46	0.51	0.20
Jet Energy Scale	0.11	0.33	0.02	0.06	0.15	0.13	0.04
B Fragmentation	0.00	0.00	0.05	0.02	0.02	0.01	0.00
Fake Muons	0.11	0.33	0.02	0.06	0.15	0.13	0.04
B Decay	0.41	0.31	0.32	0.21	0.50	0.08	0.09
B Decay (up/down)	0.04	0.04	0.04	0.00	0.05	0.00	0.00
mc Stats	0.69	0.71	0.89	1.77	1.28	0.69	0.69
Gluon Splitting C	0.16	0.21	0.04	0.11	0.10	1.22	0.12
Gluon Splitting B	0.22	0.06	0.08	0.07	0.21	0.19	0.01
Muon Reweighting	0.01	0.16	0.31	0.22	0.26	0.90	0.00
SF to inclusive jets	0.44	0.53	0.62	0.73	0.56	0.16	0.35
Total	1.22	1.22	1.47	2.04	1.74	2.15	0.88

Table C.4: Systematic uncertainties in percent for the JetProb90 working point.

Systematic	No Cut	η		$p_\perp$ [GeV]			
		$0-1.2$	$1.2-2.5$	$20-30$	$30-60$	$60-90$	$90-140$
B-hadron direction	0.89	0.12	0.80	1.83	0.24	0.27	2.17
Light Template Modeling (b variation)	0.79	0.61	0.75	0.63	0.75	0.65	0.51
Jet Energy Scale	0.12	0.24	0.01	0.13	0.17	0.41	0.21
B Fragmentation	0.02	0.03	0.04	0.05	0.05	0.11	0.32
Fake Muons	0.12	0.24	0.01	0.13	0.17	0.41	0.21
B Decay	1.38	0.70	0.76	1.21	2.22	0.91	0.31
B Decay (up/down)	0.10	0.07	0.08	0.03	0.14	0.05	0.06
mc Stats	1.30	1.23	1.75	3.28	1.52	1.49	1.65
Gluon Splitting C	0.20	0.15	0.08	0.06	0.13	2.22	0.04
Gluon Splitting B	0.30	0.01	0.28	0.12	0.33	0.51	0.21
Muon Reweighting	1.41	0.25	0.06	0.48	2.50	0.94	1.55
SF to inclusive jets	0.98	1.20	1.46	1.50	1.58	0.44	1.20
Total	2.85	2.01	2.66	4.31	4.10	3.19	3.44

Table C.5: Systematic uncertainties in percent for the JetProb80 working point.

Systematic	No Cut	η		$p_\perp$ [GeV]			
		$0-1.2$	$1.2-2.5$	$20-30$	$30-60$	$60-90$	$90-140$
B-hadron direction	0.86	0.01	1.08	2.62	0.05	0.77	2.54
Light Template Modeling (b variation)	0.88	0.70	0.95	0.77	0.80	0.65	0.51
Jet Energy Scale	0.21	0.16	0.01	0.08	0.18	0.39	0.25
B Fragmentation	0.04	0.12	0.23	0.01	0.16	0.10	0.34
Fake Muons	0.21	0.16	0.01	0.08	0.18	0.39	0.25
B Decay	2.30	1.38	2.06	2.00	2.84	0.76	0.46
B Decay (up/down)	0.32	0.08	0.37	0.07	0.39	0.06	0.08
mc Stats	1.51	1.45	2.08	3.89	1.74	1.33	1.83
Gluon Splitting C	0.70	0.18	0.71	0.12	0.62	1.43	1.75
Gluon Splitting B	0.33	0.46	0.46	0.20	0.09	0.58	0.54
Muon Reweighting	2.53	0.50	1.79	1.19	3.28	1.42	2.21
SF to inclusive jets	1.34	1.68	1.61	1.69	2.23	0.68	2.06
Total	4.25	2.81	4.16	5.56	5.30	2.92	4.79

Table C.6: Systematic uncertainties in percent for the JetProb70 working point.

Systematic	No Cut	η		$p_\perp$ [GeV]			
		$0-1.2$	$1.2-2.5$	$20-30$	$30-60$	$60-90$	$90-140$
B-hadron direction	0.61	0.06	0.42	1.62	0.26	1.52	3.05
Light Template Modeling (b variation)	0.88	0.75	0.95	0.81	0.80	0.65	0.51
Jet Energy Scale	0.20	0.15	0.02	0.80	0.16	0.35	0.20
B Fragmentation	0.04	0.13	0.24	1.10	0.16	0.09	0.24
Fake Muons	0.20	0.15	0.02	0.80	0.16	0.35	0.20
B Decay	2.41	1.43	2.18	4.59	2.92	0.62	0.39
B Decay (up/down)	0.33	0.09	0.39	1.04	0.40	0.07	0.03
mc Stats	1.66	1.66	2.35	4.69	2.32	1.45	2.05
Gluon Splitting C	0.82	0.05	0.68	0.15	0.80	1.04	2.97
Gluon Splitting B	0.35	0.40	0.49	2.92	0.09	0.58	0.35
Muon Reweighting	2.73	0.59	2.04	4.13	3.44	1.60	2.14
SF to inclusive jets	1.67	2.14	1.32	1.68	2.74	0.93	3.10
Total	4.58	3.24	4.27	8.85	5.91	3.21	6.10

Table C.7: Systematic uncertainties in percent for the JetProb60 working point.

Systematic	No Cut	η		$p_\perp$ [GeV]			
		$0-1.2$	$1.2-2.5$	$20-30$	$30-60$	$60-90$	$90-140$
B-hadron direction	0.52	0.09	0.33	1.48	0.34	1.52	4.07
Light Template Modelling (b variation)	0.88	0.78	0.95	0.81	0.80	0.65	0.48
Jet Energy Scale	0.20	0.17	0.02	0.80	0.16	0.37	0.14
B Fragmentation	0.04	0.13	0.25	1.10	0.17	0.09	0.23
Fake Muons	0.20	0.17	0.02	0.80	0.16	0.37	0.14
B Decay	2.45	1.67	2.10	4.59	2.96	0.68	0.42
B Decay (up/down)	0.33	0.10	0.38	1.04	0.40	0.07	0.01
mc Stats	1.70	1.75	2.65	5.49	1.95	1.65	2.54
Gluon Splitting C	0.71	0.19	0.50	0.19	0.73	0.99	4.28
Gluon Splitting B	0.36	0.51	0.46	2.92	0.09	0.61	0.48
Muon Reweighting	4.54	0.63	3.49	4.13	4.59	1.82	2.47
SF to inclusive jets	1.84	2.58	0.59	1.12	3.08	1.21	4.41
Total	5.90	3.73	5.07	9.19	6.68	3.51	8.22

Table C.8: Systematic uncertainties in percent for the JetProb50 working point.

Systematic	No Cut	η		$p_\perp$ [GeV]			
		$0-1.2$	$1.2-2.5$	$20-30$	$30-60$	$60-90$	$90-140$
B-hadron direction	0.50	0.31	0.62	1.31	0.32	1.22	4.99
Light Template Modeling (b variation)	0.88	0.80	0.95	0.81	0.80	0.65	0.44
Jet Energy Scale	0.20	0.18	0.02	0.80	0.15	0.37	0.17
B Fragmentation	0.03	0.12	0.25	1.10	0.17	0.08	0.21
Fake Muons	0.20	0.18	0.02	0.80	0.15	0.37	0.17
B Decay	2.47	1.54	2.05	4.58	2.98	0.76	0.43
B Decay (up/down)	0.33	0.11	0.38	1.04	0.41	0.06	0.01
mc Stats	1.76	2.12	2.93	6.78	2.17	2.03	3.27
Gluon Splitting C	0.71	0.05	0.73	0.15	0.73	0.93	4.64
Gluon Splitting B	0.36	0.33	0.48	2.92	0.07	0.63	0.62
Muon Reweighting	4.54	0.64	1.92	4.13	5.15	2.25	2.36
SF to inclusive jets	2.15	3.30	0.54	1.95	3.28	1.57	5.93
Total	6.02	4.37	4.37	10.12	7.24	3.96	9.93

Table C.9: Systematic uncertainties in percent for the JetProb40 working point.

Bibliography

[1] W. Cottingham and D. Greenwood, *An Introduction to the Standard Model of Particle Physics.* Cambridge University Press, 2007.

[2] K. Nakamura and others (PDG) J. Phys. G **37** (2010) 075021.

[3] J. M. Campbell, J. W. Huston, and W. J. Stirling, *Hard interactions of quarks and gluons: a primer for LHC physics*, Reports on Progress in Physics **70** (2007) no. 1, 89.

[4] L. Evans and P. Bryant, *LHC Machine*, JINST **3** (2008) S08001.

[5] The ATLAS Collaboration, *Luminosity Determination in pp Collisions at $\sqrt{s} = 7$ TeV Using the ATLAS Detector at the LHC*, Arxiv:1101.2185v1 [hep-ex], January, 2011.

[6] The ATLAS Collaboration, *Further investigations of ATLAS Sensitivity to Higgs Boson Production in different assumed LHC scenarios.*, ATLAS-CONF-2011-001, January, 2011.

[7] The LEP Collaborations ALEPH, DELPHI, L3 and OPAL, the LEP Electroweak Working Group, the Tevatron Electroweak Working Group, and the SLD electroweak and heavy flavour groups, *Precision Electroweak Measurements and Constraints on the Standard Model*, Arxiv:1012.2367v2 [hep-ex], January, 2011.

[8] M. Mühlleitner, *Higgs Particles in the Standard Model and Supersymmetric Theories.* PhD thesis, Universität Hamburg, 2000.

[9] G. P. Salam, *Towards jetography*, European Physical Journal C **67** (2010) 637–686.

[10] D. Asner et al., *Averages of b-hadron, c-hadron and τ-lepton Properties*, Arxiv:1010.1589v2 [hep-ex], January, 2011.

[11] R. Ellis, W. Stirling, and B. Webber, *QCD and Collider Physics.* Cambridge University Press, 1996.

[12] The DELPHI Collaboration, J. Abdallah et al., *Determination of heavy quark non-perturbative parameters from spectral moments in semileptonic B decays*, Eur. Phys. J. C 45 (2006) .

[13] *Measurement of $B\overline{B}$ angular correlations based on secondary vertex reconstruction at $\sqrt{s} = 7$ TeV*, Journal of High Energy Physics **2011** 1–35. 10.1007/JHEP03(2011)136.

[14] G. Aad et al., *The ATLAS Experiment at the CERN Large Hadron Collider*, JINST **3** (2008) S08003.

[15] CERN Photolab, *Computer generated image of the whole ATLAS detector*, http://cdsweb.cern.ch/record/1095924.

[16] The ATLAS Collaboration, *The Expected Performance of the Inner Detector.*, ATL-PHYS-PUB-2009-002, April, 2009.

[17] CERN Photolab, *Computer generated image of the ATLAS inner detector*, http://cdsweb.cern.ch/record/1095926.

[18] P. Behara et al., *Threshold Tuning of the ATLAS Pixel Detector*, ATL-INDET-PUB-2010-001, August, 2010.

[19] G. Aad et al., *Cosmic Ray Detection Efficiency for the ATLAS Pixel Detector*, ATL-COM-INDET-2010-051, 2010.

[20] D. Dobos, *Commissioning Perspectives for the ATLAS Pixel Detector.* PhD thesis, Universität Dortmund, 2007.

[21] G. Aad et al., *ATLAS Pixel Detector Electronics and Sensors*, Journal of Instrumentation **P07007** (2008) no. 3, .

[22] T. Fritzsch et al., *Experience in fabrication of multichip-modules for the ATLAS pixel detector*, Nuclear Instruments and Methods in Physics Research Section A **565** (2006) 309 – 313.

[23] G. Alimonti et al., *Analysis of the production of ATLAS indium bonded pixel modules*, Nuclear Instruments and Methods in Physics Research Section A **565** (2006) 296–302.

[24] A. Abdesselam et al., *The barrel modules of the ATLAS semiconductor tracker*, Nuclear Instruments and Methods in Physics Research Section A: Accelerators, Spectrometers, Detectors and Associated Equipment **568** (2006) no. 2, 642 – 671.

[25] CERN Photolab, *Computer Generated image of the ATLAS calorimeter*, http://cdsweb.cern.ch/record/1095927.

[26] CERN Photolab, *Computer generated image of the ATLAS Muons subsystem*, http://cdsweb.cern.ch/record/1095929.

[27] F. Hirsch et al., *Sensor and Bump Studies for the ATLAS Pixel Detector*, ATL-INDET-INT-2011-005, June, 2011.

[28] N. Garelli et al., *The Tuning and Calibration of the Charge Measurement of the Pixel Detector*, ATL-COM-INDET-2010-017, November, 2009.

[29] J. Biesiada et al., *The Implementation and Performance of ROD DSP Software in the ATLAS Pixel Detector*, ATL-INDET-INT-2010-006, February, 2010.

[30] L. Rossi, *Pixel Detectors: From Fundamentals to Applications.* Springer, 2006.

[31] F. Hügging, *Der state-of-the-art Pixelsensor für teilchenphysikalische Anwendungen mit extrem hohen Strahlungsfeldern.* PhD thesis, Universität Dortmund, 2001.

[32] M. S. Sze, *Physics of Semiconductor Devices.* John Wiley and Sons, 1981.

[33] A. Quadt, *Top quark physics at hadron colliders.* Springer, 2007.

[34] The ATLAS Collaboration, *Expected Performance of the ATLAS Experiment: Detector, Trigger and Physics.* CERN, Geneva, 2009.

[35] The ATLAS Collaboration, *Impact parameter-based b-tagging algorithms in the 7 TeV collision data with the ATLAS detector: the TrackCounting and JetProb algorithms*, ATLAS-CONF-2010-041, June, 2010.

[36] The ATLAS Collaboration, *Performance of the ATLAS Secondary Vertex b-tagging Algorithm in 7 TeV Collision Data*, ATLAS-CONF-2010-042, June, 2010.

[37] The ATLAS Collaboration, *Tracking Studies for b-tagging with 7 TeV Collision Data with the ATLAS Detector*, ATLAS-CONF-2010-070, July, 2010.

[38] The ATLAS Collaboration, *Calibrating the b-Tag and mistag Efficiencies of the SV0 b-tagging Algorithm in 3 pb^{-1} of Data with the ATLAS Detector*, ATLAS-CONF-2010-099, December, 2010.

[39] J. Boudreau et al., *b-Jet Tagging Efficiency Calibration using the System8 Method*, ATL-COM-PHYS-2011-033, January, 2011.

[40] The ATLAS Collaboration, *Calibrating the b-Tag Efficiency and Mistag Rate in 35 pb^{-1} of Data with the ATLAS Detector*, ATLAS-CONF-2011-089, June, 2011.

[41] F. Parodi et al., *b-tagging calibration with $D^*\mu$ reconstructed in 7 TeV collisions with ATLAS*, ATL-COM-PHYS-2011-051, January, 2011.

[42] T. Golling et al., *b-tagging calibration in ttbar final states and ttbar cross-section measurements with ATLAS data at $\sqrt{s}$=7 TeV*, ATL-COM-PHYS-2011-048, January, 2011.

[43] F. Garberson and T. Golling, *Measurement of the mistag efficiency in early Atlas data from fits to the SV0-mass of the tagged jets*, ATL-COM-PHYS-2011-029, February, 2011.

[44] M. Saleem et al., *Measurement of the Mistag Rate in ATLAS Data*, ATL-COM-PHYS-2011-046, February, 2011.

[45] The ATLAS Collaboration, *Performance of the ATLAS Silicon Pattern Recognition Algorithm in Data and Simulation at $\sqrt{s} = 7$ TeV*, ATLAS-CONF-2010-072, July, 2010.

[46] S. Hassani et al., *A muon identification and combined reconstruction procedure for the ATLAS detector at the LHC using the (MUONBOY, STACO, MuTag) reconstruction packages*, NIM A **572** (2007) no. 1, 77 – 79.

[47] L. Asquith et al., *Performance of Jet Algorithms in the ATLAS Detector*, ATL-PHYS-INT-2010-129, December, 2010.

[48] The ATLAS Collaboration, *Jet energy scale and its systematic uncertainty in proton-proton collisions at sqrts = 7TeV with ATLAS 2010 data*, ATLAS-CONF-2011-032, March, 2011.

[49] S. Aoun et al., *A Measurement of the b-jet production cross section with 2010 ATLAS data using muons in jets*, ATL-COM-PHYS-2011-221, March, 2011.

[50] The ATLAS Collaboration, *Performance of primary vertex reconstruction in proton-proton collisions at $\sqrt{s} = 7$ TeV in the ATLAS experiment*, ATLAS-CONF-2010-069, July, 2010.

[51] A. Coccaro, *Tracking and b-tagging for the ATLAS trigger system.* PhD thesis, Universita degli studi di Genova, 2010.

[52] T. Sjostrand, S. Mrenna, and P. Z. Skands, *PYTHIA 6.4 Physics and Manual*, JHEP **05** (2006) 026.

[53] A. Sherstnev and R. S. Thorne, *Parton Distributions for LO Generators*, Eur. Phys. J. **C55** (2008) 553–575.

[54] GEANT4 Collaboration, S. Agostinelli et al., *GEANT4: A simulation toolkit*, Nucl. Instrum. Meth. **A506** (2003) 250–303.

[55] Barlow, R. and Beeston, C., *Fitting using finite Monte Carlo samples*, Computer Physics Communications **77** (1993) 219–228.

[56] The ATLAS Collaboration, *First observation of the $J/\Psi \to \mu^+\mu^-$ resonance in ATLAS pp collisions at $\sqrt{s}=7$ TeV*, ATLAS-CONF-2010-045, June, 2010.

[57] A. Schwartzman, *Identification of b-jets from gluon splitting*, ATL-PHYS-INT-2008-042, December, 2008.

[58] The ATLAS Collaboration, *Measurement of the top quark pair cross-section with ATLAS in pp collisions at $\sqrt{s} = 7$ TeV in the single-lepton channel using b-tagging*, ATLAS-CONF-2011-035, March, 2011.

[59] The ATLAS Collaboration, *Top Quark Pair Production Cross-section Measurement in ATLAS in the Single Lepton+Jets Channel Without b-tagging*, ATLAS-CONF-2011-023, March, 2011.

[60] B. Acharya et al., *Cut-and-count measurement of the top quark pair production in the semileptonic decay channel at $\sqrt{s} = 7$ TeV with the ATLAS detector*, ATL-PHYS-INT-2011-048, May, 2011.

[61] B. Abi et al., *Measurements of the top pair production cross-section in 7 TeV proton-proton collisions using kinematic fits without b-tagging*, ATL-COM-PHYS-2011-104, February, 2011.

Nomenclature

ADC   Analog-to-Digital Converter

AMS   Alenia Marconi Systems, now Selex Sistemi Integrati

ATLAS   A Toroidal LHC Apparatus

CERN   Organisation Européenne pour la Recherche Nucléaire

CMS   Compact Muon Solenoid

CSC   Cathode Strip Chamber

DAC   Digital to Analog Converter

EM   Electromagnetic

IZM   Fraunhofer Institute for Reliability and Microintegration

LHC   Large Hadron Collider

MDT   Monitored Drift Tube

RPC   Resistive Plate Chamber

SCT   Semiconductor Tracker

TGC   Thin Gas Chamber

TRT   Transition Radiation Tracker

Acknowledgments

Creating this thesis was only possible due to the continuous support of many people. Some of them I want to list here and to all of them I want to say Thank You!

First of all I want to thank Prof. Dr. Claus Gößling for being my supervisor in the years I spent working with him and his working group. He kindled my interest in particle physics during my time as an undergraduate student and allowed me to spend most of my time as a graduate student at the heart of the experiment at CERN which was an invaluable experience.
Along the same lines I want to thank Prof. Dr. Dr. Wolfgang Rhode for being influential on my way as a physicist, all the way from teaching the basics of particle physics to me up to evaluating this thesis.

I want to thank my colleagues from E4 for all the fruitful discussions we had. Especially I want to thank Priv.-Doz. Dr. Reiner Klingenberg for leading the analysis group in Dortmund. I also want to thank Moritz Bunse, Dr. Daniel Dobos, Christian Jung, Dr. Jens Weingarten and all the other members of E4 that accompanied me at different steps of my time with the ATLAS experiment.
And thank you Monika Schoknecht and Andrea Teichmann for helping me navigate the intricacies of Reisekosten.

Many people I met at CERN deserve my gratitude for making my stay at CERN a useful, productive and also fun time. Especially I want to thank Beniamino Di Girolamo, Beate Heinemann, Tobias Golling, Sara Strandberg and Christian Weiser for being mentors and friends.
Special thanks to my good friends and roommates in Geneva, Ted Kolberg and Rachel Yohay. Thank you for making life in Switzerland so much fun.

Most importantly, I am grateful for all the support and love of my family and of my friends. Thank you for being there not only during the time I spent working on this thesis, but always.
And thank you Joana for being with me even though we could not see each other nearly enough during my stay at CERN. I am glad you are there.